Untangling Jellyfish Galaxies: Exploring the Kinematic and Physical Properties of Galaxies Undergoing Hydrodynamical Interactions Using the New Generation of Integral Field Units

Callum Bellhouse

A thesis submitted to the University of Birmingham
for the degree of Doctor of Philosophy

School of Physics and Astronomy
College of Engineering and Physical Sciences
University of Birmingham
September 2019

Abstract

Understanding the role and importance of different mechanisms which act to transform and evolve galaxies in the universe is vital in order to build a picture of the lifecycle of galaxies. Many observations over the years have shed light on such processes, both internal to galaxies and resulting from the influence of their environments. In this thesis, the current picture of galaxy evolution will be presented through a review of the literature, narrowing the focus down to a particular process which becomes important within dense environments such as groups and clusters: Ram-pressure stripping. Three studies are subsequently presented which investigate the effect of ram-pressure stripping on a galaxy, uncovering how and from where gas is stripped, the effect of stripping on a galaxy's star formation and the fate of the gas that is removed from the galaxy. By studying the scope and effectiveness of ram-pressure stripping in great detail on an archetypal jellyfish galaxy, steps are taken towards understanding the importance of the process and its role in transforming galaxies in the universe.

qué placer es hallar por fin,
subiendo
un planeta vacío,
grandes estrellas claras como el vodka
— Pablo Neruda

Acknowledgements

I'd like to thank a lot of people for helping me along the journey of writing this thesis, and through the work that has gone into it.

In particular, with me at every step of the way, I'd like to thank Claire, who supported me moving to a new, personally uncharted part of the world in Chile and turned it into a real adventure through deserts, mountains and glaciers, in all kinds of unsuitable camping conditions.

I'd like to thank my supervisors, to whom I have a great deal of respect for their advice and perpective along the way. Sean, whose advice and guidance has been invaluable, who from the beginning has taught me the importance of seeing the big picture and seeking the important questions to ask, as well as testing my spanish skills to their limit in markets. George, who not only taught me a wealth of analysis skills and techniques, but also helped me a huge amount moving to Chile; settling in, moving house and even finding the best vinyards to explore. I'm very grateful to Yara for being a fantastic mentor, for giving great guidance on scientific writing and passing on research skills which have been invaluable.

Finally, I'd like to thank my family for all their support along the way, my colleagues at ESO and at the University of Birmingham, as well as Bianca and everyone in the GASP team, for making this an exciting, compelling and intellectually demanding undertaking which I have thoroughly enjoyed.

Contents

1 Introduction **1**
- 1.1 Structure Formation . . . 3
- 1.2 Galaxy Evolution and Interactions in Clusters . . . 6
  - 1.2.1 Tidal Interactions Between Galaxies . . . 7
  - 1.2.2 Tidal Interactions Between Galaxies and the cluster potential . . . 8
  - 1.2.3 Mergers . . . 8
  - 1.2.4 Harassment . . . 9
  - 1.2.5 Viscous Stripping . . . 9
  - 1.2.6 Thermal Evaporation . . . 9
  - 1.2.7 Strangulation . . . 10
  - 1.2.8 Ram Pressure Stripping . . . 10
  - 1.2.9 Interplay Between Transformational Processes . . . 13
- 1.3 Probes of Gas Stripping . . . 14
- 1.4 Previous Studies of Ram-Pressure Stripping . . . 16
  - 1.4.1 Observations . . . 16
  - 1.4.2 Simulations . . . 18
- 1.5 GASP . . . 19
  - 1.5.1 Outline of the GASP survey . . . 19
  - 1.5.2 Observations . . . 20
  - 1.5.3 GASP results and Notable Galaxies . . . 21
- 1.6 JO201 . . . 24
- 1.7 Thesis Plan . . . 25

2 Kinematic Properties of a Galaxy Undergoing Ram-Pressure Stripping **27**
- 2.1 Introduction . . . 27
- 2.2 JO201 and Its Environment . . . 28
- 2.3 Data . . . 34
  - 2.3.1 MUSE Observations . . . 34
  - 2.3.2 Data Reduction . . . 34
  - 2.3.3 Galactic Extinction Correction . . . 37
- 2.4 Emission-Line Fitting . . . 37
  - 2.4.1 Single-Component Fits . . . 38
  - 2.4.2 Double-Component Fits . . . 39
  - 2.4.3 Final Fits . . . 42
  - 2.4.4 Hα Distribution . . . 42

2.4.5 3D Rendering of Hα Emission . . . 46
2.5 Kinematics . . . 46
2.5.1 Absorption-Line Kinematics . . . 46
2.5.2 Emission-Line Kinematics . . . 50
2.5.3 Rotation Curves . . . 56
2.6 Summary and Conclusions . . . 59

3 Physical Properties of a Galaxy Undergoing Ram-Pressure Stripping 63
3.1 Introduction . . . 63
3.2 Data . . . 65
3.2.1 The jellyfish galaxy JO201 . . . 65
3.2.2 MUSE datacube . . . 67
3.2.3 Dust extinction . . . 67
3.2.4 Emission-Only Datacube . . . 69
3.3 Emission-Line Fits . . . 69
3.4 Emission-Line Diagnostics . . . 72
3.4.1 Gas Ionisation Mechanism . . . 72
3.4.2 Metallicity and Ionisation Parameter . . . 75
3.5 Star Forming Knots . . . 78
3.6 Star Formation . . . 81
3.7 Stellar Populations . . . 85
3.8 Stripping Timescale and Length of the Stripped Tails . . . 86
3.8.1 Stripping Timescale from an Orbital Analysis . . . 86
3.8.2 Timescale of Star-Formation in the Stripped Tails . . . 89
3.8.3 Physical Length of the Stripped Tails . . . 90
3.9 Conclusions . . . 93

4 The Morphological effects of Ram-Pressure Stripping on the Arms of Spiral Galaxies 97
4.1 Introduction . . . 97
4.2 The Sample . . . 98
4.2.1 Morphologies . . . 101
4.2.2 Kinematics . . . 101
4.3 Galaxy orbits . . . 104
4.4 Spiral Arms . . . 105
4.4.1 Identifying spiral structure . . . 105
4.4.2 Gradients in stellar ages . . . 107
4.5 Simulations . . . 109
4.5.1 Comparing Observations with Simulations . . . 115
4.5.2 Tracing Unwinding Throughout Infall . . . 116
4.6 Discussion . . . 117

5 Conclusions 123
5.1 Summary . . . 123
5.2 Discussion . . . 126

List of Figures

1.1 NASA/ESA Hubble space telescope and Chandra X-ray observatory image of the jellyfish galaxy ESO 137-001, ESO VLT and ALMA molecular gas map of ESO 137-001 11

2.1 WINGS V-band image of the central part of Abell 85 showing the BCG, jellyfish galaxy JO201 and its possible kinematically selected group companions 29

2.2 *Left:* Projected phase-space diagram showing the location of JO201 and its group companions along with galaxies in Abell 85, against all OmegaWINGS cluster galaxies for comparison. RPS models of the extent of stripping on JO201 by Abell 85 are shown. *Right:* Dressler-Shectman "bubble" plot, showing the spatial distribution of galaxies in Abell 85, colour-coded by their velocity deviations 30

2.3 Chandra X-ray map of Abell 85 30

2.4 RGB image from JO201 GASP observation produced by combining slices integrated from the MUSE datacube. 35

2.5 Hα signal-noise-ratio map calculated from the line fits to the MUSE data. 36

2.6 Observed Hα, NII emission line group in 3 different spaxels within JO201 compared with a 2 component fit. *Top panel:* The central region of the galaxy, broadened by the AGN. *Middle panel:* A region within the north-eastern star-forming blob. *Bottom panel:* A region in the outer part of the disk displaying obvious tails redward of the emission. 39

2.7 Profiles of double-component fits made to Hα emission lines in JO201, separated into the combined flags described in Section 2.4.2. 41

2.8 Map of fitted spaxels in JO201, separated into regions where double-component fits were used (coloured) or where single-component fits were sufficient to fit the Hα emission (grey). 43

2.9 Contours of Hα (λ6562.82Å) overlaid on continuum fit around Hα line. Steeper contours on the western edge of the disk suggest increased star formation activity resulting from the interaction with the ICM. 45

2.10 3D visualisation of Hα gas extracted from KUBEVIZ fit. X and Y axes show projected distance, with the Z axis representing the wavelength/velocity and linewidth/sigma. An interactive version of this figure is accessible online at `web.oapd.inaf.it/gasp/publications.html`. . . 47

2.11 Stellar kinematics (*left:* line-of-sight velocity, *right:* velocity dispersion) derived from ppxf fits binned using a Voronoi Tessellation. 48

2.12 *Left:* Velocity map produced of Hα (λ6562.82Å) emission relative to the galaxy systemic velocity comprised of a combination of single component and two-component fits as described in section 2.4.2. *Right:* Velocity map as on left, cropped to show the disk region with a rescaled colour map to better exhibit the Hα kinematics of the disk region. 49

2.13 Velocity offset between broad and narrow components of Hα (λ6562.82Å) line where double component fit is available. 51

2.14 Velocity dispersion map produced using Hα (λ6562.82Å) emission from combined single component and two-component fits. 52

2.15 2D histogram of distribution of spaxels arranged by velocity on x axis and sigma on y axis. . 53

2.16 Rotation curve along the kinematic major axis r_{maj} for the stellar and gaseous components of JO201, showing the line-of-sight gas stripping ongoing in the galaxy. 55

2.17 Rotation curves of JO201, measured within a $\sim$10 arcsecond-wide strip along the kinematic major axis r_{maj} of the stellar disk. 58

3.1 Composite image of JO201 in Hα, stellar continuum and [OIII]. 66

3.2 V-band attenuation (A_V, in magnitudes) derived from the Balmer decrement and used to calculate the corrections required for internal dust extinction. 68

3.3 *Top:* Emission-line maps of Hα, [SII], [OIII], [NII] and Hβ from the dust-corrected emission-only cube. *Bottom:* Examples of spectra, with stellar component subtracted, corresponding to 3 regions of interest. 70

3.4 [OIII], [NII] BPT line-ratio diagnostics for all spaxels using the primary and secondary components of the two-component fits, alongside their spatial distribution mapped on top of the galaxy. 73

3.5 [OIII], [NII] BPT line ratio diagnostics for the primary and secondary components for all spaxels, coloured by Hα velocity dispersion. 74

3.6 Example pyqz grid for a sample spectrum in the galaxy disk 76

3.7 Metallicity of stripped gas in HII regions of JO201 calculated using pyqz. 77

3.8 *Left:* Metallicity calculated using pyqz direct estimate for integrated spectra of SF knots shown over Hα linemap. *Right:* Metallicity of knots from left panel against their projected distance r_{proj} from centre of disk. 78

3.9 *Left:* Distribution of SFR for star-forming (red, solid) and composite (green, dashed) knots. The central knot, dominated by AGN emission, has been excluded. *Middle:* Gas density distribution of individual knots *Right:* Distribution of ionised gas masses within knots. 80

3.10 Star-formation rate surface density within JO201 calculated for each spaxel ($M_{\odot}yr^{-1}kpc^{-2}$). 81

3.11 Luminosity weighted stellar age (colourbar) shown along with of stellar continuum isophotes (white contours). 82

3.12 Star-formation rate surface density grouped into several stellar age ranges, indicating the average SFR per kpc^2 83

3.13 Projected position-velocity phase-space diagram of all the galaxies in A85, including JO201. Blue curves correspond to different levels of gas stripping via ram-pressure. Orbits of simulated JO201-like haloes in a massive cluster are indicated. 88

3.14 Star Formation Timescale for knots > 20kpc from JO201. 91

4.1 The unwinding galaxy sample, showing whitelight images of each galaxy with the Halpha emission line flux overlaid. The figure shows the Halpha tails extending far beyond the disks in some cases, whilst maintaining a clear spiral arm pattern. 100

4.2 Comparison between ionised gas and stellar kinematics maps in JO201. 102

4.3 Comparison between ionised gas and stellar kinematics maps in JO200. 103

4.4 Projected position vs. velocity phase-space diagram of the unwinding sample, showing thumbnail images of each galaxy. 106

4.5 Plot of metallicity for the "unwrapped" disk of JO201, showing radial projected distance from the centre against azimuthal angle. 108

4.6 Plot of metallicity for the "unwrapped" disk of JO200, showing radial projected distance from the centre against azimuthal angle. 108

4.7 Unwinding galaxies shown in white light, overlaid with contours comparing the oldest and youngest stellar populations. 110

4.8 JO194 shown in white light, overlaid with four stellar age bins. 111

4.9 JO85 shown in white light, overlaid with four stellar age bins. 112

4.10 Kinematics comparison between JO200 and a simulated galaxy undergoing edge-on stripping. 115

4.11 Timestep snapshots of a simulated galaxy undergoing edge-on stripping, moving partially along the line-of-sight. 118

4.12 Timestep snapshots of a simulated galaxy undergoing edge-on stripping, moving along the plane of the sky. 119

4.13 Timestep snapshots of a simulated galaxy undergoing face-on stripping. 120

List of Tables

3.1 List of emission Lines considered in this analysis, with their corresponding wavelength in air. 72

4.1 Sample of GASP jellyfish galaxies with unwinding spiral arms. 99

4.2 Comparison of pitch angles in the disks and tails of unwinding GASP jellyfish galaxies. . . . 107

Chapter 1

Introduction

This chapter consists of some extracts from the papers "GASP. II. A MUSE View of Extreme Ram-Pressure Stripping along the Line of Sight: Kinematics of the Jellyfish Galaxy JO201" (Bellhouse et al., 2017) and "GASP. XV. A MUSE view of extreme ram-pressure stripping along the line of sight: Physical properties of the jellyfish galaxy JO201" (Bellhouse et al., 2019), in addition to original text.

The study of galaxies in The Universe has progressed by leaps and bounds in the past century. From "The Great Debate" of 1920, in which Shapley and Curtis debated the very nature of galaxies and the universe, to the modern day with millions of galaxies being observed in extensive surveys and many intricate processes proposed and scrutinised. We continue to expand our knowledge of the behaviour and lifecycles of galaxies. The more we learn about galaxies in the universe, the more complex and detailed studies we require to further our knowledge, and it is impossible to say how far this rabbit-hole goes. This exponential growth of understanding has lead to many branches and niches opening up within the study of galaxy evolution.

The major theme in the history of extragalactic astrophysics over the latter half of the 20th century has been the study of galaxy evolution, in particular the relative importance of internal and external transformative effects on a galaxy's evolution. Whether galaxies inherit their properties from internal or environmental processes is known in extragalactic research as "nature vs nurture". Nature in this case refers to the processes within a galaxy which, excluding all other effects, would act to transform a galaxy in total isolation. External effects are those which a galaxy experiences due to its environment and surroundings, coined as "galaxian

sociology" by Haynes & Giovanelli (1984). As such, many studies over the past few decades have placed great importance on understanding the many possible effects and their dominant regimes.

As progress has been made over the years, technology has advanced contemporaneously, with more advanced observatories and instruments facilitating deeper, more precise observations, and with more powerful supercomputers enabling more in-depth, higher-resolution simulations. Consequently, more effective, focused studies have been possible, coevolving with our growing understanding of the cosmos.

Then, as new and exciting objects are serendipitously discovered with our ever-improving tools, new paradigms and fields of research open up and our understanding grows. Within a few years these new, previously inexplicable objects become the subjects of large surveys which give us huge insights into a new area of astronomy. This cycle repeats as we continue our journey through the redshifts and across the areas of the sky.

In more recent years, the progress of technology has facilitated the construction of survey telescopes which methodically image the sky and expand our view of the cosmos, building huge catalogs of many thousands of objects with imaging data, spectral data and even resolved spectroscopy. Such catalogs are of huge benefit to astronomers as they provide large unbiased samples for study, albeit at a lower resolution to a targeted survey. As technology improves, both the number of robotically imaged objects and the imaging quality improves, and on the eve of the launch of huge dedicated observatories such as the Large Synoptic Survey Telescope (LSST), Euclid, and radio telescopes such as SKA, we face a huge paradigm shift in the way astronomy can be conducted. With petabytes of data and millions of objects expected to be observed every year, dwindling are the days of manually scouring through catalogs to build samples, and more automated mechanisms are required. Previously, these have been as simple as thresholding a parameter, such as the luminosity or colour, but more elaborate techniques are constantly improving selection methods and options. Citizen science projects such as Galaxy Zoo allow many thousands of trained volunteers to categorise objects, and are proving their worth in ever more diverse fields. Modern computing techniques, in particular Machine-Learning, make it possible to have programmed, trained neural networks carry out visual selection, which cannot be described in traditional programming techniques. With each of these methods and even combinations of the two, it is becoming possible to build previously unimaginably large samples of galaxies from the millions of observed sources. Undoubtedly, this is going to open up an exciting new era of

"big-data" in astronomy in the coming few years.

Through the course of this thesis, the modern understanding of galaxy evolution will be presented through a review of the discoveries made in the past few decades, with a focus on the evolution of galaxies in rich galaxy cluster environments, which are the bustling cosmic cities in which countless processes act to transform and affect galaxies. Following this, current research and new results will be presented that highlight aspects of a particular evolutionary process known as ram-pressure stripping.

1.1 Structure Formation

In hierarchical models of galaxy formation, condensed dark matter haloes formed the "seeds" in which the galaxies we observe in the universe condensed (White & Rees, 1978). These dark matter haloes collapsed from the small density perturbations in the early universe. From this point, structure was able to grow hierarchically across all scales starting with galactic haloes and consecutively growing by accretion and mergers up to the scales of galaxy clusters. This growth of structure from small to large scales is a feature of a cold dark-matter model of the universe, known as ΛCDM.

ΛCDM pertains to a universe which consists of, in addition to normal baryonic matter, a cosmological constant Λ which refers to the expansion of the universe, or *Dark Energy*, as well as a component of cold Dark Matter (CDM). Cold in this definition refers to the Dark Matter (DM) particles being non-relativistic at the time they decoupled from the other components of the universe, which could include massive particles such as WIMPS, or alternatively other massive DM particle candidates such as primordial black holes. The alternative to CDM is, as might be expected, *Hot Dark Matter* (HDM), which pertains to the DM particles being relativistic at the time of decoupling. If this were the case, DM particles during early structure formation in the universe would have been able to escape from overdensities and smooth out small-scale structure, which would have precluded early galaxy formation in the primordial universe, conflicting with observations of high-z galaxies.

These initial small-scale perturbations gave rise to hierarchical structure growth in the matter-dominated era of the universe. The baryonic gas follows the dark matter in the process of galaxy formation, accreting into the potential wells of growing dark matter haloes and consequently undergoing heating by adiabatic

compression and shocks up to the virial temperature of its host (White & Rees, 1978). The resulting hot gas is thermally obstructed from collapsing gravitationally in order to undergo star formation, therefore it must cool radiatively in order to reach the sufficient density for stars to condense out of the accreting gas.

The cooling time is larger than the free-fall time for typical gas masses in cluster scale primordial haloes (Mo et al., 2010), therefore much of the gas remains in an extended hot gas corona in and around clusters. This is typically observed in X-ray observations of galaxy groups and clusters and the hot gaseous halo is known as the intracluster medium (ICM)

The dominant cooling mechanism in these systems is bremmstrahlung radiation, the cooling time of which is inversely dependent on the square of the density of the medium. The result of this is that at the centres of these extended hot gas clouds, cooling becomes more efficient, and a so-called "cooling flow" develops, allowing the gas surrounding the central region to collapse down under gravity. At larger scales, the cooling time remains longer than the Hubble time.

In smaller, more compact haloes which can cool more effectively, the gas collapses down to undergo star formation, giving rise to the early galaxies. A residual halo of hot gas however, is expected to remain as a pressure-supported plasma surrounding the galaxy. This halo is predicted by current models of galaxy formation (White & Frenk, 1991) and the existence of such extended gas clouds have been suggested to explain observed absorption lines in quasars (Bahcall & Spitzer, 1969). Furthermore, the presence of gas residing in hot gas haloes would explain why only a small fraction of the baryonic matter expected to reside in dark matter haloes is observed in the form of stars and cold gas (Fukugita & Peebles, 2004, 2006).

In an undisturbed scenario, this hot gas should be able to collapse fully within the Hubble time, therefore other processes must be preventing the hot gas halo from cooling in its entirety. This can be accounted for by introducing feedback mechanisms in which energy released by ongoing processes within the galaxy can prevent the residual gas from cooling.

In stellar feedback models, the energy released by supernova events can act to heat the gas halo surrounding the galaxy. In AGN feedback, energy originating from processes related to the central supermassive black hole further act to heat the surrounding gas cloud. Such processes can be divided into two mechanisms of AGN feedback: "Radio mode" feedback (Croton et al., 2006), where energy is released by continuous gas accretion onto the black hole, as well as "quasar-mode" feedback arising from gas inflow at a higher rate

resulting from galaxy mergers and disk instabilities (Bower et al., 2008).

Cosmological simulations which include stellar and AGN feedback processes in addition to radiative cooling predict that the stellar feedback is sufficient to prevent total collapse of the gas, leaving residual hot gas haloes around formed galaxies (Bower et al., 2008; Crain et al., 2010; van de Voort & Schaye, 2012). Furthermore, the effects of buoyancy and thermal conduction combined have been found to suppress the formation of cold clouds and inhibit the collapse of the halo, independently of feedback processes (Binney et al., 2009; Nipoti, 2010).

Contrary to the expectation, there remains a dearth of direct observations X-ray emission which should indicative of the presence of such hot gas haloes surrounding star-forming galaxies according to such models of galaxy formation. One explanation for this is that such galaxy formation models may overestimate the quantity of hot hydrostatic gas and thus the expected X-ray luminosity (Benson et al., 2000). Indeed, in-depth hydrodynamical simulations (Toft et al., 2002; Rasmussen et al., 2009) have found lower expected X-ray luminosities to those predicted by the analytical models, closer to the observed values. Hydrodymanical models such as Crain et al. (2010) which include the effect of the entropy of the hot halo gas being increased by supernova energy injection and by radiative cooling, which removes the lower entropy gas to form stars, find that the distribution of this hot gas becomes more widely spread than the host DM halo, resulting in an X-ray luminosity more consistent with observations (Anderson & Bregman, 2011; Dai et al., 2012).

A different explanation, pertinent in denser group and cluster environments, for the discrepancy in predicted X-ray luminosity from the observations is the presence of mechanisms which act to remove this diffuse hot gas from the surroundings of a galaxy, diminishing the mass of the halo and its X-ray emission as the gas mixes and combines with the surrounding intragroup medium or with the ICM in larger clusters. The wake of hot corona gas left by a galaxy moving through a cluster or group can mix with the ICM or intragroup medium respectively, forming a "warm-phase" mixture with a cooling time significantly shorter than the surrounding medium, which can be funnelled into the central galaxy as a fuel for further star formation (Zavala et al., 2012).

The hierarchical formation of structure the universe proceeds as larger objects are assembled through infall and mergers of individual galaxies (Press & Schechter, 1974; White & Rees, 1978; White & Frenk, 1991; Lacey & Cole, 1993; Springel et al., 2005). The formation proceeds from the smallest scales up to

progressively larger scales as gravitational interactions assemble into groups, filaments and ultimately into galaxy clusters, giving rise to the distribution of matter we see in the universe today, known due to its foam-like filamentary appearance as the "cosmic web".

1.2 Galaxy Evolution and Interactions in Clusters

Galaxies in The Universe evolve through a combination of internal and environmental processes. Instrumental to their evolution is the flow of gas into and out of galaxies, since cold gas is the fuel for star formation. Important discoveries from the past decades supporting this idea include the observation that galaxy morphology and colour correlate with environment and galaxy mass (e.g. Dressler, 1980; Baldry et al., 2006; Peng et al., 2010; Fasano et al., 2015; Vulcani et al., 2015).

Galaxies can accrue gas from their surroundings, supplementing the mass available for star formation, through accretion processes. Accretion of gas onto the galaxy disk is found to occur in two distinct modes. In the first case, inflowing gas which collides with the hot hydrostatic gas halo can experience an accretion shock, heating it almost to the virial temperature. This gas will then have to cool over a period much longer than the dynamical time before it can collapse onto the galaxy. This is known as "hot-mode accretion" Katz et al. (2003). In the case where the cooling time of the gas is sufficiently short, such as in lower mass haloes or denser clumps, the gas can accrete onto the galaxy without being substantially shock heated, thus the accretion rate is dependent on the infall time rather than the cooling time. Since denser clouds of gas can cool more effectively, so-called "cold-mode accretion" typically occurs when gas is channelled into a galaxy disk along filaments (Kereš et al., 2005; Dekel et al., 2009).

Internal processes which can remove the gas component include stellar feedback from high-wind stars such as Wolf-Rayet and OB type stars, supernova feedback, and the effects of AGN activity (Veilleux et al., 2005; Ho et al., 2014).

Dense environments such as groups and clusters can promote gravitational and hydrodynamical encounters which can drastically alter the morphology and composition of a galaxy.

Environmental processes can be separated into two categories: gravitational and hydrodynamical. Among the gravitational effects are tidal interaction between galaxies, common in moderately crowded environments

(Spitzer & Baade, 1951; Merritt, 1983; Toomre, 1977; Tinsley & Larson, 1979; Mihos & Hernquist, 1994; Springel, 2000). In higher-mass clusters, the galaxies may also be subjected to perturbation by the gravitational potential of the cluster as a whole (Byrd & Valtonen, 1990; Valluri, 1993a), giving rise to inflows as well as boosting star formation within the nuclear and disk regions. Over extended periods of time, cluster galaxies can also be affected by cumulative high-speed close-approach encounters with other cluster members (*harassment;* Moore et al., 1996, 1998).

Hydrodynamical interactions between galaxies and the intracluster medium (ICM) can remove their halo gas via *starvation/strangulation* (Larson et al., 1980; Balogh et al., 2000), or their interstellar gas via ram-pressure stripping (RPS; Gunn & Gott, 1972; Faltenbacher & Diemand, 2006; Takeda et al., 1984). Additional mechanisms such as thermal evaporation have also been proposed (Cowie & Songaila, 1977). In this section we break down a selection of the environmental processes that galaxies may encounter as they move through a cluster.

1.2.1 Tidal Interactions Between Galaxies

Tidal interactions between galaxies act upon the gas and dust as well as stellar and dark matter components of galaxies, with differing strength depending on the gravitational binding of each component. In moderately crowded environments, tidal interactions are effective at removing matter from galactic haloes (Spitzer & Baade, 1951; Merritt, 1983). Simulations of tidal interaction by Valluri & Jog (1990) find that the process is more effective at removing matter from the outskirts of galactic haloes than from the more gravitationally-bound inner regions.

In the denser environments within cluster cores the increased frequency of encounters proliferates the tidal interaction process, however the duration of each encounter is limited by the high relative velocities of the galaxies involved, reducing the overall effectiveness.

Observations and simulations (Kennicutt et al., 1987; Mihos et al., 1992) agree that the resultant effect of tidal interaction on galaxies is a rise in nuclear activity due to induced nuclear gas infall, as well as increased disk activity and a larger bulge to disk ratio.

1.2.2 Tidal Interactions Between Galaxies and the cluster potential

In higher-mass clusters, galaxies can be perturbed as they interact with the gravitational potential of the cluster as a whole, giving rise to inflows and causing the formation of bar features as well as boosting star formation within the nuclear and disk regions.

For galaxies rotating parallel to the orbital plane, the effect of the cluster potential can be to perturb the disk structure into a spiral pattern, whilst for galaxies rotating perpendicular to the orbital plane the interaction can lead to the formation or exaggeration of a bulge structure (Valluri, 1993b). In either case, the process can lead to a thickening of the stellar disk.

Another effect of interaction with the cluster potential can be the induction of star formation as the tidal forces accelerate molecular clouds within the galaxy, thereby increasing their kinetic pressure.

1.2.3 Mergers

In the densely populated regions of galaxy clusters, one of the most extreme and rapid transformational processes is the collision, or merging, of two galaxies during an encounter (Toomre & Toomre, 1972; Lavery & Henry, 1988; Mihos et al., 1993; Schweizer, 1996). Observations have found galaxy mergers to be among the strongest mechanisms for driving sudden star formation in interacting galaxies (Kennicutt, 1998). Merger events between galaxies are generally divided into major and minor mergers (Woods et al., 2006). Major mergers, those between galaxies of similar masses, are some of the most striking examples of galaxy collisions. Minor mergers are generally more common and occur when there is a significant mass ratio between the interacting galaxies, usually where a satellite or dwarf galaxy undergoes an encounter with a larger galaxy. Minor interactions can be drivers of the evolution of disk galaxies without necessarily destroying the disk morphology (Quinn & Goodman, 1986; Quinn et al., 1993). Major mergers, on the other hand, can completely disrupt the morphology of the interacting galaxies, channeling gas into the nucleus of the post-merger remnant, boosting star formation. The angular momentum of the interacting galaxies is likely to be disrupted and the resulting galaxy is typically a large early-type elliptical galaxy (Hernquist & Barnes, 1991). Depending on the gas content of the merging galaxies, mergers are classified as either “wet” or “dry”. Wet mergers, between gas-rich galaxies, can trigger star formation (Barton et al., 2000), AGN activity and

ultimately convert late-type gaseous galaxies into early type ellipticals (see Lin et al., 2008, and references therein). "Dry" mergers, on the other hand, occur between merging early type galaxies which have little gas content to lose and do not massively change the overall star formation activity, but play an important role in the growth of massive red elliptical galaxies (Tran et al., 2005; van Dokkum, 2005).

1.2.4 Harassment

Harassment is the name given to the resultant effect of many high-speed close-approach encounters between galaxies and the cluster potential as a whole. The strength of the effect is dependent on the collisional frequency and the strength of each collision, as well as the distribution of the galaxy and cluster potentials. Due to the nature of the process, harassment is expected to have a greater effect on galaxies in elongated orbits as opposed to circular ones. The cumulative effect of many such encounters heats the stellar component, diminishing the stellar angular momentum to increase the velocity dispersion. The gaseous component sinks toward the nucleus in the process (Moore et al., 1996).

Initially a large proportion of the stellar component (up to 50%) will be removed, however the central density will be increased, intensifying the binding energy and diminished the efficiency of any further stripping (Moore et al., 1998).

1.2.5 Viscous Stripping

Viscous stripping, first proposed by Nulsen (1982), can remove material from a galaxy in the form of a viscosity momentum transfer from the hot IGM onto the outer layers of the cold, dense ISM. If the flow is turbulent, this process may be sufficiently effective to boost ram pressure in stripping gas from the galaxy at a slightly higher rate than ram pressure from the ICM alone would achieve.

1.2.6 Thermal Evaporation

Thermal evaporation is a process which acts at the interface between the hot gas of a cluster or group and the cold interstellar medium (ISM) of a galaxy (Cowie & Songaila, 1977). When the thermal energy of the ICM or intragroup medium is high compared with the galaxy velocity dispersion, the ISM of galaxies may be

heated along the interfacing region. This may sufficiently raise the temperature such that the thermal energy of the gas overcomes the gravitational potential of the galaxy and evaporates. The effectiveness of the process is sensitive to the thermal energy of the cluster or group gas and is strongly minimised by the presence of a magnetic field within the galaxy (Vikhlinin et al., 1997). Overall, the effect of thermal evaporation is almost negligible in groups and a lower order effect with respect to other processes in clusters (Cowie & McKee, 1977).

1.2.7 Strangulation

Processes such as strangulation or starvation, in which the gas reservoir of a galaxy is removed leading to a slow cessation of star formation, can explain the shape of the morphology fraction outside 1 virial radius of a cluster, where other processes listed here have diminished effectiveness.

In normal galaxies, gas is reserved in an extended outer halo to replace that used up by ongoing star formation activity. Removal of this halo by RPS, viscous stripping or other methods outlined here would lead to slow quenching of the star formation as the galaxy's internal gas is used up and not replaced, over the course of several Gyr.

The slow cessation of the star formation produces a signature in the metallicity of the quenched galaxy, since the star forming process which continues with the remaining gas increases the metallicity compared to a similar galaxy in which star formation has been rapidly quenched. Study of the metallicity distributions of cluster galaxies (Peng et al., 2015) has found that strangulation is a primary mechanism for transformation in local galaxies within cluster environments with a typical timescale of 4Gyr. In cluster environments, strangulation alone has been found by Cortese et al. (2011) to be unable to reproduce the low gas content of Virgo cluster spirals and ram-pressure stripping is required in addition, in order to match the observed sample.

1.2.8 Ram Pressure Stripping

Galaxies moving at high velocities ($\sim$1000km s^{-1}) through a hot, dense intracluster medium (ICM) can be stripped by the intense ram-pressure as the cold gas reservoir is abruptly and violently removed, sometimes with spectacular morphological consequences, as demonstrated in Figure 1.1 for the spectacular example

Figure 1.1: *Top:* NASA/ESA Hubble space telescope image of the Jellyfish galaxy ESO 137-001, combined with data from Chandra X-ray observatory, revealing gas and dust removal from the inner disk in the optical image, as well as the extreme X-ray tail in blue.(*Image credits: NASA, ESA, CXC; original source:* `https://www.eso.org/public/images/eso1437e/`) *Bottom:* ESO VLT image of ESO 137-001 combined with Atacama Large Millimeter/submillimeter Array (ALMA) molecular gas map, showing intricate detail in the stripped molecular gas trailing behind the galaxy (*Image credits: ALMA (ESO/NAOJ/NRAO), P. Jachym (Czech Academy of Sciences) et al; original source:* `https://www.eso.org/public/images/potw1939a/`)

ESO 137-001. If the ram-pressure exerted on the galaxy by the ICM overcomes the gravitational pressure of the galaxy, this process can effectively remove the galaxy's ISM leaving only the extant stellar component, causing spiral galaxies to be transformed into lenticulars and dwarf irregular galaxies into dSph's.

In a seminal paper, Gunn & Gott (1972) showed that the ram-pressure exerted by the ICM on an infalling galaxy is proportional to the medium density and the square of the velocity of the galaxy relative to it.

$$(\mathrm{P_{ram}} \propto \rho v^2). \tag{1.1}$$

The galaxy will lose its gas if ram-pressure overcomes the limiting force per unit area,

$$\mathcal{F} = 2\pi \mathrm{G} \Sigma_s \Sigma_g, \tag{1.2}$$

which depends on the stellar and gas surface densities σ_s and σ_g respectively. This description, although simplified, reproduces very well the observed gas deficiencies of cluster galaxies (see e.g. Chung et al., 2007; Jaffé et al., 2015). Owing to the higher velocities and closer approach to the dense cluster core, galaxies on radial orbits are the most likely to undergo RPS (Abadi et al., 1999; Quilis et al., 2000; Vollmer et al., 2001). Recent hydrodynamical simulations have shown however that the efficiency of RPS is also a function of the inclination, with face-on encounters being typically more efficient at stripping than edge-on or inclined encounters (Abadi et al., 1999; Quilis et al., 2000; Vollmer et al., 2001). Since their lower mass diminishes their ability to retain a gaseous component, dwarf galaxies are in principle more strongly subjected to gas-removal than their large spiral counterparts. During the stripping phase, galaxies can exhibit largely disturbed optical or ultraviolet tails composed of young stars formed in-situ in the stripped gas (Kenney & Koopmann, 1999; Cortese et al., 2007; Yoshida et al., 2008; Hester et al., 2010; Yagi et al., 2010; Smith et al., 2010; Owers et al., 2012; Kenney et al., 2014; Ebeling et al., 2014; Fumagalli et al., 2014; Rawle et al., 2014; McPartland et al., 2016), for which they are often referred to as "jellyfish" galaxies. Some studies further suggest that gas removal by RPS may be accompanied by an enhancement in the star formation activity as the thermal instabilities and turbulent motions within the galaxy provoke collapse within cold clouds in the galaxy (Evrard, 1991; Bekki & Couch, 2003). In this short starburst period, the star formation activity can increase by as much as 2 times (Poggianti et al., 2016), however the removal of the HI reservoir leads

to cessation of the star formation in the long term and the galaxy eventually becomes quiescent (Fujita, 1998; Fujita & Nagashima, 1999; Haines et al., 2015; Jaffé et al., 2016; Vollmer et al., 2012). Observable effects of ram-pressure stripping include compression of the leading edge of the galaxy, in some cases leading to the formation of a bow-shock, with the stripped gas forming a diffuse tail trailing behind in extreme scenarios. (Chung et al., 2009; Jaffé et al., 2015) According to simulations by Vollmer et al. (2001), the central gas density of galaxies in near-edge on collisions can be increased up to ~ 1.5 times as outer gas layers stripped from the leading edge are accreted onto the core. For edge-on collisions, over 50% of the gas can be re-accreted. Throughout the RPS process the stellar disk remains largely undisturbed, however in the case of face-on interactions the stripped gas in the outer disk can exert tidal forces on the stellar component, increasing the velocity dispersion along the rotation axis and thickening the outer disk (Quilis et al., 2000). It has been found by Boselli & Gavazzi (2006) that RPS is effective in removing atomic HI from an object with velocity similar to or larger than the average cluster velocity dispersion. This is consistent with results found by Vollmer et al. (2001), who have managed to reproduce the observed radial truncation of HI disks.

1.2.9 Interplay Between Transformational Processes

Each of these transformation mechanisms may dominate within certain regions and environmental densities, however it is generally accepted that the average galaxy in a cluster will experience a combination of many of them throughout their infall and orbit within the cluster. It is also believed that in some cases, violent transformation mechanisms may trigger nuclear infall and AGN activity which further quenches star formation through AGN feedback. Galaxy disk features such as spirals and bars can lead to enhancement of central star formation, reducing the timescale over which environmental quenching that removes the outer gas content such as strangulation or weak ram pressure stripping will lead to complete shut down of star formation, as the galaxy uses its remaining reservoir at a higher rate.

Since there is an abundance of mechanisms by which galaxy star formation can be quenched, it is imperative that more detailed studies are carried out on individual galaxies and in particular, examples of galaxies which are in the process of being transformed. As discussed in the next section, new instruments and surveys will see the rise of such studies and allow a greater insight to be achieved into the nature of galaxy transformation.

1.3 Probes of Gas Stripping

- Atomic Hydrogen gas

  Some of the most compelling evidence of ram-pressure stripping has come from observations of neutral atomic Hydrogen (HI) in galaxies falling into massive clusters. HI observations trace the 21cm line of neutral atomic Hydrogen, which is an indicator of the galactic ISM and consequently, potential star formation. In the context of ram-pressure stripping studies, HI observations can reveal the disturbances to the ISM during a hydrodynamical encounter. Observations of the HI content of infalling galaxies have revealed long "tails" of stripped gas, truncated gas profiles and reduced gas fractions, convincingly demonstrating the efficiency of RPS in massive clusters (Haynes & Giovanelli, 1984; Cayatte et al., 1990; Kenney et al., 2004; Chung et al., 2009; Cortese et al., 2010; Vollmer et al., 2001; Jaffé et al., 2015; Yoon et al., 2017) and even lower-mass groups (Rasmussen et al., 2006, 2008; Jaffé et al., 2012; Hess & Wilcots, 2013).

- Molecular gas

  The molecular gas content of a galaxy offers a crucial insight into the quantity of gas available for star formation. The molecular gas makes up a large portion of the total gas mass in a galaxy and represents the gas phase in the ISM in which star formation occurs. The most commonly used tracer of H_2 is the ^{12}CO line, which has been found to closely follow a relation to the molecular gas mass (Maloney & Black, 1988) (see appendix of Kenney & Young, 1989, for a detailed summary on the ^{12}CO H_2 relation)

  Molecular gas studies show that while the H_2 component is vulnerable to RPS, it is much less affected than atomic gas (Kenney & Young, 1989; Boselli et al., 1997, 2014). This is attributed to the higher surface density of molecular gas and its location deep in the galaxy's potential well making it less susceptible to RPS. Correspondingly, the deficiency of HI with respect to the molecular gas is in part owing to the atomic hydrogen being dominant on the outer regions of the disk of the galaxy, which are more susceptible to stripping.

- Ionised gas

  Narrow-band imaging centered on the ionised Hα emission has also proven to be an excellent tool to

study gas stripping phenomena and the subsequent evolution of galaxies (Gavazzi et al., 2002b,a; Yagi et al., 2010; Fossati et al., 2012; Boselli et al., 2016, 2019). In particular, the Hα emission traces recent star formation activity on a timescale of $\sim$ 10Myr (Calzetti, 2013), making it useful for tracing star formation occurring during the ram-pressure interaction, which can result from the compression of the gas present in the disk, as well as the collapse of stripped gas in the tails (Kenney & Koopmann, 1999; Yoshida et al., 2008; Kenney et al., 2014; Boselli et al., 2018a; Fossati et al., 2018; Boselli et al., 2018b).

The Hα emitting gas is ionised by ongoing local star formation, making it an indirect tracer of the SFR. An alternative, direct, tracer of the SFR comes from UV emitted by young stellar photospheres. UV observations are therefore used as an indicator of star formation as the UV band is where young stars emit the majority of their energy. The UV emission is sensitive to longer-term star formation compared to Hα, on a timescale around 100Myr (Calzetti, 2013) and is less sensitive to rapid recent changes in SFR than Hα.

- X-ray emission

  The hot, dense ICM of a galaxy cluster is a strong source of thermal bremmstrahlung radiation in the form of X-ray emission (Jones & Forman, 1999). This allows the ICM density, mass and temperature to be probed using X-ray observations, which gives an insight into the distribution and nature of the ICM. Any merger events causing disturbances to the hot cluster gas can therefore be inferred from the residual evidence of turbulent events, such as sloshing of the gas caused by infalling groups and previous merging of clusters. Since mergers of clusters and infalling groups are likely to result in the occurrance of ram-pressure stripping events, knowledge of the X-ray ICM distribution is useful in Jellyfish galaxy studies. Infalling galaxies can also be evident in disturbances to the ICM distrubution in X-ray emission.

- IFU studies

  The dawn of the Integral Field Unit (IFU) era has revolutionised the study of jellyfish galaxies, enabling the resolved analysis of spectral features across the extent of a galaxy and its tails. This has made possible studies that have given us a much more in-depth understanding to be reached of individual galaxies undergoing RPS. (Merluzzi et al., 2013; Fumagalli et al., 2014; Fossati et al., 2016). Jellyfish galaxies are incredibly complex objects, kinematically and physically. The strength of IFU studies is

that they allow the "dissection" of these galaxies, differentiating the plethora of different environments and processes which reside within.

1.4 Previous Studies of Ram-Pressure Stripping

Since jellyfish galaxies represent a transition period of galaxies prior to quenching in the cluster environment, they have been the subjects of many studies, both observation and simulation based. In this section, a few such studies have been presented and summarised to give an overview of progress in the field to date.

1.4.1 Observations

In Kenney et al. (2004), HI observations were taken with the Very Large Array (VLA) of the galaxy NGC 4522, finding a truncated HI component in the disk of the galaxy, and extraplanar HI gas forming a tail to one side of the galaxy. The presence of this tail, coupled with the lack of disturbance to the stellar disk, was found to be consistent with ongoing ram-pressure stripping over any gravitational interactions. In addition to being spatially offset to the galaxy, was also found to be blueshifted with respect to the galaxy disk, toward the mean cluster velocity. The tail was found to by asymmetric, which the authors ascribed to the stronger ram-pressure experienced by the side of the disk rotating into the wind.

The 21cm HI observations of NGC 4522 were carried out using the VLA and compared with Hα maps taken in Kenney & Koopmann (1999). A large surface density was found for the HI tail, much larger than typically expected for extraplanar gas. The HI spectral line profile in the tail was found to exhibit a velocity offset $\sim$ 50km s^{-1} blueward of any disk velocity.

The authors found that the ram-pressure required to produce the disturbances observed was expected to be much higher (by an order of magnitude) than would be present at the location of the galaxy, invoking standard assumptions. This was attributed to possible large-scale ICM motions augmenting the relative velocity of the galaxy, evidenced by presence of ICM shocks in the region. This may be the result of subcluster merging between M49 and Virgo stirring the ICM.

In the study Ebeling et al. (2014), a sample of 6 jellyfish galaxies discovered in the Massive Cluster Survey were presented, observed in visible light with the Hubble Space Telescope. The galaxies were identified as

part of a two-step process to build a catalog of galaxies undergoing ram-pressure stripping events, where the first step was to manually identify a training sample by visual inspection. These would then be used to construct color magnitude criteria for selection of a larger sample of galaxies which may be undergoing similar transformations, albeit with less visually conspicuous signs of stripping. The production of such a sample was later outlined in McPartland et al. (2016). The selection criteria employed were 1) "Strongly disturbed morphology indicative of unilateral external forces", 2) "a pronounced brightness and color gradient suggesting extensive triggered star formation" and 3) "compelling evidence of a debris tail". Additionally, the implied directions of motion from each of these criteria should be consistent. Galaxies suiting all three criteria were selected as prime candidates, whilst galaxies satisfying two out of the three were considered in the latter study as part of the training data. The visually selected galaxies in the sample exhibited different degrees of morphology disturbance and star formation, the latter of which was ascribed to the galaxies undergoing different stages of ram-pressure stripping, i.e. due to the star formation rate changing with time as the gas removal proceeds.

The paper by Fumagalli et al. (2014) and the follow-up paper Fossati et al. (2016) focused on MUSE observations of an extreme example of a galaxy undergoing ram-pressure stripping, ESO 137-001. The first paper presented the data and characterised the stripping undergone by the galaxy. The second paper investigated the gas properties in the stripped material, such as the metallicity, ionisation parameter and ionisation mechanisms. The galaxy was observed using the MUSE IFU instrument allowing resolved studies of the spectral features to be carried out. The distribution of the Hα emission was obtained by fitting the zeroth, first and second order moments of the emission line in each spaxel across the cube. From this, maps of the kinematics in the stripped tail were produced, as well as the spatial extent of the Hα emitting ionised gas.

The Hα stripped tails were found to extend > 30kpc continuously and are surrounded by clumps, some of which had previously been confirmed as HII regions. The primary tail was confirmed to be stripped material originating from the central region of the galaxy, indicating that the galaxy is in a later stage of intense stripping which has ablated material down to the central few kpc of the galaxy disk. The velocity of the material in the tail was found to show no gradient from the galaxy, suggesting that the stripping is almost exclusively on the plane of the sky. Furthermore, the stripped material was found to be rotating with the

stellar disk up to $\sim$ 20kpc downstream, before turbulence overcomes the uniform rotation.

In the follow-up paper Fossati et al. (2016), the physical properties of the disk and tails of ESO 137-001 were derived from resolved emission line ratio studies. Evidence was found for shocks as an ionisation source in the tails, whilst photoionisation dominated the disk and leading edge. The HII regions were found to have metallicities close to solar, and were present only in the less turbulent regions of the tail.

1.4.2 Simulations

The paper Kapferer et al. (2009) presents a study of the dependence on ram-pressure strength of star formation and the distribution of components of galaxies, using N-body hydrodynamical simulations combined with radiative cooling, star formation and stellar feedback. In the study, the star formation was found to be boosted by more than 10 times under the influence of intense ram pressure. In particular, this star formation enhancement was found to be more dependent on the ICM density than the relative velocity. Many of the stars formed in the wake were found to fall back onto the disk, developing an enlarged bulge structure. The complex velocity field in the tails caused by the combination of the ram-pressure and the disk rotation was found to produce velocity structures which would survive up to several 100Myr. Particularly, self gravitating structures formed form the stripped spiral arms were found to evolve into the star forming regions in the tail. Finally, simulated observations in X-ray, Hα and HI were produced and features were analysed at different ram-pressure intensities. The HI component was found to be extremely sensitive to ram-pressure intensity, with the highest simulated ram-pressure almost completely removing the cold gas component. The X-ray simulated observations found a bright spot in the wake caused by compressional heating of the stripped gas, which is more concentrated in the most extreme ram-pressure scenarios.

Tonnesen & Bryan (2012) carried out high-resolution simulations of galaxies undergoing ram-pressure stripping including radiative cooling and star formation with thermal feedback. The simulations found that the star formation was diminished in the galaxy within a few 100Myr as a result of the stripping process. The RPS process was found to slightly increase the bulge mass relative to a galaxy evolving in isolation. Stars were found to form in the stripped tails where the low density gas cools and collapses into dense clouds. Finally, the star formation rate in the tails was predicted to be dependent on the ICM pressure, with more massive clusters facilitating more highly star-forming tails due to more cold, dense gas being formed in the

wake of the stripped galaxy. Importantly, the impact of stripping to the intracluster light (ICL) was found to be small; less than 1% of the stripped material becomes stars which contribute to the ICL, suggesting that other processes are more dominant in growing the ICL.

Roediger et al. (2014) present hydrodynamical simulations of RPS events, including star formation and stellar feedback, with a focus on structure and dynamics in star formation in the remaining disk and the near tails. The jellyfish morphology was found to be reproduced in both face-on and edge-on ICM wind scenarios. Furthermore, ram-pressure acting on existing tails will not instantly alter their direction, hence galaxies falling back onto a cluster may proceed for a time with misleading tail directions. In galaxies rotating as they fall edge-on into the wind, an asymmetry was found to be built in the tail due to the differential ram-pressure in the rotating disk. The authors also found as in Tonnesen & Bryan (2012) that less SF enhancement was observed in the simulated stripping than expected from gas disturbance resulting from the collision. This was attributed to the simulation resolution, as the greatest star formation enhancement would be expected in regions with low initial density, rather than those which are already high. Finally, the tails were found to be able to persist up to a few hundred Myr after ram-pressure stripping events, and were not as collimated as those in some observed galaxies such as ESO 137-001 (Fumagalli et al., 2014), which may be due to thermal conductivity in the ICM or magnetic fields, or due to differences in the ICM wind velocity with time resulting in different tail morphologies.

1.5 GASP

1.5.1 Outline of the GASP survey

The work presented in the papers that make up the chapters of this thesis is based on data taken in the GASP (GAs Stripping Phenomena in galaxies with MUSE) survey (Poggianti et al., 2017b). The GASP programme is a spatially-resolved spectroscopic survey of the gas-removal processes in a sample of 114 disk galaxies at redshifts $0.04 < z < 0.07$. The GASP targets were chosen from the jellyfish candidate sample of Poggianti et al. (2016), drawn from the WINGS, OMEGAWINGS and PM2GC catalogs. Galaxies were selected to span a wide range of galaxy stellar masses ($10^{9.2} - 10^{11.5}\mathrm{M}_{\odot}$) and environments (dark matter halo masses range from $10^{11} - 10^{15.5}\mathrm{M}_{\odot}$). The sample selection was carried out by visual inspection of B and V

band images, identifying morphological signatures suggestive of ram-pressure stripping. The chosen galaxies were given a value JCLASS from 1 (weakest) to 5 (strongest) based on the visual extent of stripping.

The galaxy coverage in GASP resulting from the $1' \times 1'$ field of view of MUSE amounts to $50 - 100$kpc from the galaxy centre, crucial for analysing the diffuse gas tails and extraplanar features of each galaxy. In cases where the extent of a galaxy and its stripped material exceeded the coverage of a single MUSE observation, two observations were taken and combined into a mosaic during the reduction process to obtain the full coverage.

Some of the core aims and motivations for GASP include the following goals:

- To better understand the process of gas removal from infalling galaxies. From where is the gas removed, under what conditions and what quantity of gas is stripped throughout infall?
- To investigate the effects of stripping and gas removal on the star formation activity and quenching of jellyfish galaxies.
- To investigate the interplay between ram-pressure stripping and AGN activity in galaxies with active nuclei in their central regions.
- How does the metallicity and star formation history of stripped galaxies compare with galaxies prior to stripping, or in the absence of hydrodynamical interactions?

1.5.2 Observations

The selected galaxies in the GASP programme were observed using the Multi Unit Spectroscopic Explorer (MUSE), a second generation integral-field spectrograph which saw first light on 31/01/2014, mounted on UT4 of the Very Large Telescope (VLT). In the standard wide-field mode (WFM), provide a 1×1 arcminute field of view with a spatial sampling of 0.2×0.2 arcseconds, and a spectral range of 4800-9300 Å (can be extended blueward to 4650 Å). The spectral resolving power of the instrument ranges from 1770 at 4800 Å to 3590 at 9300 Å.

The MUSE instrument divides the field of view into 24 channels, each of which is directed into one of 24 individual IFU modules. Each IFU module subdivides the image into 48 slits which are directed into a

spectrograph. Volume phase holographic gratings in each spectrograph then split the light into spectra, which are directed onto a $4K \times 4K$ CCD. The images recorded by the detector are recombined and the resultant data product is a cube of 2 dimensions in space and one spectral dimension. As of 2018, in addition to the WFM configuration, MUSE offers a narrow-field mode (NFM) for detailed study of more compact objects, with a field of view of 7.5×7.5arcseconds and a sampling of 0.025×0.025arcseconds. For the purposes of this study, the WFM was used as it offers a sufficient field of view to image the extent of each galaxy and its tails. An adaptive-optics facility was commissioned for MUSE in 2017 for the WFM and, at the time upcoming, NFM configurations. The system, known as GALACSI, is comprised of a 4-laser guide star facility (4LGSF) as well as a deformable secondary mirror (DSM) mounted on UT4. Sodium atoms in the upper atmosphere are excited by the 4LGSF and the emitted light is read by wavefront sensors mounted on the telescope, allowing the measurement the wavefront error introduced by the Earth's atmosphere. The correction to the wavefront error is applied to the DSM. The AO system operates at a frequency of 1000Hz, constantly correcting the wavefront distortion by the atmosphere and minimising the FWHM in poor seeing-conditions.

1.5.3 GASP results and Notable Galaxies

In the initial GASP studies, the focus was on individual case-studies of some of the more prominently stripped and more conspicuous galaxies. Several studies were published on these individual candidates, verifying ram-pressure as the origin of the disturbance and understanding what processes were occurring inside the galaxies and their tails. A set of the most distinctive (JCLASS=5) galaxies were chosen for individual study: including JO206 (Poggianti et al., 2017b), JO204 (Gullieuszik et al., 2017), JO201 (Bellhouse et al., 2017, 2019), JO36 (Fritz et al., 2017) and the unique example JO171 (Moretti et al., 2018a), a Hoag's-like galaxy undergoing RPS. The Hoag's galaxy is a particular object discovered and suggested to be a "pathological" galaxy by Hoag (1950). The object is composed of a central spheroidal core surrounded by a completely detached ring of young stars and gas likely formed by an accretion event in the past few (2-3) Gyr (Schweizer et al., 1987). JO171, a galaxy which closely resembles Hoag's object, is additionally experiencing ram-pressure stripping, more recently than the accretion event which formed the ring structure. In the individual case-studies, the MUSE data were analysed, exploring in particular the Hα distribution in the disk and tails, the ionised gas kinematics and the resolved emission line ratio diagnostics across the galaxy and tails. All of these galaxies

were found to have Hα emission in the disk and extending out into the tails. The stripped material in each case retains some semblance of the rotational velocity of gas in the disk. Where stellar components were analysed through via line fitting, the older stellar populations were found to be localised only within the galaxy disk and the bulk of star formation in the tails occurred within the last 20Myr, consistent with a hydrodynamical interaction over a gravitational one. Where line-ratio diagnostics were measured, the ionisation mechanisms followed the same general pattern of photoionisation dominating the emission in the disk and the clumps within the tails of the galaxies, with composite emission throughout the diffuse stripped material surrounding the disk and in the tails. In many of the JCLASS=5 galaxies, the central regions were dominated by AGN-type emission and were, previously or later, confirmed to be hosting AGN. This common feature was later examined in one of the sample-orientated GASP papers.

Following the case-studies of individual galaxies of interest in the GASP catalogue, several studies were carried out with the focus being on general trends in the population. One such study Poggianti et al. (2017a), focused on the aforementioned trait shared by several of the most compelling stripped galaxies; the presence of an AGN in their central regions. The study presented the 7 JCLASS=5 galaxies from the GASP sample, of which 6 were found to host AGN. This high incidence of AGN among extreme Jellyfish galaxies hints at a link between ram-pressure stripping and AGN activity. Such a link points to two possible scenarios, either: 1) The process of ram-pressure stripping may trigger the AGN through funneling of gas into the central region, resulting infall of matter onto the supermassive black hole. 2) The presence of AGN gives rise to more efficient stripping by way of decreasing the binding energy of the ISM through energy injection, making it more susceptible to removal. In analysing the location of each galaxy in position-velocity phase-space, a trend was found with all of the AGN hosting jellyfish lying in the "peak stripping" region with high velocities close to their cluster centres. Such a trend is strongly indicative that the intense stripping has given rise to the AGN, rather than the other way around. If the AGN was enhancing the stripping, there is no reason for this to occur preferentially in the most favourable region of phase-space for stripping.

Such a process indicates that RPS processes can give rise to even higher gas-loss rates if they trigger the AGN, giving rise to outflows which can dislodge and eject more gas from the inner regions of the galaxy disk than would be removed by ram pressure alone, thereby boosting the efficiency of the gas removal.

In Jaffé et al. (2018), a study of the locations of each galaxy in position-velocity phase space was presented,

constructing an orbital history of the galaxies and their stripping encounters. The diagnostic used locates each galaxy by its line-of-sight velocity relative to the cluster velocity dispersion and its projected radial distance from the cluster centre in cluster scale units. Such phase-space velocity diagrams reveal the key locations of interest in stripping processes, in which galaxies are likely to be encountering strong stripping due to their extreme line-of-sight velocities and proximities to the dense central regions of their host clusters. In the study, analytical models were used to identify the extent of this region of intense stripping. It was found that the sample of GASP jellyfish galaxies reside at higher peculiar velocities than the overall galaxy population at all clustercentric radii, implying that these galaxies are, in general, recently accreted into the clusters. Combined with their location in phase space within the region of expected intense ram-pressure stripping and the predicted orbital histories, the study concludes that the observed jellyfish sample consists of galaxies have been formed by intense incremental outside-in RPS on a timescale of $1 - 2$Gyr, encountered during first infall on near-radial orbits.

The study Vulcani et al. (2018) analysed the star formation rates within the sample of 42 GASP jellyfish galaxies in comparison with 32 field and cluster undisturbed galaxies on the integrated star formation rate-mass relation. The stripped galaxies were found to exhibit enhanced star formation in the disks, with additional star formation present in the stripped tail regions. This results in the sample of jellyfish galaxies occupying the upper envelope of the SFR-M_* relation and indicating that such stripping processes can give rise to periods of enhanced star formation in cluster galaxies.

In follow-up studies, many of the GASP galaxies of interest have been re-observed at other wavelengths in order to build a wider picture of the stripping process and its effect on galaxies. Studies in UV with Astrosat UVIT, CO with APEX and HI with VLA have been published, expanding the survey to ascertain the scope of RPS across the atomic and molecular gas and its effect on star formation in the UV. The UV study by George et al. (2019) of the jellyfish galaxy JO201 found a cavity in the UV emission corresponding to a similar deficiency in the Hα, co-spatial with the AGN emission. The paper concluded that such a cavity evidences star formation suppression by the AGN, which could be observational evidence that if the RPS process triggers the supermassive black hole in the galaxy, as per Poggianti et al. (2017a), this can more efficiently quench the galaxy by suppressing star formation from the inside out.

The CO study by Moretti et al. (2018b) found large amounts of molecular gas in the disks of four GASP

galaxies, with significant detections in two of the stripped tails, ranging out to a maximum of 40kpc. A clear correlation was found between the mass of molecular gas and the mass of Hα emitting ionised gas, and a possible offset was found between the velocities of the ionised and molecular gas detections, possibly due to the differential effect of ram pressure on the cold and warm gas components. Finally, the star formation efficiency was measured to be low in the tails, suggesting that the majority of the molecular gas will not be converted to stars before joining the ICM, however this will be confirmed with higher resolution data from ALMA. The atomic gas, studied in Ramatsoku et al. (2019) for JO206, was found to exhibit a similar tail to the ionised gas. The study found a high star formation rate in the galaxy and a short HI gas depletion time, with the star formation efficiency in the disk about 10 times higher than that in the tail.

1.6 JO201

Chapters 2 and 3 deal predominantly with one particularly unique jellyfish galaxy named in Poggianti et al. (2017b) as JO201. From all the GASP sample, the jellyfish galaxy JO201 is one of the most spectacular and complex examples of ram-pressure stripping at play. JO201 is particularly unique because it occupies a seldom explored region of position vs. velocity phase space: The galaxy lies at a very small projected distance to the centre (360 kpc) of the massive ($M_{200} = 1.58 \times 10^{15}$) cluster A85 and is moving with an extreme line of sight velocity of 3363.7km s^{-1} toward the observer (Poggianti et al., 2016; Bellhouse et al., 2017). This suggests that the galaxy is close to pericentric passage in a radial orbit and therefore is close to peak RPS. In most other cases, Jellyfish galaxies have their greatest velocity component along the plane of the sky, since the selection is, by design, biased towards galaxies with obvious long tails on the sky. As such, JO201 presents the opportunity to compare features of a jellyfish galaxy from a different perspective. Moreover, JO201 is interacting almost entirely face-on with the ICM, and hosts an AGN in its central region, which is believed to be connected to the stripping process (Poggianti et al., 2017a). The studies discussed in Chapters 2 and 3 of this thesis add JO201 to the small sample of jellyfish galaxies studied in depth to date, with the aim of stretching the RPS parameter space explored so far to its limits.

1.7 Thesis Plan

This thesis is divided into four major chapters. Chapter 1 introduces the relevant background on the subjects of cosmology, extragalactic astrophysics and galaxy evolution, as pertinent to the contents of the work outlined in the rest of this thesis. The current understanding of galaxy evolution and the relevant lines of modern extragalaxtic research are summarised. The mechanisms that have been proposed over the past few decades, which serve to evolve and transform galaxies, are outlined and compared. The different probes of gas stripping are outlined and detailed, across different wavelength observations and employing different tracers of stripping processes. Several notable works on the topic of ram-pressure stripping are shown, which have used observations or simulations to study individual galaxies or elements of the gas-stripping process. The GASP survey is introduced and the VLT instrument MUSE, employed to gather data in the GASP program, is detailed. Lastly, the galaxy known in the GASP programme as JO201, the subject of chapters 2 and 3, is introduced.

Chapter 2 consists of the paper "GASP. II. A MUSE View of Extreme Ram-Pressure Stripping along the Line of Sight: Kinematics of the Jellyfish Galaxy JO201" (Bellhouse et al., 2017), published August 2017. This chapter presents an investigation of the Hα spatial distribution and kinematics of the GASP galaxy JO201. The MUSE observations of JO201 are described and the analysis process is outlined, including correction of dust extinction and the fitting of emission lines. The environment of JO201 is analysed, obtaining its phase-space position within the cluster abell 85 in order to make predictions about the amount of stripping encountered by the galaxy. These predictions are then compared with the results of the MUSE data analysis and the velocity distribution of the observed stripped material.

Chapter 3 is drawn from the paper "GASP. XV. A MUSE view of extreme ram-pressure stripping along the line of sight: physical properties of the jellyfish galaxy JO201", published May 2019. This chapter presents the further analysis of JO201, exploring the physical properties of the galaxy as well as investigating the stripping history of JO201 through simulations. The timescale of star formation is calculated for star forming clouds in the tail and estimates are made using simulations of the timescale of the ram-pressure stripping as well as the physical length of the stripped gas tails.

Chapter 4 consists of material from the upcoming paper "GASP: Unwinding the arms of spiral galaxies

via ram-pressure stripping" (Bellhouse et al. in prep). The chapter presents an analysis of the morphological effects of the ram-pressure stripping process, in particular the "unwinding" effect observed in several GASP jellyfish galaxies. MUSE observations of several GASP galaxies are analysed and compared with simulations of galaxies experiencing an ICM wind at different orientations, in order to understand the effect of a galaxy's orientation on its stripped morphology.

Finally, Chapter 5 summarises the results of the previous chapters in the context of the modern understanding of galaxy evolution in The Universe.

Chapter 2

Kinematic Properties of a Galaxy Undergoing Ram-Pressure Stripping

This Chapter consists of the paper "GASP. II. A MUSE View of Extreme Ram-Pressure Stripping along the Line of Sight: Kinematics of the Jellyfish Galaxy JO201" (Bellhouse et al., 2017), published August 2017. The introduction has been abridged, since the background has already been given in Chapter 1, whilst some sections have been expanded within the paper.

The majority of the paper is of the author's original writing, with due credits for contributions to the text to Yara Jaffé for section 2.2 and George Hau for subsection 2.3.1.

2.1 Introduction

We present results from a new MUSE (Multi Unit Spectroscopic Explorer; Bacon et al., 2010) survey at the VLT called GAs Stripping Phenomena in galaxies with MUSE (GASP[1]), that aims to provide a detailed systematic study of gas removal processes in galaxies (see Poggianti et al., 2017b: Paper I).

[1] web.oapd.inaf.it/gasp

In this chapter we present a kinematical analysis of one of the most spectacular jellyfish galaxies in GASP, JO201 (WINGSJ004130.30-091546.1, also known as PGC 2456 and KAZ 364, RA 00:41:30.325, Dec -09:15:45.96), a heavily ram-pressure stripped galaxy in the massive galaxy cluster Abell 85. In section 2.2 we summarise the properties of JO201 and present a study of its local and global environment. In section 2.3 we describe the GASP MUSE observations, the data reduction process and the corrections used for Galactic extinction. Section 2.4 focuses on the Hα emission-line fitting processes and shows the resulting Hα emission maps. Section 2.5 presents the stellar and ionised gas kinematics of the galaxy, including velocity and velocity dispersion maps, as well as rotation curves. Finally, in section 2.6 we summarise all of the results and draw conclusions.

Unless otherwise stated, throughout the study we adopt a Chabrier initial mass function (IMF; Chabrier, 2003), and a concordance ΛCDM cosmology of $\Omega_{\rm M} = 0.3$, $\Omega_{\Lambda} = 0.7$, $\rm H_0 = 70 km\,s^{-1} Mpc^{-1}$.

2.2 JO201 and Its Environment

JO201 is perhaps the most convincing case of gas stripping in the sample of 419 (344 cluster and 75 field) jellyfish candidates of Poggianti et al. (2016). Its morphology is that of a spiral galaxy with tails of material to one side and its total stellar mass is $3.55^{+1.24}_{-0.32} \times 10^{10} \rm M_{\odot}$.

X-ray studies have classified JO201 as a Seyfert galaxy (Durret et al., 2005). Our MUSE observations confirm the presence of an AGN (see e.g. broadened emission-lines at the centre of the galaxy in Section 2.4), but we leave the study of the AGN activity in JO201 for a following paper (Bellhouse et al., 2019).

JO201 resides in Abell 85, a massive cluster with a velocity dispersion of $\sigma_{cl} = 982 \pm 55 \rm km\ s^{-1}$ ($M_{200} = 1.58 \times 10^{15} \rm M_{\odot}$), at a redshift of $z_{\rm cl} = 0.05586$ (Moretti et al., 2017). This cluster is part of OmegaWINGS and therefore has wide-field OmegaCam imaging ($\sim 1 \rm deg^2$) and spectroscopy from the Anglo-Australian Telescope. JO201 is located very close to the brightest cluster galaxy (BCG), with a projected radial distance (r_{cl}) of only 360 kpc ($0.15 \times R_{200}$), as can be seen in Figure 2.1. Moreover, JO201 has a very high line-of-sight velocity with respect to the mean velocity of the cluster ($|\Delta v_{cl}| = 3363.7 \rm km\ s^{-1} = 3.4 \times \sigma_{cl}$). In fact, it is outside the velocity cut originally considered for cluster membership ($3 \times \sigma_{cl}$; Moretti et al. accepted; Cava et al., 2009).

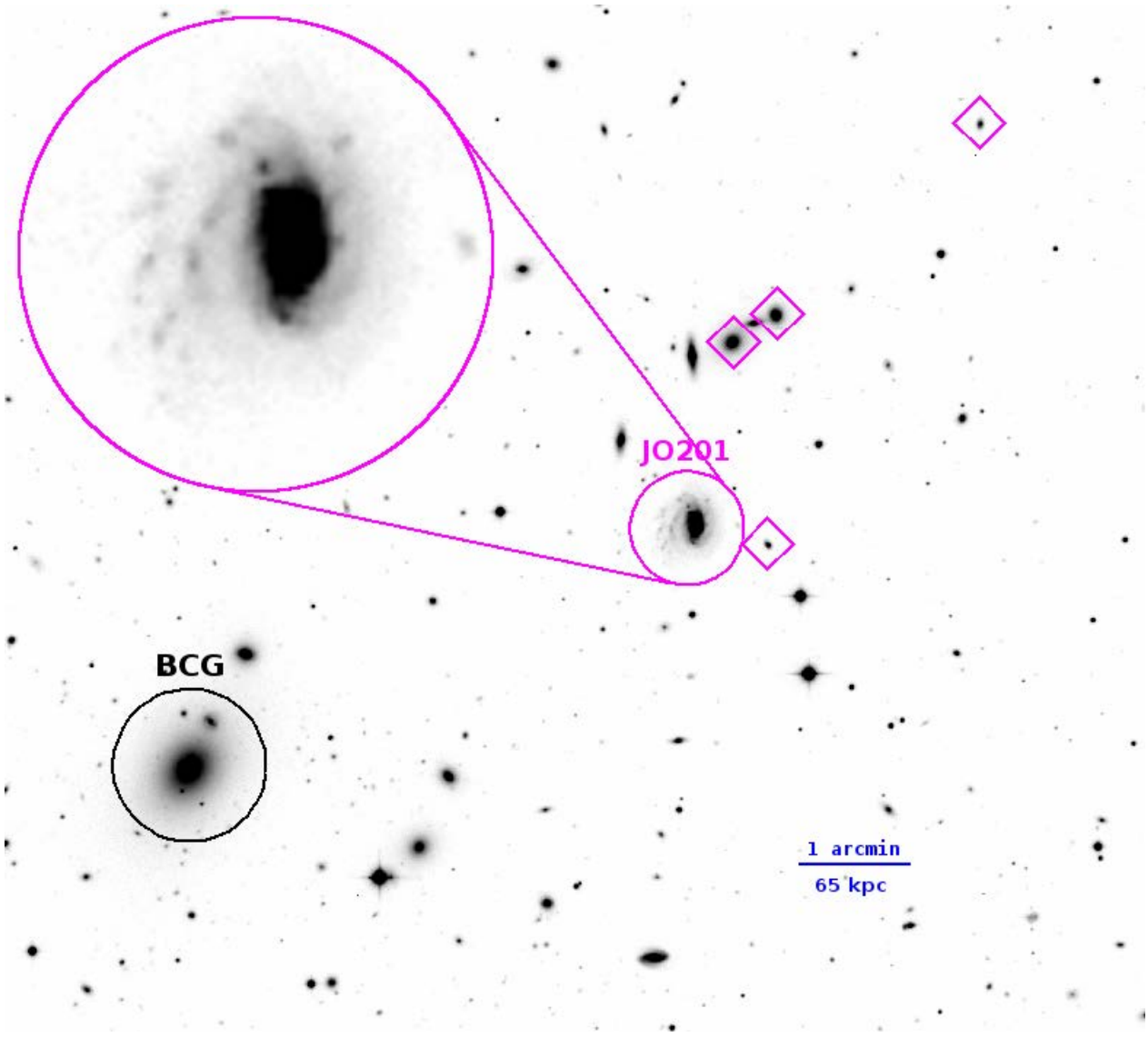

Figure 2.1: WINGS V-band image showing the central part of Abell 85. Highlighted are the BCG (black circle), the jellyfish galaxy JO201 (magenta circle and inset) and its possible group companions (magenta diamonds), selected from their kinematical deviations as described in the text. The distance between JO201 and the BCG is ∼5.6 arcmin (360 kpc at the redshift of the cluster). East is to the left and north to the top.

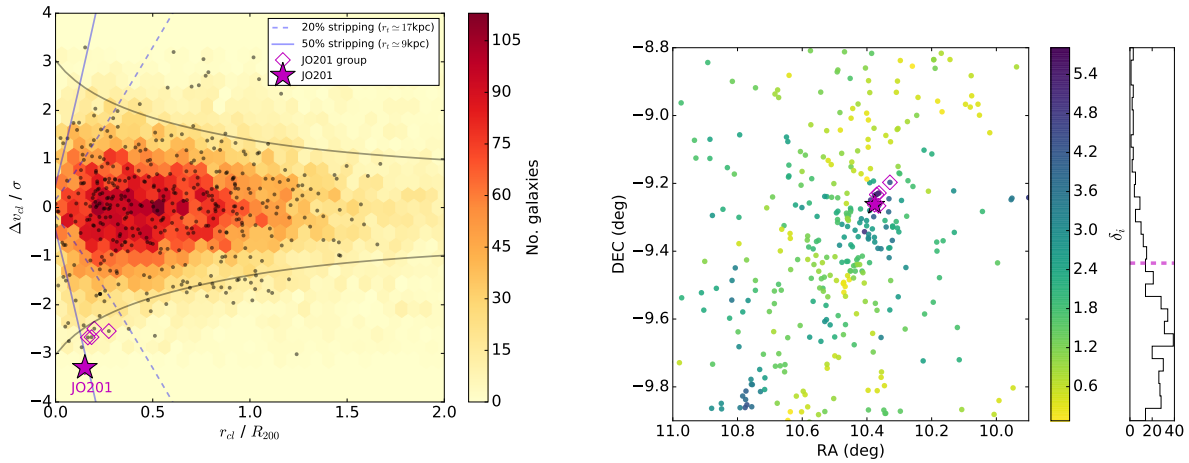

Figure 2.2: *Left:* Projected phase-space diagram of all the OmegaWINGS clusters (background density plot), where galaxies in Abell 85 are highlighted with gray circles. The gray curves represent the escape velocity in a Navarro, Frenk & White (1996) halo profile. The dashed and solid blue curves represent RPS models of JO201 by A85's ICM, in which 20% or 50% of the total gas mass in the disk has been removed (see text for details). *Right:* Dressler-Shectman "bubble" plot, showing the spatial distribution of galaxies in Abell 85, colour-coded by their velocity deviations δ_i. The magenta dashed line on the histogram shows $\delta_i = 2.5$, above which a galaxy may be considered to be part of a group or substructure. In both panels JO201 is marked with a magenta star and its possible group companions with open magenta diamonds.

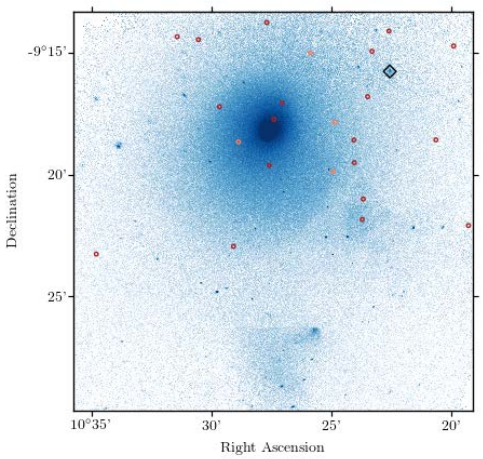

Figure 2.3: Chandra X-ray map of Abell 85 in blue, showing position of JO201 (black diamond) as well as OmegaWINGS galaxies (circles) of which spectroscopically confirmed cluster members are shown in dark red, and all others in orange. The figure shows a slight peak in X-ray emission around JO201, as well as bright, extended substructures in the south of the cluster.

The left panel of Figure 2.2 shows the projected position vs. velocity phase-space diagram of galaxies in Abell 85. All the cluster members with a spectroscopic redshift in Abell 85 are over-plotted (gray filled circles) on top of the distribution of all OmegaWINGS clusters stacked together (hex plot), and lie mostly within the trumpet-shaped region defined by the escape velocity of a Navarro, Frenk & White (1996) halo profile (grey curves). In this diagram, JO201 (magenta star) lies very close to the central region of the cluster in the "envelope" of the trumpet, which suggests that this galaxy is likely falling into the cluster for the first time. Its high peculiar velocity combined with its small r_{cl} also indicates a highly radial orbit. It is worth noting that JO201 is the most central and fast-travelling cluster jellyfish galaxy from the sample of Poggianti et al. (2016: see Jaffé et al. 2018).

Its location in phase-space suggests that the galaxy is falling into the cluster from behind and moving towards the observer. Although the line-of-sight component probably dominates the velocity vector, the galaxy's projected tails pointing eastwards (close to the direction of the BCG; see Figure 2.1), further suggest that the velocity vector must have some inclination with respect to the line-of-sight.

We quantify the ram-pressure intensity exerted on JO201 by the ICM in the same manner as in Jaffé et al. (2015). We utilise the cluster gas density distribution of Abell 85 presented in Bravo-Alfaro et al. (2009), computed from a hydrostatic-isothermal β-model (Cavaliere & Fusco-Femiano, 1976) as:

$$\rho(r) = \rho_0[1 + (r_{cl}/r_c)^2]^{-3\beta/2}, \tag{2.1}$$

where the core radius is $r_c = 82$ kpc, the central density $\rho_0 = 0.0257\mathrm{cm}^{-3}$, and $\beta = 0.532$ (values from Chen et al., 2007). The ram-pressure exerted on JO201 can be computed following Gunn & Gott (1972)'s equation: $P_{\mathrm{ram}} = \rho_{\mathrm{ICM}} \times v^2$, where ρ_{ICM} is the density of the ICM at the galaxy's position in the cluster and v the galaxy's velocity relative to the ICM. We adopt the projected cluster-centric distance (r_{cl}) and the line-of-sight differential velocity of the galaxy ($|\Delta v_{cl}|$) and obtain $P_{\mathrm{ram}}(JO201) = 1.24 \times 10^{-11} Nm^{-2}$. Note that due to the mass of A85 and the extreme speed of JO201, this value is over an order of magnitude higher than the estimated pressures computed for Virgo galaxies with HI tails in (Chung et al., 2007).

We can then compare ram-pressure exerted by the ICM on the infalling galaxy with the anchoring self-

gravity provided by the galaxy, defined as:

$$\Pi_{\rm gal} = 2\pi G \Sigma_{\rm s} \Sigma_{\rm g}, \tag{2.2}$$

where $\Sigma_{\rm s}$ and $\Sigma_{\rm g}$ are the density profiles of the stellar and gaseous exponential disks respectively, that can be expressed as:

$$\Sigma = \left(\frac{M_d}{2\pi r_d^2}\right) e^{-r/r_d}, \tag{2.3}$$

where M_d is the disk mass, r_d the disk scale-length and r the radial distance from the center of the galaxy. For the stellar component of JO201 we adopted a disk mass $M_{d,stars} = 3.55 \times 10^{10} M_{\odot}$, and a disk scale-length $r_{d,stars} = 5.56$ kpc, obtained by fitting the light profile of the galaxy from the V-band WINGS image[2]. For the gas component we assumed a total mass $M_{d,gas} = 0.1 \times M_{d,stars}$, and scale-length $r_{d,gas} = 1.7 \times r_{d,stars}$ (Boselli & Gavazzi, 2006).

These values yield $P_{\rm ram} = 0.008 \times \Pi_{\rm gal}$ at the centre of the galaxy, which is not enough to strip the inner gas. The condition for stripping ($P_{\rm ram}/\Pi_{\rm gal} > 1$) is met only when considering the galaxy is partially stripped (outside-in) down to a given "truncation radius", r_t.

By combining the stripping condition with equations 2.2 and 2.3 at $r = r_t > 0$, we find find that at the location of JO201 in phase-space, P_{ram} should have stripped the gas in JO201 down to $r_t \simeq$9 kpc, which is equivalent to $\sim$50% of the total gas mass stripped, estimated from the equation for remaining gas mass:

$$f = 1 + \left[e^{-r_t/r_d}\left(\frac{-r_t}{r_d} - 1\right)\right] \tag{2.4}$$

This is shown in the phase-space diagram of Figure 2.2 (left), where JO201 (magenta star) sits on top of the line corresponding to 50% gas stripping of JO201 in A85 (solid blue lines). We also plot the region corresponding to 20% of gas stripping (dashed blue lines; $r_t \simeq 17$ kpc) as a reference to the trajectory and stripping history of JO201 in phase-space. As we will see in Section 2.5.3, the extent of the non-stripped Hα emitting disk ($r \gtrsim 6$ kpc along the major axis) is comparable to the estimated r_t. Note however that r_t is

[2]We note that, although the light profile fitting reveals that JO201 is dominated by a disk component, there is a non neglible bulge component (20% of the light) that we ignore when estimating the ram-pressure stripping intensity across the galaxy. The bulge component however is confined to the central part of the galaxy. We also note that the value r_d obtained from V-band photometry is consistent with fits made to the stellar continuum (near Hα) using the MUSE datacube.

particularly difficult to measure in this galaxy due to the direction of stripping (see Sections 2.4 and 2.5).

We further study the local environment of JO201 by investigating the presence of substructures within Abell 85. We perform a Dressler-Shectman test (Dressler & Shectman, 1988), that consists of computing individual galaxy deviations by comparing the *local* (nearest neighbours) velocity and velocity dispersion for each galaxy with the *global* (cluster) values. We characterise the cluster by its mean velocity ($\bar{v}_{\rm cl}$), velocity dispersion ($\sigma_{\rm cl}$), and the total number of cluster members ($N_{\rm mem}$). Then, for each galaxy with $|\Delta v_{cl}| < 4 \times \sigma_{cl}$ (this cut includes galaxies with borderline membership, like JO201), we select a subsample of galaxies containing the galaxy i, plus its nearest 10 neighbors, and compute their mean velocity $\bar{v}^i_{\rm local}$ and velocity dispersion $\sigma^i_{\rm local}$. From these, we compute the individual galaxy deviations δ_i, following:

$$\delta_i^2 = \left(\frac{10+1}{\sigma_{\rm cl}^2}\right)\left[(\bar{v}^i_{\rm local} - \bar{v}_{\rm cl})^2 + (\sigma^i_{\rm local} - \sigma_{\rm cl})^2\right] \tag{2.5}$$

One way to investigate whether the cluster is substructured is through the "critical value" method, that compares $\Delta = \sum(\delta_i)$ with $N_{\rm mem}$. For A85, $\Delta/N_{\rm mem} = 1.7$, and, as explained in Dressler & Shectman (1988), a value > 1 is found in clusters with significant amounts of substructure.

The computed individual δ_i values are shown in the right panel of Figure 2.2, where groups of galaxies with high velocity deviations ($\delta_i > 2.5$, as indicated by the dashed line in the right-most histogram) are considered potential groups. According to this criteria several substructures are visible (e.g. at the centre and south-east). Our results are consistent with previous optical studies of A85 such as Bravo-Alfaro et al. (2008). Moreover, the high level of substructure found in A85 is in agreement with the findings of Ichinohe et al. (2015), who studied the cluster's X-ray emission and concluded that the cluster has undergone a merger event in the past, in addition to at least two currently ongoing mergers with galaxy groups, the effects of which can be seen in the substructures in the lower regions of the X-ray map in Figure 2.3.

To test whether JO201 is part of a substructure, we select galaxies in the vicinity of JO201 with $\delta_i > 2.5$ and study their velocity distribution. We find that 4 of these galaxies are likely forming a group with JO201, since they have similar line-of-sight velocities (see left panel of Figure 2.2). These galaxies are highlighted in Figures 2.1 and 2.2 with open blue and magenta diamonds respectively.

In summary, JO201 is a massive spiral falling into the massive galaxy cluster Abell 85 within a small

group of galaxies. Its projected position and velocity within the cluster suggests that it is crossing the cluster at supersonic speed in a radial orbit (mach ~ 3.2, for sound speed $\sim$km s^{-1} at the location of JO201 based on X-ray measurements from Ichinohe et al. 2015). The galaxy's motion through the cluster invokes ram-pressure on its disk, which has caused significant gas stripping ($\sim$50% of total gas mass). In the following sections we study the effects of RPS on this galaxy by comparing the distribution and kinematics of ionised Hα gas with that of stars.

2.3 Data

2.3.1 MUSE Observations

JO201 was observed on 2015-12-17, with photometric conditions and image quality of $\sim$0.7" FWHM, as measured from the stars in the Slow-Guiding System surrounding the MUSE field of view (see MUSE user manual[3]). A total of eight 675 second exposures spanning 2 adjacent fields were observed with the Nominal Mode, with an instrument rotation of 90 degrees and a small spatial offset between exposures as recommended by the MUSE User Manual. An internal illumination flat field was taken at the beginning of the observations for the purpose of illumination correction. A spectrophotometric standard star GD-71 was also observed right after the science target, for flux-calibration and telluric-correction. Standard calibration files as per the MUSE Calibration Plan were also taken.

2.3.2 Data Reduction

For data reduction, we followed the standard reduction procedures as described in the pipeline manual (Bacon et al., 2010: `www.eso.org/sci/software/pipelines/muse`), with minor exceptions. We used custom scripts for organising and preparing the raw data, which were then fed to ESOREX recipes v3.12, MUSE pipeline version 1.2.1. As the data have sufficient sky coverage, the sky was modelled directly and subtracted from individual frames using the 20% pixels with the lowest counts. After wavelength calibration using arc lamp exposures, the final wavelength adjustments were made using sky emission lines. The final, flux-calibrated

[3] `http://www.eso.org/sci/facilities/paranal/instruments/muse/doc.html`

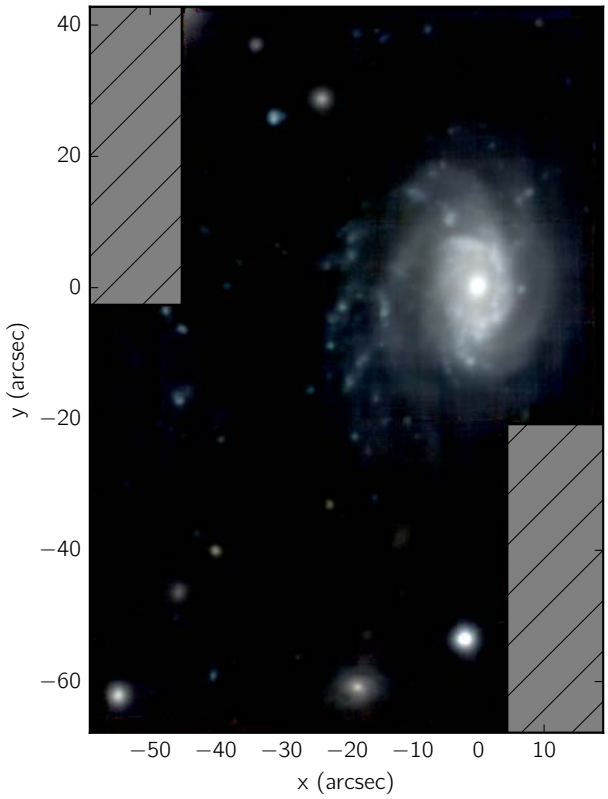

Figure 2.4: RGB image from JO201 GASP observation produced using 1000Å slices integrated from the datacube (B:5000-6000Å, G:6000-7000Å, R=7000-8000Å). East is to the left and north to the top. A series of bright knots to the east of the galaxy are seen connected by "bridges" of diffuse emission. The asymmetry of the disk and brightening of the western edge is suggestive of a bow-shock increasing the star-formation activity in the leading edge. On the far left are bright knots which are far removed from the galaxy and likely to have been stripped at a much earlier stage.

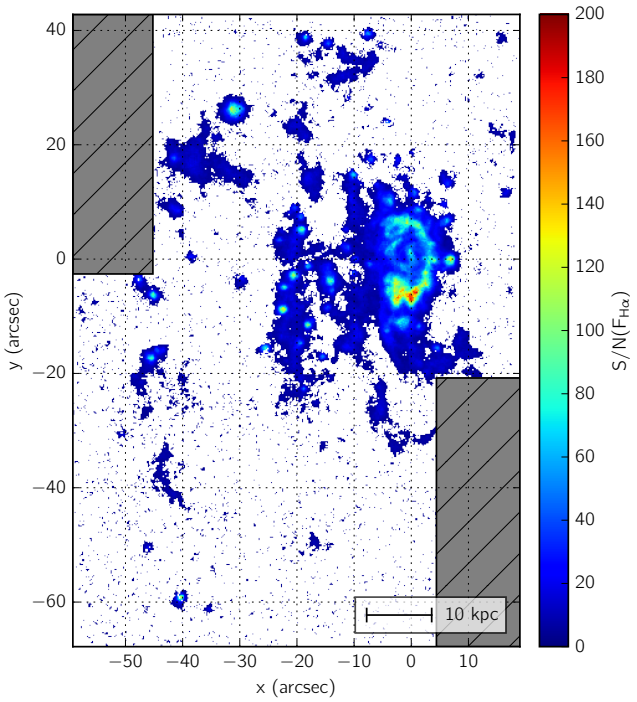

Figure 2.5: Hα signal-noise-ratio map calculated from the line fits to the MUSE data. The higher S/N ratios are seen in the areas of brightest $H\alpha$ emission in the western edge of the galactic disk and in the knots located eastwards of the disk. All fitted spaxels are shown with no signal noise cutoff applied in this figure.

data cube was generated by lining up and combining the individual frames using sources in the white light images. The final image quality is 0.8" FWHM in the reduced cube.

The full GASP data reduction process is described in greater detail in Paper I.

An RGB image produced using the reduced MUSE cube is shown in Figure 2.4. Visible in the image are a series of bright knots to the East of the galaxy connected by "bridges" of diffuse emission as well as slight morphological asymmetry in the disk. The western side of the disk shows a bright ridge of emission along an arc shaped pattern, suggestive of a bow-shock increasing the star-formation activity in the leading edge. On the far left of the image are bright knots which are far from the disk of the galaxy and are likely to have been stripped at a much earlier stage.

2.3.3 Galactic Extinction Correction

The observed spectra are subject to reddening by dust in the Milky Way, which must be accounted for prior to any analysis of the emission line fluxes. For the correction to be made, the amount of dust visible in the observed line of sight must be quantified. We estimated the contribution of dust using values from the galactic dust extinction and reddening tool on the NASA/IRSA infrared science archive, which uses measurements from Schlafly & Finkbeiner (2011) to quantify the dust distribution and give an extinction estimate across the cube. The extinction obtained of $E(B-V) = 0.0319$, $A_V = 0.0987$ was used in the Cardelli extinction law (Cardelli et al., 1989) to obtain a correction which was applied to the spectrum of each spaxel across the cube. The corrected cube was then used in all subsequent analyses.

2.4 Emission-Line Fitting

By fitting model profiles to the emission lines, the spatial distribution of different emission lines as well as the peculiar velocity and velocity dispersion of the emitting gas can be derived. In order to fit emission lines, the IDL custom code KUBEVIZ (Fossati et al., 2016), written by Matteo Fossati and David Wilman, was used. KUBEVIZ fits a set of predefined emission lines across the spectrum using models with up to two gaussian components or using moments.

2.4.1 Single-Component Fits

The available lines in the fitting procedure were Hβ, [OIII], [OI], [NII], Hα and [SII], however this study will focus on the Hα (λ6563) emission, fitted alongside the [NII] ($\lambda 6548, 6583$) lines. Chapter 3 expands the analysis to cover the full range of emission lines. The line fitting was carried out on a cube smoothed spatially using the mean value within a 3×3 kernel, chosen to smooth the data sufficiently to produce successful fits in KUBEVIZ to S/N > 3, without significantly sacrificing spatial resolution.

The redshift used for fitting the lines in KUBEVIZ was set at $z = 0.045$, calculated by KUBEVIZ using the spectral position of the Hα line at the central point of the galactic disk.

As the noise values in the 'stat' datacube produced by the MUSE pipeline underestimate the total error, the option was selected in KUBEVIZ to compute the nominal standard deviations of the measurements after renormalising the covariance matrix assuming a reduced $\chi^2 = 1$ (Fossati et al., 2016). The continuum under each line was calculated between 80 and 200Å from each line, omitting regions containing other known emission lines and using values within the 40th and 60th percentiles. An initial value of 20km s^{-1} was set for the narrow linewidth to prevent KUBEVIZ returning an error when fitting regions with low velocity dispersion, in particular the upper region of the galactic disk and the central region of the star forming knot to the NE of the field.

Figure 2.5 shows the $H\alpha$ S/N map resulting from the line fits. We rejected fits with S/N < 3, as well as unrealistic fits flagged by KUBEVIZ, which have zero velocity or velocity error.

For each fitted spaxel the fitting process yielded a central wavelength, intensity, and width of the Hα line, that could in turn be converted into velocity, flux and velocity dispersion.

We visually inspected the emission-line fits and found that in most cases the fits describe the line profiles well. In some regions, however, the line profiles are more complex and thus multi-component fits were needed. Three example spectra extracted from different spaxels within the galaxy are shown in Figure 2.6. The top panel shows the central region of the galaxy where an AGN has clearly broadened the lines. In this case, two gaussian components (red and blue lines) fit the emission lines better than a single component. The middle panel shows a star-forming region (large Hα blob with high S/N NE of the galaxy disk, visible in Figure 2.5) well fitted by a single gaussian. In the bottom panel instead, we see non-gaussian emission (with

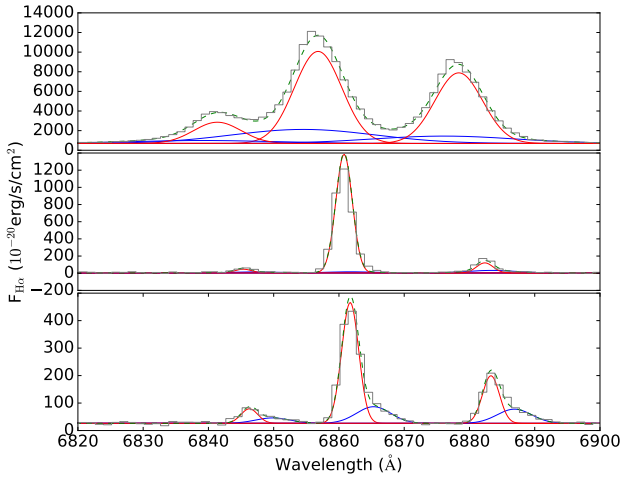

Figure 2.6: The observed Hα, NII emission line group in 3 different spaxels within JO201 (black histograms) together with a 2 component fit (red and blue curves correspond to individual component and the green dashed line their sum). *Top panel:* The central region of the galaxy, broadened by the AGN. *Middle panel:* A region within the north-eastern star-forming blob. *Bottom panel:* A region in the outer part of the disk displaying obvious tails redward of the emission.

one-sided wings) from a region in the outer part of the disk. As shown in Section 2.4.2, we find many of these non-gaussian emission lines in the galaxy. In some (more extreme) cases, two separate peaks can be distinguished (see bottom panels of Figure 2.7). As will be established and further discussed in the following sections, the shapes of the lines in these cases are indicative of gas trailing behind the disk of the galaxy, or even multiple physical blobs present in the same line of sight.

2.4.2 Double-Component Fits

Owing to the variety and complexity of the observed emission line profiles, in this section we present the two-component fits to the Hα emission across the galaxy. In the following sections, we will combine the two-component fits with single-component fits to construct maps of the emission in JO201.

We re-fitted all of the emission lines, using KUBEVIZ, setting two gaussian components to prioritise convergence on narrow and broad components of the emission, based on the value of their velocity dispersion. The resulting fits yield line centers ($\lambda_{\rm narrow}$ and $\lambda_{\rm broad}$), fluxes ($F_{\rm narrow}$ and $F_{\rm broad}$), and velocity dispersions ($\sigma_{\rm narrow}$ and $\sigma_{\rm broad}$) for each spaxel. From these parameters we could then investigate in each case which

component was the brightest or bluest and reveal which regions exhibited strong wings in the emission lines or double-peaking. As before, we rejected fits with S/N < 3 (in either component) as well as those rejected by KUBEVIZ.

For each fitted emission-line, flags were allocated based on the following parameters.

- 0 for spectra in which the narrow component is redward of the broad component. I.e. $\lambda_{\rm narrow} > \lambda_{\rm broad}$.
- +1 for spectra in which the narrow component is blueward of the broad component: $\lambda_{\rm narrow} < \lambda_{\rm broad}$.
- +2 where the narrow component is brighter than the broad component: $\mathrm{F}_{\rm narrow} > \mathrm{F}_{\rm broad}$.
- +4 where the separation between the two lines is greater than the sum in quadrature of their sigmas, Suggesting that two distinct lines are present: $\lambda_{\rm narrow} - \lambda_{\rm broad} > \left(\sigma^2_{\rm narrow} + \sigma^2_{\rm broad}\right)^{1/2}$.

For example, a region flagged as 5 will be comprised of flags +1 and +4, i.e. the narrow component will be blueward of and fainter than the broad component, with both components being significantly separated from each other.

Our flagging system allows the separation of different line profiles, as shown in Figure 2.7, where all the double-component line fits are split into the different flags. For this plot the fits were normalised to a standard velocity, width and height to facilitate their comparison.

It is interesting to map the location of the different line profiles in the galaxy. This is shown by the coloured regions in Figure 2.8.

Emission-lines with Flag < 3 are predominant in the centre of the galaxy. These fits correspond to cases where the 2 components are aligned or not significantly misaligned (see top row in Figure 2.7). The cause of these types of line profiles is the presence of an AGN. The active nucleus not only causes line broadening (Flag = 0), but, in some cases, it can generate outflows visible as mildly visible wings to one side of the broadened lines (e.g. Flag =1). Lines with Flags = 0, 1 and 2 account for 18% of the 2-component fits with $S/N > 3$.

Lines with Flag = 3 instead show skewed emission lines, exhibiting wings on the redward sides of bright emission lines. These trailing wing profiles are common (45%), and are typically found in the disk.

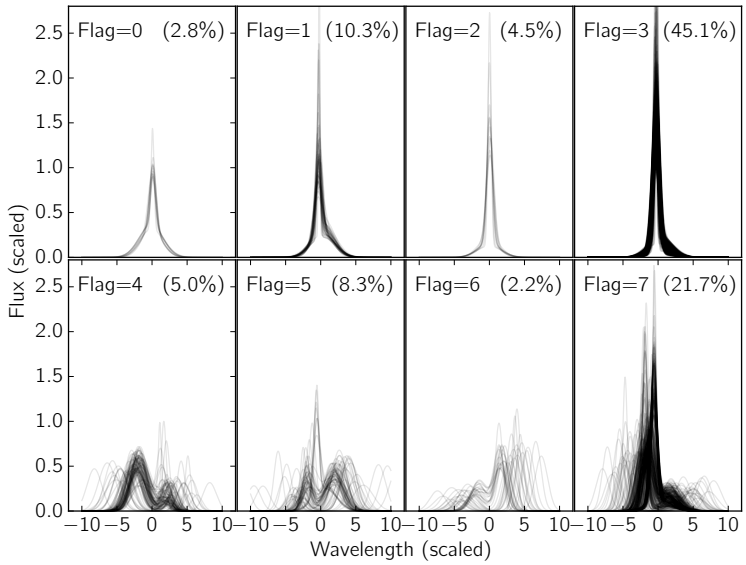

Figure 2.7: Profiles of double-component fits made to Hα emission lines in JO201, separated into the combined flags described in Section 2.4.2. Each of the plotted profiles has been normalised in position width and height to facilitate the comparison of the shape of the profiles. Percentages show the number of spaxels with each flag value out of the total number of spaxels fitted with 2 components. The flag values are mapped in the context of the galaxy in Figure 2.8.

Fits with Flag ≥ 4 are more extreme cases where there is a significantly displaced second component (37% of all 2-component fits, see bottom row of Figure 2.7). These types of fits were the best description of the emission lines in the regions around the edges of the galactic disk as well as the diffuse regions around the stripped tails. Their location and morphology are consistent with the scenario in which JO201 is primarily undergoing gas stripping along the line of sight, with the stripped gas being dragged behind the galaxy by ram pressure. The stripped material could be arranged either in the form of a physical tail behind the galaxy, or separate blobs along the same line of sight. This interpretation is in agreement with the environmental analysis presented in Section 2.2, and further supported by the kinematic analysis of the stellar and gaseous components of the galaxy, presented in Section 2.5.

2.4.3 Final Fits

To identify the best fit in each fitted spaxel we compare the results of the single versus double-component fits in each case. We use the S/N ratio of the single-component fit and the narrow and broad components of the double-component fits for this purpose.

We use the double-component fits when both the narrow and broad component are detected to greater than 3σ, otherwise a single component (also limited to 3σ) is used. Figure 2.8 shows the regions where double-component (colour) versus single-component (grey) fits are used. The figure shows that although single-component fits characterise well the emission in most parts of the galaxy, two-component fits are needed in the central region and in some parts of the disk and stripped tails.

Unless otherwise stated, the above mentioned combination of single and double-component fits is used in the rest of this analysis.

2.4.4 Hα Distribution

The spatial distribution of the fitted line flux in Hα is shown as red contours overlaid on the continuum fit from KUBEVIZ in Figure 2.9. It is visible in the figure that the emission from the Hα component shows a large offset, down to a surface brightness of $\sim 0.7 \times 10^{-18} \mathrm{erg\,s^{-1}cm^{-2}}$, from the disk of the galaxy due to the effect of RPS. Furthermore, the bright ridge of Hα on the west side of the galaxy may evidence the interaction with the hot ICM compressing the gas and forming a bow shock, increasing the star formation activity and thus

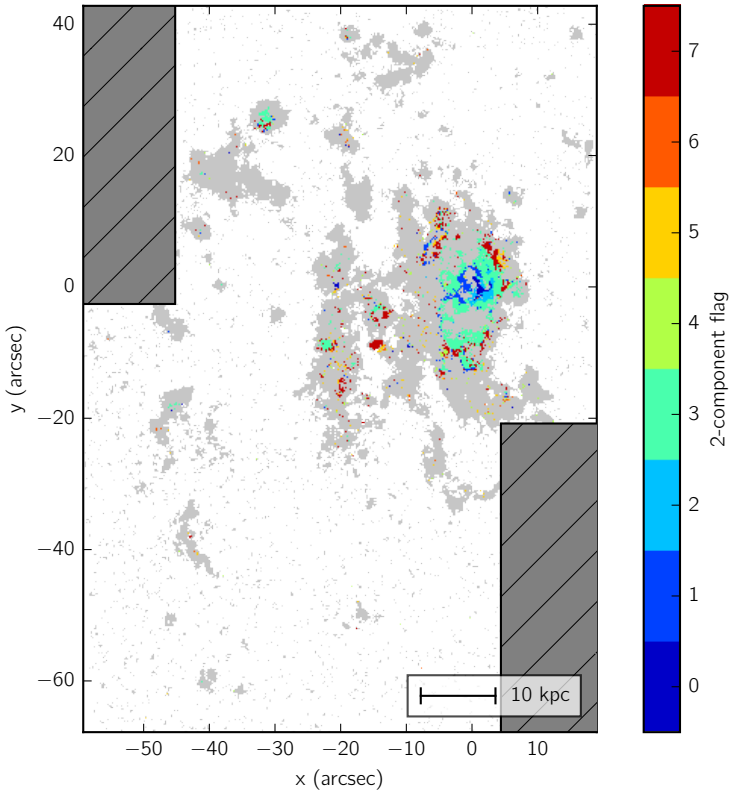

Figure 2.8: Map of fitted spaxels in JO201, separated into regions where double-component fits were used (coloured) or where single-component fits were sufficient to fit the Hα emission (grey). We chose the double-component fits when both the narrow and broad component were detected to greater than 3σ, otherwise a single component (also limited to 3σ) was used. Colours other than grey correspond to the flags attributed to each 2-component fit (c.f. Figure 2.7), as indicated by the colourbar.

the Hα emission. To the East of the galaxy disk (roughly in the direction towards the BCG, as shown by the arrow in the figure) the Hα emission is drawn out into "tentacles" of trailing gas which connect brighter knots. These knots are likely to be previously stripped gas which has collapsed under gravity to undergo intense star formation. The pattern of the diffuse emission and the collection of brighter knots observed in the plot suggest an unwinding of the spiral arm structure (see white dashed lines in Figure 2.9). A possible explanation is that strong ram-pressure "wind" can cause the spiral arms to unwind. This effect has not been observed in hydrodynamical simulations (yet) due to the difficulty of reproducing realistic spiral arms. Observationally the effect has not been reported either, although studies of jellyfish galaxies have mostly focused on stripping of galaxies in the plane of the sky, where the tails are more easily detected. The proposed effect, if true, would be better appreciated in galaxies like JO201, that are experiencing intense face-on stripping and are viewed along the direction of the stripping (i.e. along the line of sight). We plan to utilise simulations to address this idea in future studies.

Although the jellyfish tails in JO201 extend to $\sim$50 kpc from the disk, it is likely that they are much larger given the strong projection effects expected for this galaxy and the fact that the stripped material covers essentially the entire field of view of the MUSE mosaic.

Our measurements are consistent with recent observations of other jellyfish galaxies in clusters. For example, from deep Hα+[NII] wide-field imaging with MegaCam at the CFHT, Boselli et al. (2016) found tails of diffuse ionised gas in NGC 4590 extending $\sim$ 80 kpc from the disk in projection (at a surface brightness limit of a few 10^{-18} erg s^{-1} cm^{-2}). Using MUSE at the VLT, Fumagalli et al. (2014) observed the jellyfish galaxy ESO137-001 in the Norma cluster, and found that at a surface brightness $\sim 10^{-18}$ erg s^{-1} cm^{-2}, the tails extend to > 30 kpc from the disk.

These examples are quite different from JO201 and its environment: NGC 4590 is a very massive late-type galaxy falling into a low-mass cluster, ESO137-001 is a lower-mass spiral falling in a very high mass cluster, and JO201 is a massive spiral falling into a very massive cluster. Although the exact comparison of the tail extent is subject to projection effects and depth of the observations, we can confidently conclude that the observed tails in all cases clearly extend well beyond the galaxy (out to at least $30 - 80$ kpc), which implies that RPS has a wide range of action.

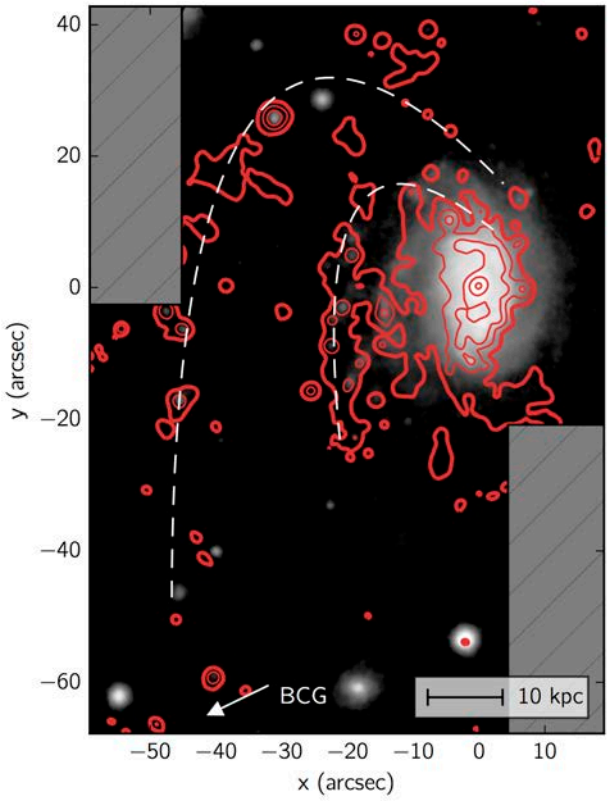

Figure 2.9: Contours of Hα (λ6562.82Å) overlaid on continuum fit around Hα line. Steeper contours on the western edge of the disk suggest increased star formation activity resulting from the interaction with the ICM. Contours correspond to surface brightness levels of 6.67×10^{-19}, 3.55×10^{-18}, 1.89×10^{-17}, 1.00×10^{-16}, 5.33×10^{-16} erg s^{-1}cm^{-2} from low to high. The pattern of the stripped material appears to follow the shape of the spiral arms (see dashed white curves as reference) as discussed in the text. The white arrow indicates the direction toward the BCG.

2.4.5 3D Rendering of Hα Emission

To visualise the distribution of the Hα gas, a 3D model was produced by combining projected space and velocity space.

The fitted Hα line was used to produce a "cleaned" cube comprised of only Hα emission, onto which surface contours were wrapped using the velocity distribution in place of the spatial distribution of the gas along the line of sight. We selected contour levels manually to optimally separate different points of interest, such as the bright central Hα emission, the knots within the tails and the diffuse extended gas. The resulting 3D model is presented in Figure 2.10. An interactive version of the figure is available online at `web.oapd.inaf.it/gasp/publications.html`.

Viewed face-on, the 3D model visualises the distribution of the Hα gas and highlights the bright knots within the tails (like Figure 2.9). If the cube is rotated to get a view through the y-axis, the rotation of the gas is visible both within the disk and in the tails, along with a dispersion-dominated nuclei. From this perspective (and also when viewing through the x axis), the diffuse component of the gas can be seen at higher line-of-sight velocities than the denser knots.

2.5 Kinematics

2.5.1 Absorption-Line Kinematics

In order to extract the stellar kinematics, we extracted the absorption line properties from the galactic extinction corrected cube using the Penalized Pixel-Fitting (pPXF) code (Cappellari & Emsellem, 2004), that fits the observed spectra with a set of templates. We spatially binned the spectra, using a Voronoi tessellation dependent on the signal to noise of our spectra (S/N=15), as described in Cappellari & Copin (2003). In particular, we used a Weighted Voronoi Tessellation (Diehl & Statler, 2006) in order to take care of possible significant gradient in the S/N. For our analysis we used the stellar population templates by Vazdekis et al. (2010), i.e. a set of SSP spanning a range in metallicity (6 different metallicities from $[M/H] = -1.71$ to $[M/H] = 0.22$) and age (26 ages from 1 to 17.78 Gyr) calculated with a Salpeter IMF (Salpeter, 1955) with a slope of 1.30 and the Padova 1994 isochrones (Bertelli et al., 1994; Girardi et al.,

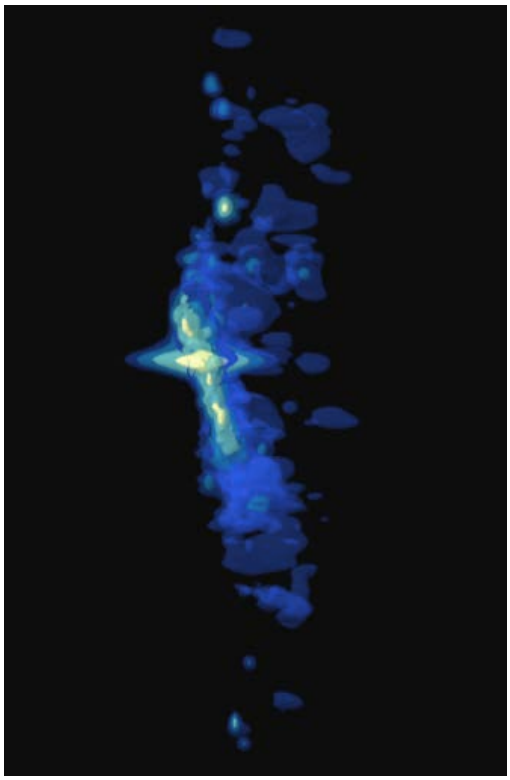

Figure 2.10: 3D visualisation of Hα gas extracted from KUBEVIZ fit produced using the method presented in Vogt et al. (2016b) and Vogt et al. (2016a). X and Y axes show projected distance, with the Z axis representing the wavelength/velocity and linewidth/sigma. Surface contours are plotted with different colours, from yellow to dark blue. The units and contours are arbitrary as they have been chosen at levels which highlight interesting features in the Hα gas, such as the bright central emission, knots of Hα and the extended diffuse gas. An interactive version of this figure is accessible online at `web.oapd.inaf.it/gasp/publications.html`.

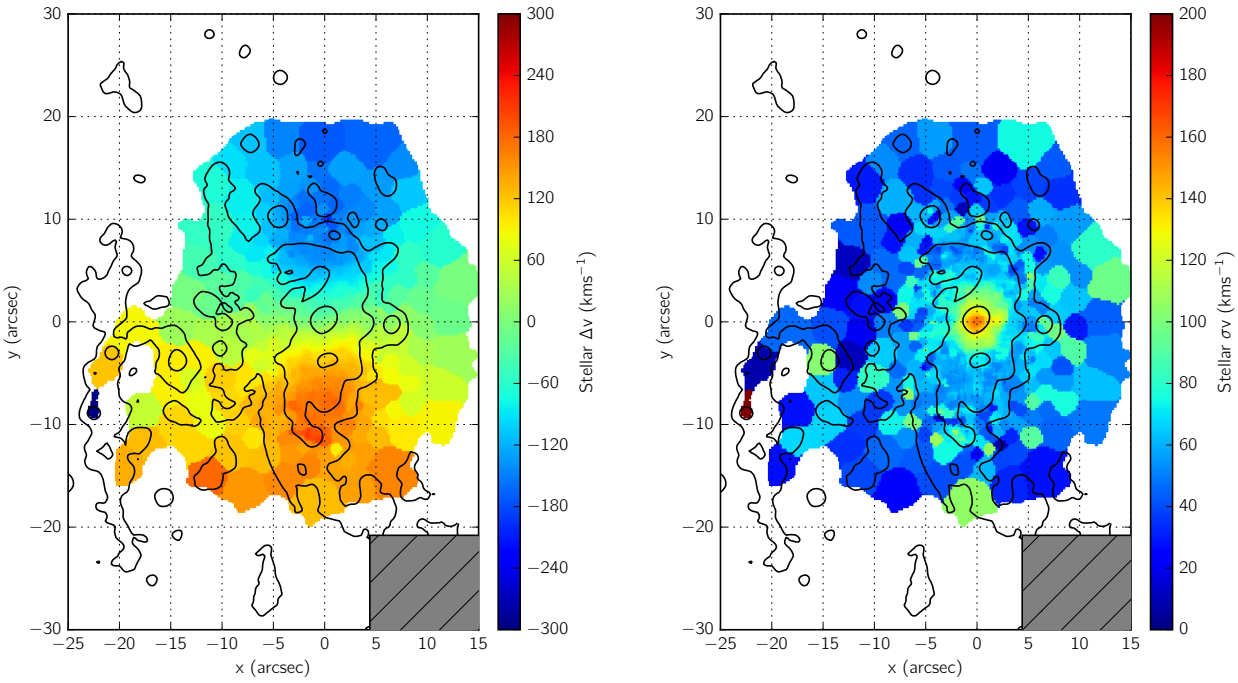

Figure 2.11: Stellar kinematics (*left:* line-of-sight velocity, *right:* velocity dispersion) derived from ppxf fits binned using a Voronoi Tessellation to obtain a S/N of 15. Hα contours are shown overlaid. As expected for the case of RPS, the stellar component shows smooth, generally unperturbed kinematics. This is consistent with a hydrodynamical interaction as opposed to a gravitational one.

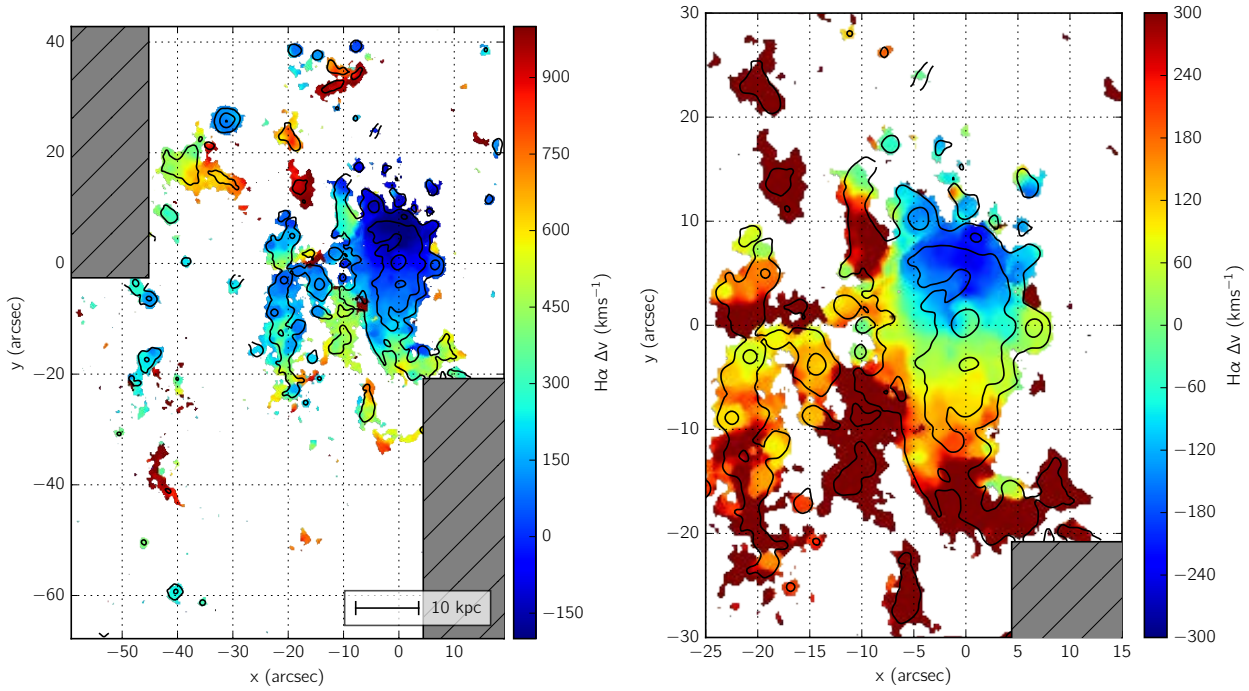

Figure 2.12: *Left:* Velocity map produced of Hα (λ6562.82Å) emission relative to the galaxy systemic velocity comprised of a combination of single component and two-component fits as described in section 2.4.2. The velocity map has been convolved with a median filter with a 3×3 pixel kernel for visualisation purposes, in addition to the data being smoothed using a mean filter with a 3×3 kernel before fitting. *Right:* Velocity map as on left, cropped to show the disk region with a rescaled colour map to better exhibit the Hα kinematics of the disk region. Black contours on both figures indicate the Hα flux for context.

1996). We excluded from the fit the red part of the spectra, where the theoretical stellar libraries have a poor resolution and the observed spectra are strongly contaminated by the sky lines. Spurious sources (foreground stars, background galaxies) have been masked before performing the fit. We derived the rotational velocity, the velocity dispersion and the two h3 and h4 moments. This allows us to derive for each Voronoi bin a redshift estimate, that will then be used as input for the stellar population analysis.

The stellar kinematics maps (not corrected for the inclination of the galaxy) are shown in Figure 2.11 with the velocity on the left panel and the velocity dispersion on the right. The velocity map shows that the stellar component follows a uniform rotation, with maximum velocity $\simeq 155$km s^{-1}. The velocity dispersion profile of this galaxy is also smooth, with increasing values towards the centre that peak at $\simeq 150$km s^{-1}.

To the south-east of the disk, two parallel tails are visible. It is unlikely that these tails arise from tidal interactions, since i) they are seen only in one side of the galaxy, ii) spectrophotometric modelling shows they have very young stellar populations (Bellhouse et al., 2019), and iii) they follow the main rotation of the galaxy. As will be discussed in (Bellhouse et al., 2019), these young stellar tails most likely formed in-situ from stripped gas.

Overall, the stellar kinematics of JO201 show little deviation from the smooth rotation curve that would be expected of a gravitationally undisturbed galaxy.

2.5.2 Emission-Line Kinematics

In order to produce maps of the kinematics of the gaseous component in JO201, we extracted the velocity and velocity dispersion of the Hα (λ6562.82Å) line from the line fits presented in Section 2.4.

The left panel of Figure 2.12 shows a map of the line-of-sight velocities of the Hα emission (not corrected for inclination). A zoomed version focusing only on the disk (with a smaller range of velocities) is shown on the right panel of the figure. Overall, the gas component displays a clear rotation within the disk. The rotational velocity gradient of the galaxy is somewhat retained in the stripped material to at least 50kpc in projected distance from the disk, although beyond the central disk, the stripped material outside the galaxy's main body is notably residing at higher line-of-sight velocities (up to $\sim$900km s^{-1}) with respect to the disk. This highly redshifted emission reflects the intense RPS acting on the galaxy along the line of sight. As the galaxy plunges towards the observer, the gas stripped from the (less shielded) outskirts of the galaxy is

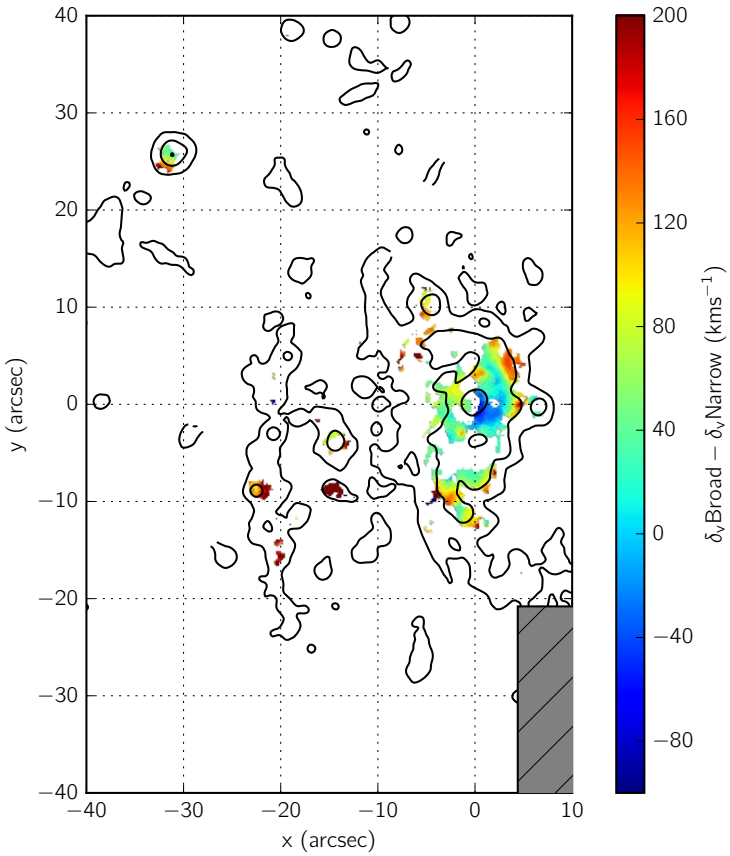

Figure 2.13: Velocity offset between broad and narrow components of Hα (λ6562.82Å) line where double component fit is available. The region of blueward broad component indicating a tail orientated towards the observer is likely to originate from an outflow associated with the central AGN. The redward broad component in the outskirts of the disk evidence a tail in the velocity distribution produced by increased stripping intensity at the outer edges of the disk. Black contours indicate the Hα flux for context.

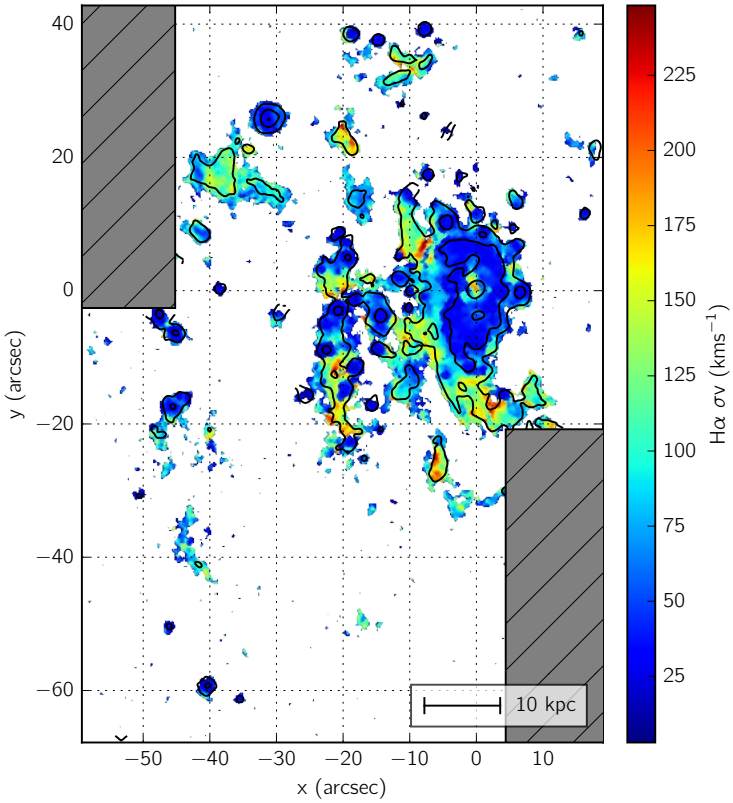

Figure 2.14: Velocity dispersion map produced using Hα (λ6562.82Å) emission from combined single component and two-component fits as described in section 2.4.2, corrected for instrument resolution by KUBEVIZ. The velocity dispersion map has been convolved with a median filter with a 3×3 pixel kernel for visualisation purposes.

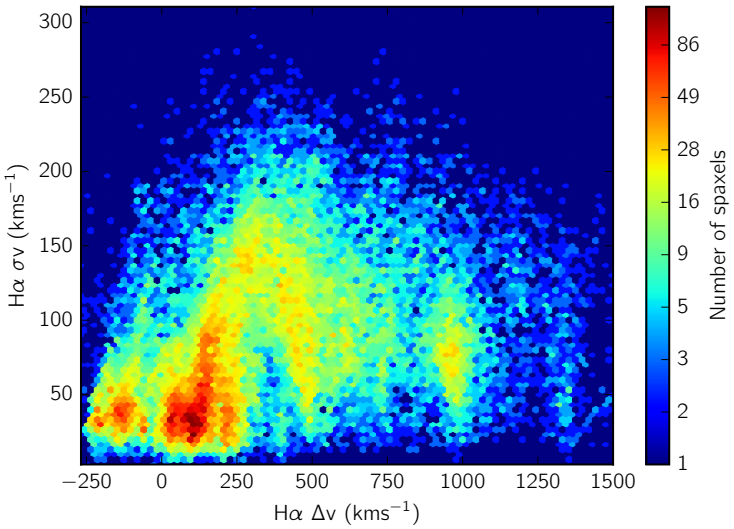

Figure 2.15: Distribution of spaxels arranged by velocity on x axis and sigma on y axis. The plot shows a bimodal distribution around 0km s^{-1} from the rotation curve of the galaxy, followed by an increase in dispersion with velocity due to the onset of turbulent motions within the stripped gas. This trend reverses above 350km s^{-1} as the dispersion falls back down, likely to be caused by the recollapse of cooling stripped gas causing the dispersion to decrease.

dragged away from the galaxy. As already mentioned, this interpretation is in agreement with the extreme line-of-sight velocity of JO201 with respect to the cluster (Section 2.2), which suggests that the velocity vector of the galaxy is mostly in the line of sight and thus the majority of the stripped material must reside behind the galaxy.

Inside the disk, the maximum observed rotational velocity of the ionised gas toward the observer is ∼144km s^{-1}, extending beyond ∼179km s^{-1} away from the observer at the southern end of the disk, up to where gas starts to be visibly stripped, both along the plane of the sky and in the redshift direction. From a quick comparison of the rotation of the gas (Figure 2.12, right) and the stars (Figure 2.11, left), it is noticeable that the rotational velocity of the gas is significantly higher than that of the stars. A careful comparison of the stellar and gas rotation curves is presented in Section 2.5.3.

We further compare the kinematics of the broad and narrow components of the Hα line in Figure 2.13 for those regions where a double-component fit was available. The colours in the figure highlight the difference between the velocities of the 2 components. The central region showing a blueward broad component indicates

a tail orientated towards the observer. This is likely to originate from an outflow associated with the central AGN. The redward broad component in the outskirts of the disk is suggestive of tails produced by increased stripping intensity at the outer edges of the disk, consistent with outside-inward stripping.

The line-of-sight velocity dispersion of the gas component is shown in Figure 2.14. The figure shows that the velocity dispersion in the central region of the disk is $150 - 180$km s^{-1}. The lowest velocity dispersions are observed in the dense knots with large Hα fluxes, with typical values ranging around $20 - 40$km s^{-1}. The stripped diffuse gas bridging between star-forming knots appears to have a higher velocity dispersion, with values around 140km s^{-1}.

Finally, a histogram is shown in Figure 2.15 of the line-of-sight velocities and velocity dispersions of each fitted spaxel. On the x axis, the distribution of velocities gives a rough separation between the disk of the galaxy and its stripped, higher velocity tails. The y axis can be used to distinguish between collapsing and heated/shocked gas, with kinematically hotter clouds appearing higher up on the axis. The two red clumps to the lower left ($\Delta v \lesssim 200$km s^{-1} and $\sigma v \lesssim 70$km s^{-1}) reveal a bimodal distribution of line-of-sight velocities indicating the rotation curve of the disk of the galaxy. The right-hand, higher velocity clump of the two is much larger, indicating a skew to higher velocities due to the influence of strong line-of-sight gas stripping. At velocities of $\lesssim 350$ km s^{-1}, the stripped gas follows a steep increase in velocity dispersion with increasing velocity, owing to the onset of turbulent motion within the stripped gas as it moves away from the galaxy. Above 350km s^{-1} the trend reverses as the dispersion falls, likely due to the cooling of stripped gas recollapsing.

Although the unique direction of stripping and viewing angle of JO201 makes the comparison with other jellyfish galaxies difficult, our results are consistent with observations of nearby jellyfish that show a structured distribution of the stripped gas composed of compact blobs and diffuse filaments (e.g. Boselli et al., 2016), as well as simulated RPS events (Tonnesen & Bryan, 2010). Moreover, previous studies of the dynamics of jellyfish galaxies have shown that the stripped gas (primarily in the plane of the sky) preserves the rotation of the galaxy for a while (e.g. up to $\sim$ 20kpc in ESO137-001; Fumagalli et al., 2014), and then turbulent motion takes over. In JO201 we observe a similar phenomenon, but primarily along the line of sight.

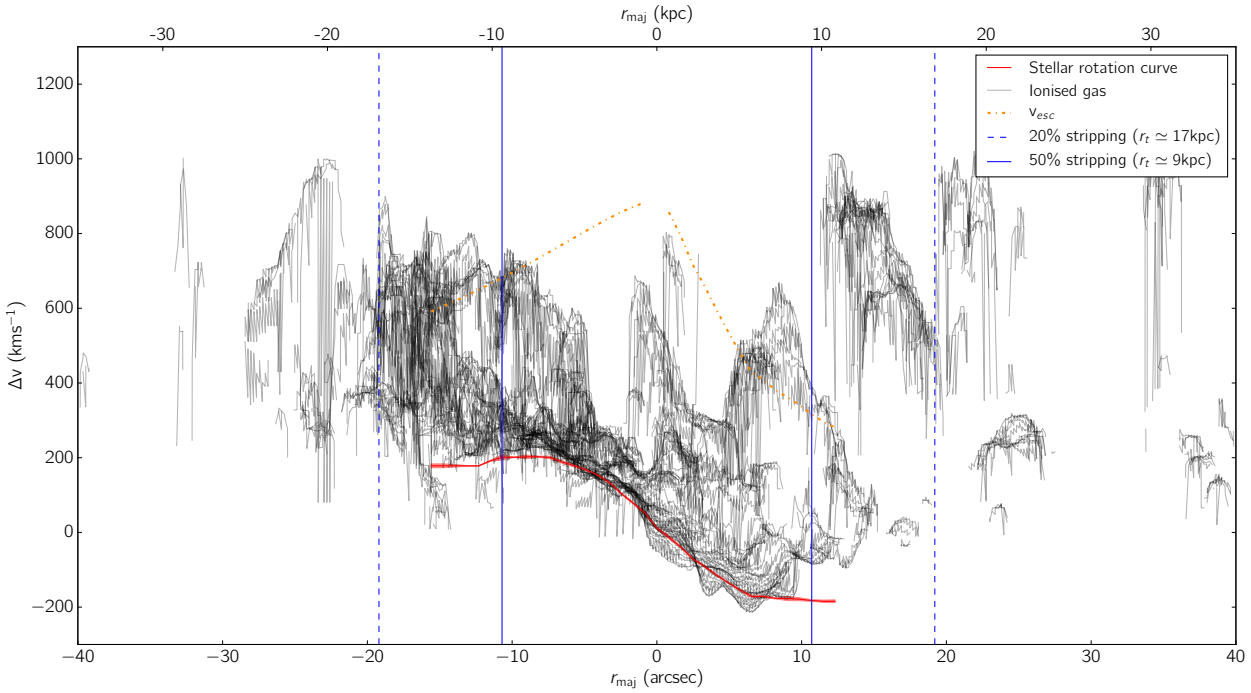

Figure 2.16: The rotation curve along the kinematic major axis r_{maj} for the stellar component of JO201 is plotted in red. The solid black lines show the velocity of the ionised gas along strips parallel to the direction of r_{maj}. The orange dot-dashed line shows the escape velocity calculated as described in the text. The vertical blue dashed and solid lines further show the truncation radii at which 20% and 50% of the total gas mass is expected to have been stripped respectively, as described in Section 2.2 (see lines in Figure 2.2). The gas stripping is made clear by the increased line-of-sight velocity of the ionised gas to the left and right of the disk caused by regions of stripped gas being slowed by the ICM with respect to the infalling galaxy. Rotating clumps of gas can also be seen at higher Δv in the stripped gas, rotating around their own centres, away from the motion of the galaxy. It is likely that much of this gas has become unbound from the galaxy due to its high velocity offset, particularly where it approaches and passes the indicated escape velocity, however the gas retains the angular momentum of its previous rotation within the galaxy. The region of gas which remains mostly bound to the disk is best illustrated by the dashed lines in Figure 2.17, within a diameter of $\sim$ 10kpc (see text for details). Measured velocities have been corrected for inclination to show the intrinsic rotational velocity.

2.5.3 Rotation Curves

To directly compare the distribution of the stellar component and the Hα gas in velocity space across the galaxy, we construct rotation curves.

The red curve in Figure 2.16 shows the rotation curve of the stellar component, constructed by taking the median velocities in a strip approximately 10 arcseconds wide along the disk's kinematic major axis (2.5 deg from north to east). The Hα emission-line velocity map is plotted on top, in strips parallel to the direction of the stellar kinematic major axis, to show the overall velocity structure of the gas (black lines), as well as the spread within individual regions undergoing stripping. Velocities were corrected for galaxy inclination ($i = 54$ deg from face-on) by dividing the observed velocities by $\sin i$.

The offset between the stellar and gaseous components of the disk, first seen in Section 2.5, is clearly visible in Figure 2.16. A large fraction of the ionised gas is redshifted with respect to the stellar disk as a consequence of strong ram-pressure drag. Interestingly, many of the individually stripped clumps of material (groups of black lines separated from the main body of the galaxy) seem to preserve the overall gradient of the rotation curve of the galaxy, although redshifted.

To test whether the high-velocity stripped gas is bound to the galaxy, we computed an upper limit to the escape velocity, v_{esc}, using the potential of a thin exponential disk, with the form presented in equation 2.165 of Binney & Tremaine (2008):

$$\Phi(r, 0) = -\pi G \Sigma_0 r \left[I_0(y) K_1(y) - I_1(y) K_0(y) \right] \tag{2.6}$$

where $y = r/2r_d$, I_n, K_n are modified Bessel functions, r_d the disk scale length, and Σ_0 the central surface density of a thin exponential disk, calculated from the dynamical mass as $\Sigma_0 = M_{dyn}/2\pi r_d^2$. To determine M_{dyn} we followed equation 15 of van den Bosch (2002), using the maximum velocity values of the stellar rotation curve ($\sim$190km s^{-1} after correcting for an inclination of 54°, calculated from an axis ratio of $\sim$0.6) and an I-band disk scale "length (we used 5.56kpc as in Section 2.2, as this value is consistent with fits made to the stellar continuum using the MUSE datacube). The resulting dynamical mass was found to be $M_{dyn} = 5.10 \times 10^{11} M_\odot$. The calculated escape velocity ($v_{esc}^2(r) = -2\Phi(r)$) is an upper limit, as it does not take into account the vertical extent of the disk. Moreover, we note that $v_{esc}(r)$ should ideally be compared

with the magnitude of the full velocity vector of the gas, while our observations are limited to the line-of-sight velocity component. We plot $v_{esc}(r)$ as a dashed blue curve on top of the stellar rotation curve of the galaxy in Figure 2.16. Because it only makes sense to compare absolute values of Δv with v_{esc}, for $r_{maj} > 0$ (where the stellar rotation curve has $\Delta v < 0$) we have plotted $v_{esc} + 2\Delta v$ instead[4]. The plotted line helps distinguished several clumps of stripped gas that are unbound from the disk. These are located in the outer parts of the disk lying above the line.

Figure 2.17 presents inclination-corrected rotation curves of the stars and the ionised gas, separated into narrow and broad components of the Hα emission. All of the curves were constructed by taking the median velocities in a strip approximately 10 arcseconds wide along the disk's kinematic major axis. In the lower part of the figure, the residuals of the narrow and broad gaseous components from the stellar component are shown.

The rotation curves highlight the existing offset between the stellar and gaseous components of the disk. In particular, the rotation curve of the gaseous component shows an upward turn at the edges of the stellar disk, $|r_{maj}| \gtrsim 6$ arcsec. The residuals show clearly the increase in the velocity offset with distance from the centre of the disk, with the broad component showing a more pronounced effect. Note that the difference between the blue and green lines in Figure 2.17 reflects the velocity offset displayed in Figure 2.13. The observed behaviour can be interpreted as a decrease in the gravitational binding of the gas at higher distances from the centre of the galaxy (see Section 2.2), that allows the gas to be more easily stripped from the edges of the disk.

In summary, Figures 2.16 and 2.17 highlight the intensity of the stripping experienced by JO201, with a redshifted ionised gas component with respect to the stellar disk. This is consistent with ram-pressure dragging the gas away from the fast-moving galaxy (and the observer). The incremental shift in velocity observed at larger distances from the centre of the galaxy indicates outside-in gas removal, and the shape of the asymmetric rotation curve of the gas is consistent with simulations of face-on RPS (Kronberger et al., 2008).

[4]This accounts for the difference in using Δv rather than $|\Delta v|$. The plotted function, p(r) should obey the relation $v_{esc} - |\Delta v| = p(r) - \Delta v$.

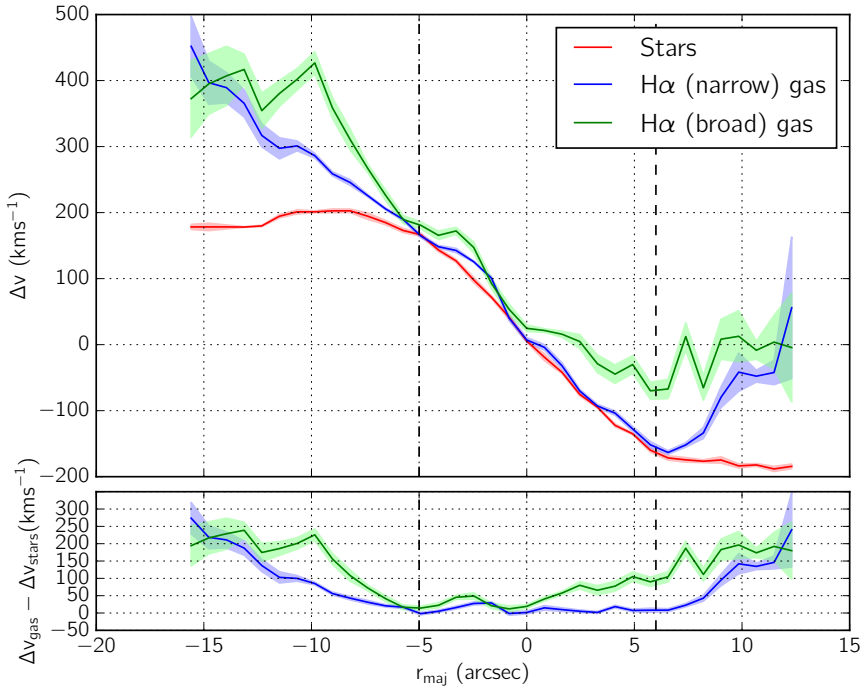

Figure 2.17: Rotation curves of JO201, measured within a ∼10 arcsecond-wide strip along the kinematic major axis r_{maj} of the stellar disk. Inclination-corrected median stellar velocities (obtained from the absorption line kinematics) are shown in red, along with the median velocity of the ionised gas, separated into narrow (blue), and broad component (green) of the Hα emission-line fits. Standard deviations of bootstrap medians are shown for both. Dashed lines enclose the region of the disk less affected by ram-pressure stripping ($r_{maj} \lesssim 6$kpc).

2.6 Summary and Conclusions

This study is the second of a series presenting the first results from the ongoing GASP (GAs Stripping phenomena in galaxies with MUSE) survey at the VLT (Poggianti et al., 2017b: Paper I), that is obtaining deep integral-field spectrocopy for over 100 galaxies with signatures of gas stripping (so-called "jellyfish" galaxies). We focus on the distribution and kinematics of the stellar and ionised gas components of JO201, one of the most striking jellyfish galaxy in the GASP survey and its parent sample (Poggianti et al., 2016).

We start by studying the global environment of JO201 and find that it is part of a massive unrelaxed galaxy cluster (A85). Its large differential line-of-sight velocity with respect to the cluster, and (projected) proximity to the BCG, indicate JO201 is likely falling into the cluster for the first time, following a radial orbit mostly in the direction towards the observer. Moreover, a dynamical analysis utilizing all the cluster members suggests that JO201 is possibly falling into A85 within a small group of galaxies.

JO201 has been classified as a jellyfish galaxy candidate by Poggianti et al. (2016) owing to the presence of optical tails in only one side of the galaxy, which suggests that unilateral gas stripping is taking place. We modelled the ram-pressure expected in A85 and find that, at the projected position and velocity of JO201, a galaxy of its mass and size must have lost $\sim 50\%$ of its total gas mass during its first passage though the cluster. The amount of lost gas coincides remarkably well with the estimated gass loss computed by comparing the size of the stellar disk with the extent of the remaining Hα (ionised gas) disk. Our environmental analysis thus strongly support RPS as the principal mechanism removing gas from JO201 during its first passage though the dense ICM.

We analysed the MUSE datacubes (covering JO201's main body and outskirts) to study the distribution and kinematics of the stellar and ionised gas components of the galaxy, and find the following.

1. There is significant Hα emission concentrated along the windward side of the galaxy (colliding with the ICM), as well as tails in the opposite direction, composed of bright Hα knots and diffuse emission. The tails extend $\sim$50kpc away from the galaxy, and point towards the cluster centre. The observed (structured) distribution of the gas is consistent with RPS simulations of galaxies (Tonnesen & Bryan, 2010). We identify a pattern in the distribution of stripped gas in the tails of JO201 that resembles the shape of wide spiral arms. If true, a possible explanation is that strong RPS can cause an unwinding of

the outer spiral arms. Owing to the difficulty in reproducing realistic spiral arms in simulated galaxies, this effect has not (yet) been reported by simulations of RPS. Observations of other jellyfish galaxies have not reported the effect either, but this is likely a consequence of the rare angle of observation of the JO201. We hope to explore and expand upon this idea in future GASP studies.

2. In some parts of the galaxy the Hα emission often displays a non-gaussian profile. We characterise the different types of line profiles within the galaxy and find that at the centre of the galaxy there is emission-line broadening caused by an active nucleus. In the outer parts of the disk and stripped tails, the emission lines can be described by either a single narrow gaussian, or a narrow component with an offset (redward) broader component. These double-gaussian profiles result from intense gas stripping along the line of sight, that drags material away from the galaxy (in the opposite direction to the observer).

3. After selecting the best fit (single vs. double-component gaussians) in each spaxel, we constructed a three-dimensional model of the Hα emission in the galaxy that highlights the extent of the emission line wings in the redshift direction.

4. From a kinematic analysis of the absorption features, we find that the velocity field of the stellar component is well reproduced by a smoothly rotating disk. This suggests that there are no gravitational perturbations such as tidal interactions acting on JO201. The velocity of the gaseous component follows that of the stars in the inner regions of the galaxy, but deviates significantly from the disk to the tails. In particular, much of the stripped material with Hα emission resides at higher line-of-sight velocity with respect to the stellar disk. The trend, clearly seen in the rotation curves of the stellar and gaseous components, increases with distance from the galaxy centre, in agreement with simulations of face-on RPS (Kronberger et al., 2008).

5. The velocity dispersion in the stripped diffuse gas is high (> 100 km s^{-1}), while the star-forming blobs are kinematically cold (velocity dispersion < 40 km s^{-1}), suggestive of shock heating and gas compression respectively.

Overall, our results favour RPS as the main mechanism removing gas from JO201. This galaxy's trajectory

in the cluster, together with our viewing angle, offer a unique insight into the ram-pressure drag generated by the ICM, with most of the stripping happening along our line of sight as the galaxy plunges through the cluster towards the observer. Moreover, the MUSE observations reveal clear evidence for outside-inward RPS of the disk, with gas compression and shock heating occurring in the stripped tails.

In chapter 3 we further investigate the sources of ionisation in this galaxy, along with an analysis of the gas mass loss, gas-phase metallicity, and ages of the stellar populations across this galaxy.

JO201 is a an extreme case of stripping of a massive galaxy ($\sim 10^{11} M_{\odot}$) in a massive ($\sim 10^{15} M_{\odot}$) cluster. Our results are consistent with previous studies of jellyfish galaxies in a variety of environments, and thus highlight the importance and wide range of action that RPS has on satellite galaxies.

Chapter 3

Physical Properties of a Galaxy Undergoing Ram-Pressure Stripping

This Chapter is comprised of the paper "GASP. XV. A MUSE view of extreme ram-pressure stripping along the line of sight: physical properties of the jellyfish galaxy JO201" (Bellhouse et al., 2019), published May 2019. The introduction has been abridged to avoid repeating Chapter 1, as per Chapter 2, whilst some sections have been expanded within the paper.

The majority of the paper is of the author's original writing, with contributions given to the text by Yara Jaffé in part of subsection 3.8.1, Jacopo Fritz in part of subsection 3.8.2 and Rory Smith in part of subsection 3.8.3

3.1 Introduction

In Chapter 2 (Bellhouse et al., 2017: GASP II), we presented a study of the environment of JO201 and the kinematic properties of its Hα emitting gas. We found that JO201 is moving at supersonic speeds (mach ~ 3.2) through the core of the massive cluster Abell 85 (A85) mostly along the line of sight, unlike the other jellyfish galaxies studied to date (Gullieuszik et al., 2017; Poggianti et al., 2017b; Fumagalli et al., 2014).

The GASP MUSE data as well as follow-up multi-wavelength observations revealed a largely undisturbed stellar disk accompanied by a disturbed, asymmetric and extended gas component with in-situ star-formation, suggestive of ongoing intense outside-in ram-pressure stripping along the line-of-sight (see Section 3.2.1 for details).

In this chapter, an in-depth analysis of the physical properties of JO201 is presented, including gas ionisation from emission-line ratio diagnostics, metallicity, star-formation rates, and ages of the stellar populations across the galaxy and its stripped tails. At the end, we compare all the derived quantities for this peculiar galaxy with a simple model of its evolution within the cluster to construct a comprehensive view of its stripping history.

The chapter is structured as follows. Section 3.2 summarises the properties of JO201 and the MUSE data from the GASP survey used in this study. The methods of galactic extinction correction and stellar absorption correction are outlined. In section 3.3, we describe the steps to analyse the datacubes and fit emission lines from the spectra. In section 3.4 we calculate the gas properties from the emission line parameters, including the production of line-ratio diagrams to determine ionisation sources as well as to calculate estimates of the metallicity and ionisation parameter. Section 3.5 focuses on the knots visible in the disk and tails. The process of detecting knots is explained and the properties of the knots are calculated from emission line fits derived from the integrated spectra.

Section 3.6 covers the star-formation rates across the galaxy, measured using the Hα emission.

In section 3.7, we explore the stellar population, derived from SINOPSIS photometric code fits (Fritz et al., 2017), comparing the star-formation rate surface density across the history of JO201's interaction with the cluster environment. We also look at the luminosity weighted age and explore how regions of the galaxy have been affected by these periods of star formation.

In Section 3.8 we use parameters of the galaxy and its host cluster to explore the stripping history of JO201, estimating the time since the galaxy began experiencing RPS, the star-formation histories of the stars within the tails, and the physical length of the the tails. Finally in section 3.9 we summarise the findings and draw conclusions, piecing together the journey of JO201 as it bullets through A85.

Throughout this study we adopt a Chabrier initial mass function (IMF; Chabrier, 2003), and a concordance ΛCDM cosmology of $\Omega_{\rm M} = 0.3$, $\Omega_{\Lambda} = 0.7$, $\rm H_0 = 70 km\,s^{-1} Mpc^{-1}$.

3.2 Data

This study exploits the MUSE observations presented in GASP II (Sec. 3.1).

In this section we summarise the main findings of previous studies of JO201 (Sec. 3.2.1), and the GASP MUSE observations, data reduction and analysis utilised (Sec. 3.2.2), highlighting any differences between the present study and GASP II.

3.2.1 The jellyfish galaxy JO201

JO201 is a massive spiral galaxy located in the massive galaxy cluster A85 ($M_{200} = 1.58 \times 10^{15}$, velocity dispersion $\sigma_{\rm cl} = 982$km s^{-1}) at a redshift $z_{cl} = 0.05586$. The galaxy has a stellar mass of $3.55 \times 10^{10} M_{\odot}$ and a dynamical mass of $5.10 \times 10^{11} M_{\odot}$ (GASP II).

As also shown in GASP II, JO201 lies at a projected distance of 360 kpc from the cluster centre, and has a line-of-sight velocity of 3363.7km s^{-1} (or $3.4 \times \sigma_{\rm cl}$) with respect to the mean velocity of the cluster. The proximity to the cluster centre, coupled with its extreme velocity place the galaxy close to the peak of stripping (see Jaffé et al., 2018). Moreover, the inclination of the galaxy and the morphology of its tails indicate that the interaction with the ICM is close to face-on. The MUSE data further reveals projected tails of Hα emitting gas up to at least ~ 50 kpc in length (see Figure 3.1), structured into kinematically cold knots (velocity dispersion < 40 km s^{-1}) and warm diffuse emission (> 100 km s^{-1}). These tails rotate with the stellar disk out to ~ 6 kpc, but become increasingly redshifted in the disk outskirts (by up to 900 km s^{-1}) with respect to the centre of the galaxy due to the intense ram-pressure along the line of sight, that causes the gas to drag behind the galaxy.

It is likely that JO201 is falling into the cluster within a small group of galaxies (GASP II) and that its visible nuclear activity (shown in Section 3.4) is being triggered by the interaction with the ICM (Poggianti et al., 2017a).

Follow-up studies of JO201 at different wavelengths have further revealed the presence of extra-planar molecular CO gas (Moretti et al., 2018a) and in-situ star formation activity visible in the Ultra Violet (UV; George et al., 2018). Moreover, Venkatapathy et al. (2017), detected emission in the tails of JO201 (A85[DFL98]176) at blue and UV wavelengths, but not in near infrared, which suggests a lack of an older

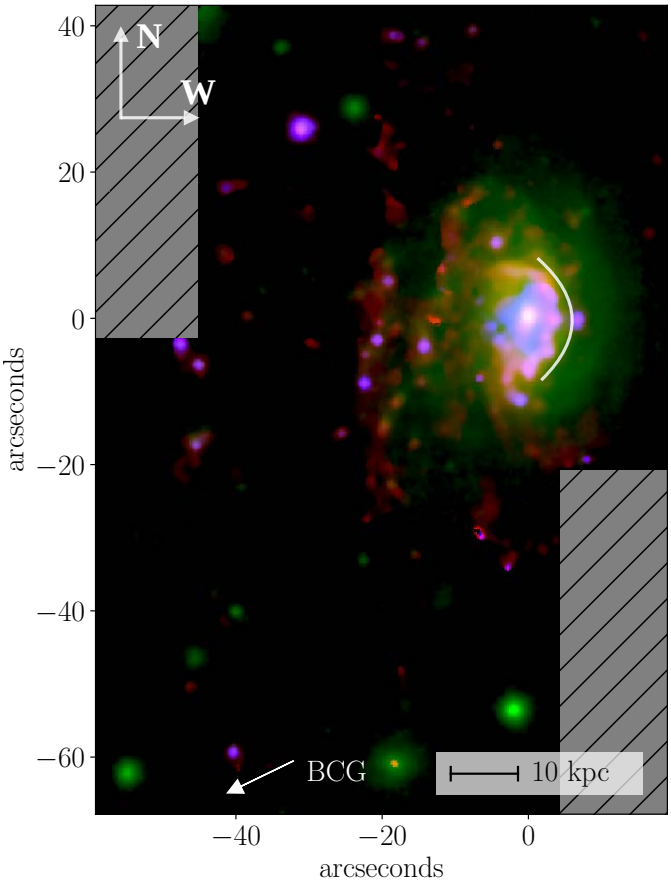

Figure 3.1: Composite image of JO201, red: Hα, green: stellar continuum fitted between 80-200Å either side of the Hα line, blue: [OIII]. The emission lines have been masked to a S/N ratio of 3 or greater and cleaned using a 5×5 median filter. The white curve indicates the leading edge of the galaxy, where the gas is compressed by RPS. The large offset of the red Hα from the green stellar component is clearly visible, as well as the large concentration of [OIII] in the central 2-3kpc of the disk. The bright [OIII] emission in the central region of the disk corresponds with a drop in the SFR according to both the Hα luminosity shown in the figure and the stellar age shown later. This may be due to feedback from the AGN inhibiting star formation in the central region of the disk

stellar component, as expected for hydrodynamic disruption.

Fig 3.1 shows an overview of JO201 with the stellar continuum (fitted between 80 and 200Å from the Hα) in green, Hα in red and [OIII] in blue, illustrating the intense stripping by the large offset of the Hα component from the stellar component, and the intense [OIII] emission from the central AGN.

3.2.2 MUSE datacube

JO201 was observed by MUSE as part of the GASP programme on December 17, 2015 with photometric conditions. A total of eight exposures of 675s each were taken across two adjacent fields to produce the final mosaic. The data were reduced using ESOREX recipes version 3.12, MUSE pipeline version 1.2.1 (see GASP I for details on the reduction process). The sky background was measured from the sky coverage within the individual frames for subtraction and the final wavelength and flux calibrated images were combined using sources in the white light images for alignment. The final image quality of the reduced cube is 0."8 FWHM.

3.2.3 Dust extinction

To prepare the cube for emission line fitting, the effect of dust extinction was accounted for accordingly with other GASP studies. Dust extinction by the Milky Way was corrected across the cube, the full details of the correction are outlined in Chapter 2.

In addition to galactic extinction by the Milky Way, we corrected internal extinction within JO201 using the Cardelli extinction law (Cardelli et al., 1989) using the Balmer decrement within each spaxel to calculate the attenuation A_λ for each emission line, assuming an intrinsic ratio of Hα/Hβ of 2.86. The correction uses the Balmer decrement to obtain the distribution of dust across JO201 by the relative extinction of $H\beta$ with respect to $H\alpha$. The theoretical ratio of these two lines can be assumed to be 2.86 in regions dominated by photoionisation, assuming case B recombination in the low density limit at a temperature of $T \sim 10^4 K$ (Osterbrock & Ferland, 2006). The observed value is increased by the presence of dust which preferentially absorbs the shorter-wavelength emission. This shift in the Balmer decrement can therefore be used to determine the distribution of the dust and the correction to be applied to correct the emission.

The resulting correction was applied only to regions in which all corrected lines are observed to S/N > 3 and, since the correction only applies to regions which are dominated by photoionisation, spaxels which lie

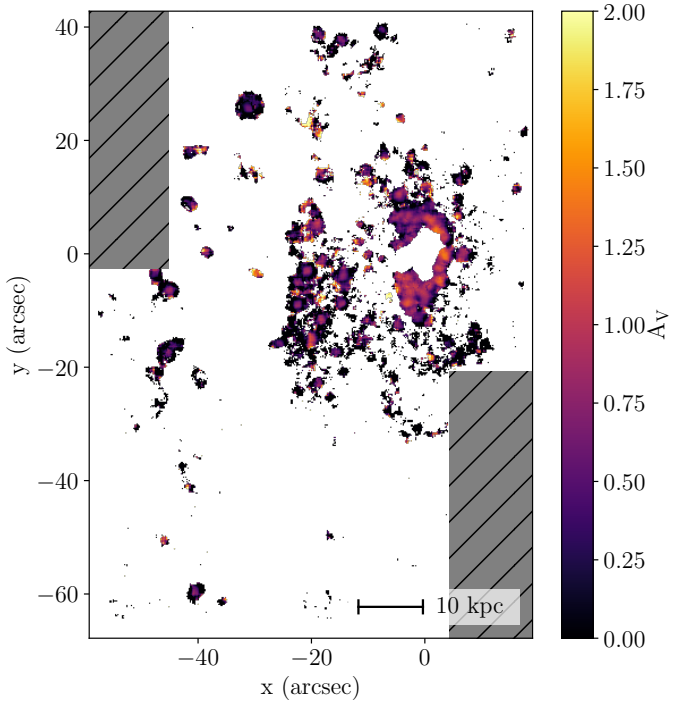

Figure 3.2: V-band attenuation (A_V, in magnitudes) derived from the Balmer decrement and used to calculate the corrections required for internal dust extinction. The AGN-dominated emission in the centre and the non-photoionisation regions are omitted as described in the text. The values reveal that much of the dust extinction occurs in the disk and in the centres of the knots.

above the Kewley et al. (2001a) line on the [OIII]/Hβ vs [NII]/Hα (Baldwin, Phillips & Terlevich, 1981: BPT) diagram were also omitted.

The map of the V-band attenuation calculated from the Balmer decrement is shown in Figure 3.2 in terms of A_V. as calculated in equation 3.1. It is clear from the figure that much of the attenuation by dust occurs within the regions of the disk and it is slightly less prominent in the trailing knots. This pattern is similarly observed in other GASP galaxies undergoing stripping along the plane of the sky.

$$A_V = \frac{\log(2.86) - \log\left(\frac{F_{H\alpha}}{F_{H\beta}}\right)}{0.4\left(\frac{A_{H\alpha}}{A_V} - \frac{A_{H\beta}}{A_V}\right)} \tag{3.1}$$

3.2.4 Emission-Only Datacube

The emission line fluxes are subject to stellar absorption and direct measures will underestimate the true flux, unless the absorption line contribution can be accurately estimated. To obtain emission line fluxes corrected for stellar absorption, we ran the spectrophotometric code SINOPSIS (Fritz et al., 2017), which includes the pertinent nebular emission lines. SINOPSIS was used to find the best fitting combination of single stellar population (SSP) models to the spectra.

The best-fitting solution found by SINOPSIS was then subtracted from the original cube to produce an emission-line-only cube which was used in the subsequent analysis. A few examples of the continuum subtracted spectra from this cube are shown in the bottom panel of figure 3.3.

3.3 Emission-Line Fits

As in GASP II, we used the IDL custom code KUBEVIZ (Fossati et al., 2016) written by M. Fossati and D. Wilman to fit the emission lines, adding some changes to optimise for the line ratio analysis. KUBEVIZ fits selected emission lines to the spectrum of each spaxel with models comprised of one or two Gaussian profiles, or by defining lines using moments. The full details of the fitting process are described in GASP II. In summary, we spatially smoothed the emission-only datacube (c.f. Sec. 3.2.4) using the mean value within a 3×3 kernel. As in the previous chapter, the kernel size was chosen to smooth the data sufficiently to produce successful fits in KUBEVIZ to S/N > 3, whilst minimising the loss in spatial resolution. The zero-point redshift was set to $z = 0.045$, the mean redshift for JO201, and the option in KUBEVIZ was enabled which scales the noisecube errors to give a reduced $\chi^2 = 1$. Examples of the fits given by kubeviz to different spectra can be seen in Figure 2.6, in Chapter 2.

It is important to mention that the large line-of-sight component of the stripping in JO201 causes the emission-lines in some regions of the disk to be non-Gaussian (see "Disk" spectrum in Figure 3.3, and also GASP II Figure 5), often requiring two-component fits. Typically, in these regions the emission is described by a sharp narrow line accompanied by a fainter component with a higher velocity dispersion and a slightly redshifted line-of-sight velocity.

As shown in GASP II, most of the spaxels requiring double-component fits are located around the edges of

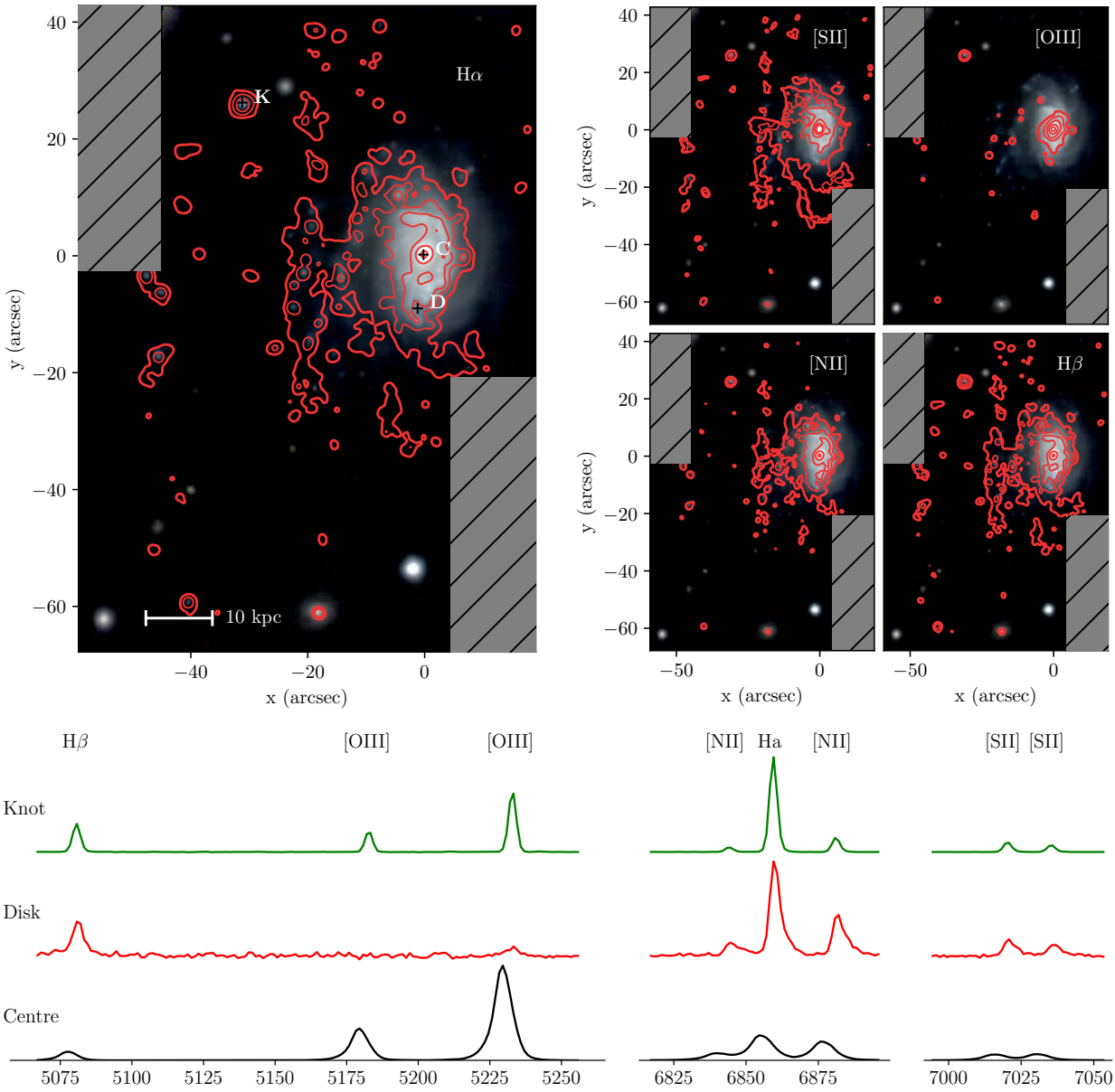

Figure 3.3: *Top:* Emission-line maps of Hα, [SII], [OIII], [NII] and Hβ from the dust-corrected emission-only cube are shown in red contours, on top of an RGB image of JO201 produced using 1000Å slices integrated from the datacube (B:5000-6000Å, G:6000-7000Å, R:7000-8000Å). Each line has been masked to a S/N of 3 or greater. *Bottom:* Examples of spectra, with stellar component subtracted as described in the text. The spectra correspond to 3 regions of interest indicated on the Hα linemap in the left panel: Galaxy centre (C), disk (D), and a knot (K). The central region exhibits much broader lines around the AGN, with a larger proportion of [OIII] emission. Within the disk, the lines are much narrower and slight asymmetry is visible due to the stripping acting in the line of sight. The knot exhibits narrow emission with strong Hα and [OIII] emission.

the disk, where ram-pressure has already removed and spread a significant amount of gas. The broad emission seen in the centre of the galaxy on the other hand originates from the active galactic nucleus (AGN).

Both single and double-component fits were carried out to the emission lines present in the MUSE spectra.The fits used in the subsequent analysis were therefore a combination of single and double component fits, decided on a spaxel-by-spaxel basis depending on the line profiles. In any given spaxel, the double-component fits were preferred if the two components were detected to S/N $>$ 3 and they are sufficiently separated in velocity (i.e. detectable emission-line wings, or multiple peaks in the same line of sight). Otherwise, the single-component fits with S/N $>$ 3 were used. The selection process between 1 and 2 component fits is described in further detail in GASP II. It is worth noting that in the regions where the emission is faint, the single-component fits tend to yield a higher signal-noise ratio.

For the rest of the analysis, the two components of the emission-line fits will be referred to as "primary" and "secondary". The primary component refers to either the single component fit or the narrower component (velocity dispersion: 3.0 - 310.7km s^{-1}, mean value: 84.4km s^{-1}) of the double component fit. These together describe the majority of the emission from the galaxy disk, knots and tails. The secondary component instead, refers to the more diffuse component (velocity dispersion: 21.4 - 376.8km s^{-1}, mean value: 123.4km s^{-1}) of the two component fit and generally describes redshifted tails caused by line-of-sight stripping, co-spatial knots, or emission around the AGN region. It should be noted that the fit parameters are convolved with the instrumental resolution ($\sim$100km s^{-1}) to give the model spectrum in KUBEVIZ. This allows the fitting routine to measure widths smaller than the instrumental resolution, but the minimum velocity dispersions may be less well constrained and are only given here for reference. Both components have a range of velocity dispersion, and often have comparable widths (but are simply shifted in velocity), therefore we have avoided referring to them as "narrow" and "broad".

In the kinematic study of JO201 (GASP II) we focused on the Hα component fitted alongside the N[II] lines. In this study we fit all lines shown in Table 3.1 in order to construct line ratio diagnostics, to obtain the metallicity and ionisation parameter.

For most of the analysis, since all lines were required for each diagnostic, the cube was masked to include only areas in which all required emission lines were detected in KUBEVIZ to a signal-noise ratio of 3 or above. This was in addition to the internal flag system used by KUBEVIZ which excludes fits with zero velocity errors

Table 3.1: Emission Lines considered in this analysis. Table columns are: (1) Name of emission line, with "forbidden" transitions denoted by square brackets. (2) Wavelength in air

Line	λ (Å)	Line	λ (Å)
Hβ	4861.33	[NII]	6548.05
[OIII]	4958.91	Hα	6562.82
[OIII]	5006.84	[NII]	6583.45
[OI]	6300.30	[SII]	6716.44
[OI]	6363.78	[SII]	6730.81

or velocity dispersions narrower than the instrumental resolution.

The resulting line flux maps for Hα, [SII], [OIII], [NII] and Hβ are shown at the top of Figure 3.3. The Hα map prominently highlights the star forming knots and steep leading edge on the disk, whereas the [OIII] line shows the strong emission originating from the AGN at the galaxy centre.

3.4 Emission-Line Diagnostics

3.4.1 Gas Ionisation Mechanism

BPT line diagnostic diagrams were produced from the Hα, [OIII], [NII] and Hβ lines to distinguish the ionisation mechanism of the nebular gas.

Fig 3.4 shows the [OIII]/Hβ, [NII]/Hα line diagnostic diagram for the primary (top) and secondary (bottom) components of the two-component fits. The left side of the figure shows the position of each spaxel in BPT space, coloured by the excitation mechanism according to the intersecting lines on the figure. The star forming/composite/AGN regions are defined by the Kauffmann et al. (2003) and Kewley et al. (2001b) lines and the AGN/LINER separator is taken from Sharp & Bland-Hawthorn (2010). The plot on the right shows these spaxels in situ on the galaxy, revealing the regions in which each ionisation mechanism dominates.

The majority of the AGN emission comes from the very central region of the galaxy disk. The composite emission emanates from the diffuse gas which surrounds the disk and between the knots, which themselves are dominated by star formation. A small cluster of spaxels dominated by LINER type sources is visible on the galaxy to the left of the AGN dominated central region. Most of the secondary component lies within the composite region. This generally corresponds to the diffuse gas surrounding the disk and knots as seen in

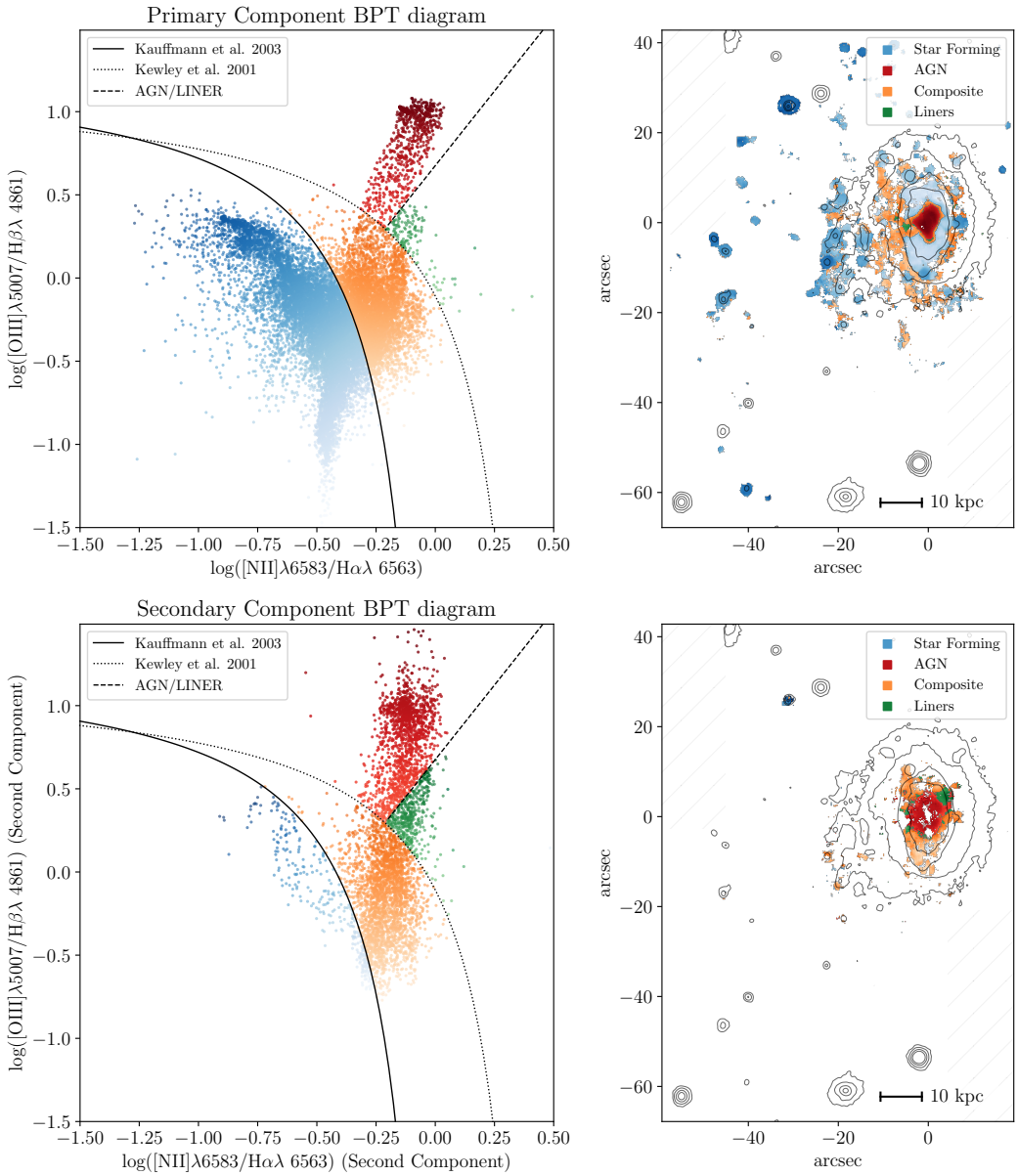

Figure 3.4: [OIII], [NII] BPT line-ratio diagnostics for all spaxels with S/N > 3 on the primary (top) and secondary (bottom) component of the two-component fits (left), mapped on top of the galaxy (right). The black lines separating different ionisation sources on the left panel come from: Kauffmann et al. (2003), to separate star formation dominated regions from composite; Kewley et al. (2001b), to separate composite from AGN/LINER regions; and the AGN/LINER separator, taken from Sharp & Bland-Hawthorn (2010). The contours on the right panel correspond to the stellar continuum fitted around the Hα line for context. The colour gradients are included to show variations within each region of the BPT diagram. The distribution of the ionised gas in the galaxy prominently shows an AGN region in centre of the galaxy, and knots with ongoing star formation, that are surrounded by ionised gas lying in the composite region of the BPT diagram.

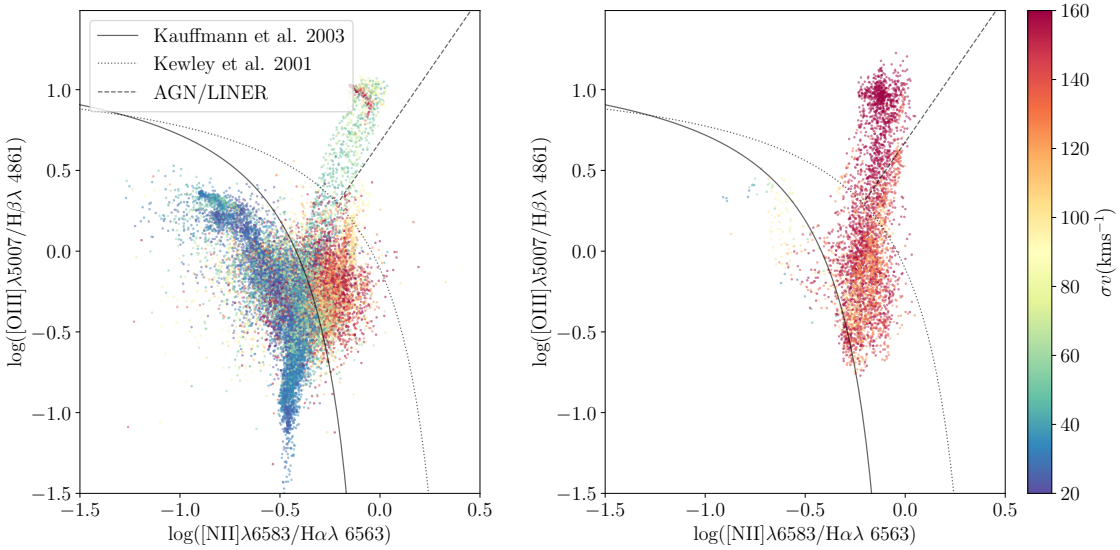

Figure 3.5: [OIII], [NII] BPT line ratio diagnostics for the primary (left) and secondary (right) component for all spaxels with primary component detected to S/N < 3, coloured by Hα velocity dispersion. The dark blue clumps on the star forming branch in the left panel indicate the denser star forming knots in the galaxy's tail, while the large cluster of points with velocity dispersion 120 to 150 km s^{-1} in the composite region is comprised of ionised gas resulting from the interaction with the ICM. Finally, the broader lines are naturally located in the AGN-ionised region. In the right panel the secondary component, which traces the stripped disk and the nuclear region, is located between the composite region, consistent with turbulent, excited gas being stripped from the galaxy, and the AGN region to the upper right of the figure.

the primary component, but also comes from broad velocity tails in the line of sight coming from the edges of the galaxy disk, where the line-of-sight stripping produces a tail in the velocity distribution (see GASP II).

To illustrate this, we have shown in Figure 3.5 the same BPT maps as in the left panels of Figure 3.4, this time coloured by the velocity dispersion of the gas, as measured from the broadness of the emission-line fits in GASP II. In the case of the primary component this illustrates that the knots are kinematically colder (see also Fig. 13 of GASP II), consistent with the idea that the knots condense out of the stripped gas, collapsing and forming stars, as confirmed by UV observations which show in-situ star-formation in the stripped tails (George et al., 2018). These kinematically cold, star forming knots are a feature of other GASP jellyfish galaxies (Poggianti et al. 2018 in press) and other strongly ram-pressure stripped Jellyfish galaxies in the literature such as ESO 137-001 (Fumagalli et al., 2014; Fossati et al., 2016), UGC6697 (stripped edge-on; Consolandi et al., 2017) and SOS 114372 (Merluzzi et al., 2013: also included in the GASP sample as JO147).

The AGN region exhibits broader lines in general and this peaks within the cluster of AGN-dominated points at the upper right. The cloud of higher velocity dispersion points within the composite region results from the diffuse stripped gas which surrounds the disk and the knots. In the case of the secondary component, which traces mainly the diffuse or nuclear gas, the majority of points lie within the composite and AGN dominated regions, originating from the stripped gas in the outer disk, and the broad AGN emission in the centre respectively.

3.4.2 Metallicity and Ionisation Parameter

Using the software pyqz (Dopita et al., 2013) the metallicity ($12 + \log(\mathrm{O/H})$) and ionisation parameter ($\log \mathrm{Q}$) were calculated for each spaxel using the direct estimate interpolated from the [NII]/[SII]+ vs [OIII]/[SII]+ diagnostic (where [SII]+ refers to the sum of the two SII components). The metallicity and ionisation parameter measurements are only valid in HII regions, therefore spaxels outside the star forming region of the BPT diagram were masked out. The pyqz python module uses a finite set of diagnostic line ratio grids produced using the MAPPINGS code, onto which the selected combination of line ratios are interpolated. We used a version of pyqz modified to use the MAPPINGS IV grids which are calibrated over a larger range $7.39 < 12 + \log(\mathrm{O/H}) < 9.39$ than the MAPPINGS V grids (F. Vogt, priv comm.). A sample grid is shown

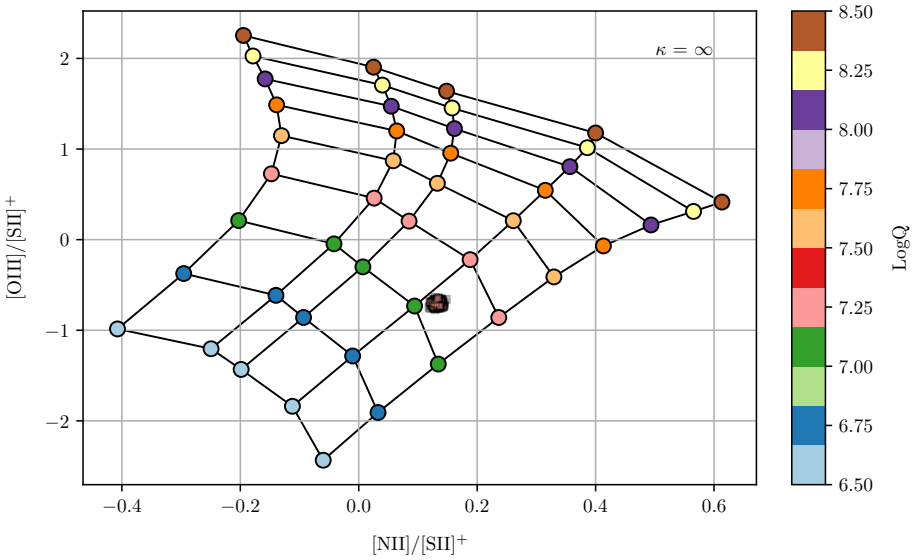

Figure 3.6: Example pyqz grid for a sample spectrum in the galaxy disk. The figure shows, in the lower middle, the clustering of sample values taken from the probability density function (see `http://fpavogt.github.io/pyqz/understanding.html` for details on the internal process of pyqz) of the measured line ratios which are interpolated onto the grid shown. For each spaxel, any line ratio grids with values within the suitable range are used and the results are combined.

in Figure 3.6. Some of the MAPPINGS grids are folded in line-ratio space, yielding degenerate results on their own, however the [NII]/[SII]+ vs [OIII]/[SII]+ diagnostic used here does not suffer this.

The results from pyqz for the metallicity and ionisation parameter are shown in Figure 3.7. We find that the metallicity varies by ~ 0.6 dex in the ionised gas and has similar values to those in other GASP jellyfish galaxies, such as JO204 (Gullieuszik et al., 2017) and JO206 (Poggianti et al., 2017b). The most metal-rich gas is found in the disk of the galaxy up to values of ~ 9.2, with intermediate metallicities of ~ 8.9 in the stripped gas. The most metal-poor gas resides in the more distant knots $>$ 40kpc from the galaxy, with $12 + \log(\mathrm{O/H}) \approx 8.7$. For comparison, the Tremonti et al. (2004) relation gives an average metallicity of 9.06 for a galaxy of this stellar mass. The outwardly-decreasing trend is better seen in the star-forming knots (Section 3.5). Comparing with undisturbed galaxies, JO201 has a higher central metallicity compared to galaxies observed with CALIFA in Sánchez-Menguiano et al. (2017), (with stellar masses ranging over 9.18-11.30$\mathrm{M}_{\odot}$) whilst the range of metallicity values within JO201's disk and tails is similar to that of the

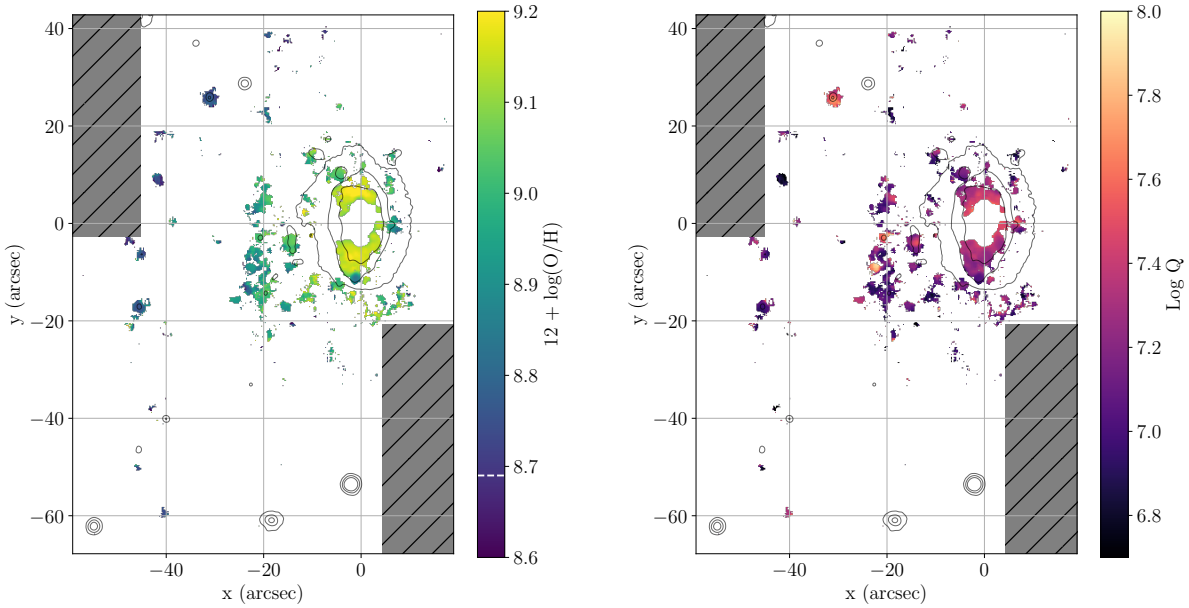

Figure 3.7: Metallicity (*Left*) and Ionisation parameter (*Right*) of stripped gas for HII regions calculated using pyqz as described in the text. Black contours show stellar continuum fitted around the Hα line for context. Solar oxygen abundance (8.69, Asplund et al., 2009) is marked as a white dashed line on the metallicity colourbar. The highest metallicities are visible in the disk of the galaxy, with lower metallicities in the tails and knots. This outwardly-decreasing trend is further explored in Fig 3.8 for the star-forming knots. The right hand side of the figure reveals that the highest ionisation parameters are found within the disk and some knots within the tails.

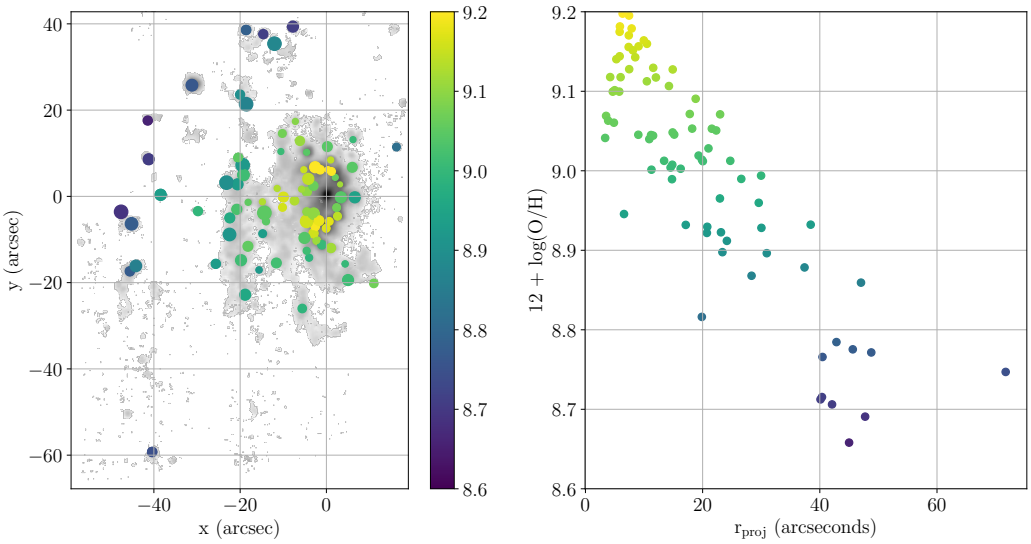

Figure 3.8: *Left:* Metallicity calculated using pyqz direct estimate for integrated spectra of SF knots shown over grey Hα linemap. *Right:* Metallicity of knots from left panel against their projected distance r_{proj} from centre of disk. The figure shows the metallicity of the knots decreasing outwardly from the galaxy centre, with more distant knots having generally lower metallicities.

arm regions of the CALIFA galaxies.

The ionisation parameter, which indicates the ratio of the ionising photon density to the Hydrogen density, describes the degree of excitation in the HII regions. In the results of pyqz, the ionisation parameter Q is defined as the ratio of ionising photons per unit area per second to the gas particle number density, as outlined in Dopita et al. (2013) (This definition can be converted to the dimensionless ratio $\mathcal{U}$ of ionising photons to particle density by dividing by the speed of light, $\mathcal{U} = Q/c$). The value of the ionisation parameter measured here is low in general with a median value of (~ 7.1) in the disk and of (~ 7.3) in the tails. These values, like the metallicity, are similar to those observed in other strongly stripped GASP jellyfish.

3.5 Star Forming Knots

The bright star forming knots within the tail of the galaxy are a common feature in many GASP sample galaxies and other observed jellyfish galaxies. To further study the emission properties of these knots, the

spectra within circular masks were binned spatially and lines were fitted to the resulting total spectrum using the KUBEVIZ mask function, which fits emission lines to the integrated spectra within each mask. The positions and radii of each knot were obtained using a custom script, described in full detail in Poggianti et al. (2017b), in order to produce the masks. The emission line fluxes measured by KUBEVIZ were subsequently corrected for internal dust extinction using the same calculation as described in section 3.2.2. In total, 85 knots were found, of which 63 lie within the star-forming branch below the Kauffmann line marked on the line ratio diagram. The measured line fluxes were fed into pyqz to calculate direct estimates of the metallicities.

The left side of the plot in Figure 3.8 shows the spatial position of each knot against the galaxy. The size of each point scales with the size of each knot and the colour is indicative of the direct estimate of the metallicity as computed by pyqz. The plot reveals a general decrease in the metallicity of the knots with distance from the galaxy disk, with the highest metallicities in the disk and lower values in the most distant knots. This outwardly decreasing trend is better visualised in the right plot of the figure, which shows the metallicity of each knot against the projected distance from the galaxy centre. The metallicity gradient revealed by the knots in JO201 is similarly observed in other GASP galaxies (see Franchetto et al. in prep.), and it is consistent with the mechanism of outside-inward stripping, whereby the most distant, lowest metallicity gas from the galaxy is stripped first, followed by subsequently higher metallicity gas closer to the centre. In fact, semianalytic models of galaxies in clusters (Gupta et al., 2017) have invoked outside-in gas stripping to explain, at least partially, the cluster scale (integrated) metallicity gradients observed in galaxy clusters (see e.g. Ellison et al., 2009).

Figure 3.9 shows the star-formation, gas density and gas mass calculated as in GASP I, for the knots in JO201. The first plot shows the distribution of star-formation rate (SFR) for knots below (red) and above (green) the Kauffmann et al. (2003) line of the BPT diagram. The star-formation rates are calculated using the dust extinction and stellar absorption corrected Hα luminosity in the (Kennicutt, 1998) method,

$$\mathrm{SFR} = 4.6 \times 10^{-42} L_{\mathrm{H}\alpha}, \tag{3.2}$$

transformed to a Chabrier IMF, as described in GASP I.

We note that the SFRs obtained here are up to 30% lower (differing by 0.1-0.5$\mathrm{M}_{\odot}\mathrm{yr}^{-1}$) than those

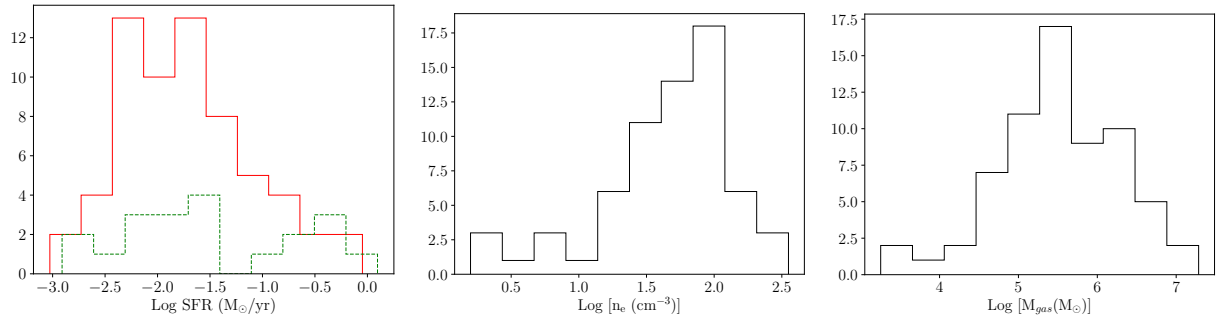

Figure 3.9: *Left:* Distribution of SFR for star-forming (red, solid) and composite (green, dashed) knots. The central knot, dominated by AGN emission, has been excluded. *Middle:* Gas density distribution of individual knots *Right:* Distribution of ionised gas masses within knots.

computed from far ultraviolet emission by George et al. (2018) (using a Salpeter IMF), which could be attributed to the uncertainty in the dust extinction correction. The SFRs are slightly higher than those found in both JO206 (Poggianti et al., 2017b) and JO204 (Gullieuszik et al., 2017).

The second plot in Figure 3.9 shows the density of the ionised gas calculated using the ratio of the [SII] 6716 and [SII] 6732 lines. The calculation is made using the Proxauf et al. (2014) calibration for $T = 10{,}000K$, obtained with modern atomic data with CLOUDY, valid within the range $R = [\text{SII}]6716/[\text{SII}]6732 = 0.4 - 1.435$. The densities are similar to those observed in JO204 and slightly higher than the star forming knots of JO206.

The gas densities calculated here were used to estimate the mass of ionised gas in the star forming knots, shown in the third plot of Figure 3.9. These masses were computed from the Hα luminosities following equation 13.7 in Osterbrock & Ferland (2006) as in Boselli et al. (2016) and Poggianti et al. (2017b).

$$M_{\text{gas}} = N_{\text{protons}} \times m_p = \frac{L_{\text{H}\alpha} \times m_p}{n\alpha_{\text{H}\alpha} h\nu_{\text{H}\alpha}} \tag{3.3}$$

Case B recombination is assumed with $T = 10{,}000K$, and it is assumed that the gas is fully ionised.

In comparison, these masses are distributed similarly to JO206, and are about an order of magnitude higher than the gas masses measured for JO204, although the latter is skewed by a large number of lower mass knots.

The similarity in the distributions of each parameter of the star forming knots shows consistency in the

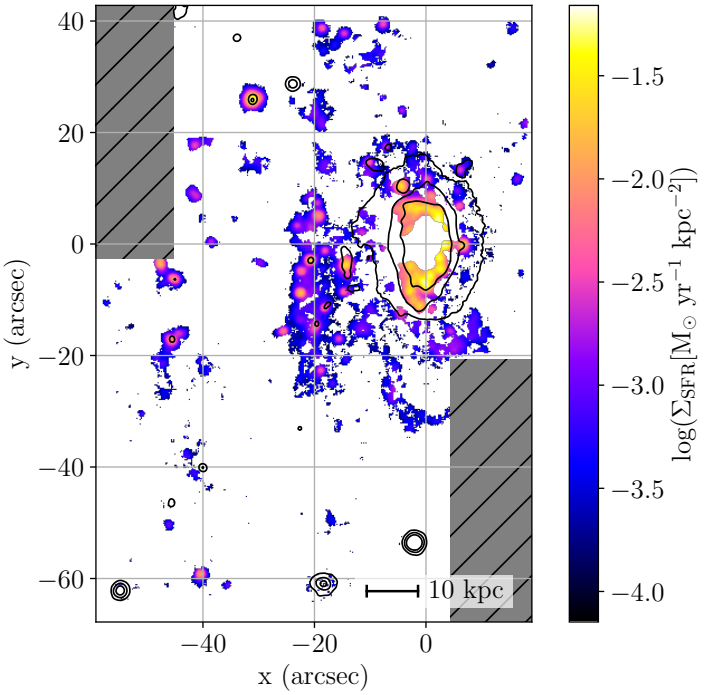

Figure 3.10: Star-formation rate surface density within JO201 calculated for each spaxel ($M_{\odot}yr^{-1}kpc^{-2}$). Black contours show stellar continuum fitted around the Hα line for context. We observe high star-formation rate surface densities in the leading (western) edge of the disk, triggered by the interaction with the ICM. High Σ_{SFR}s are also seen in the collapsed knots trailing behind the galaxy and in particular within the bright knot in the north-eastern region of the image.

process of stripping between each of the galaxies. The properties of the resulting clumps of gas may not be dependent on the galaxy itself or the orbital properties, but this will be clarified as more GASP galaxies are added to this comparison.

3.6 Star Formation

It is interesting to examine the distribution of star-formation activity within the galaxy, since it can reveal information about the ram-pressure stripping history and the disruption and compression of the gas component.

The star-formation rates for each spaxel are shown in figure 3.10. The star-formation rate surface density,

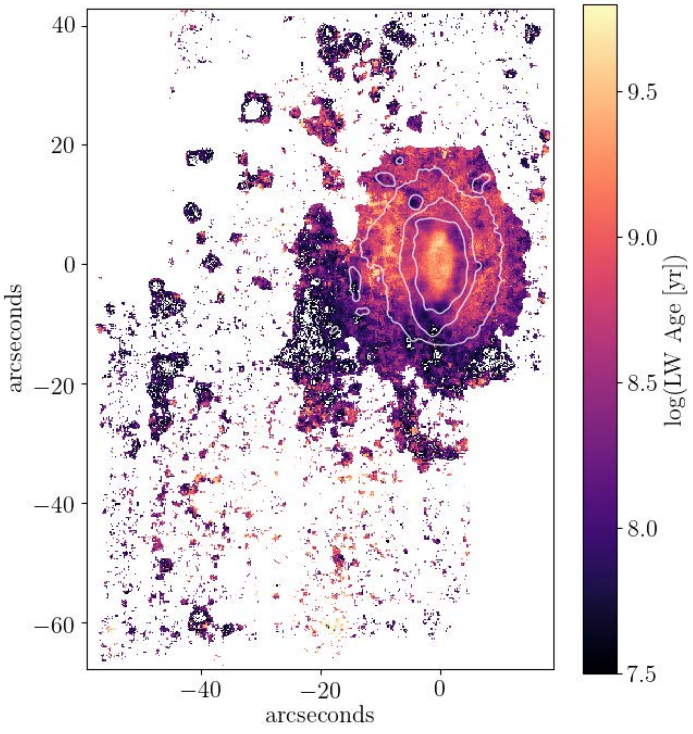

Figure 3.11: Luminosity weighted stellar age (colourbar) shown along with of stellar continuum isophotes (white contours). A clear age gradient is seen, with the oldest stars residing around the disk and lower ages in the tails, whilst a ring of young stars is visible within the disk surrounding the centre.

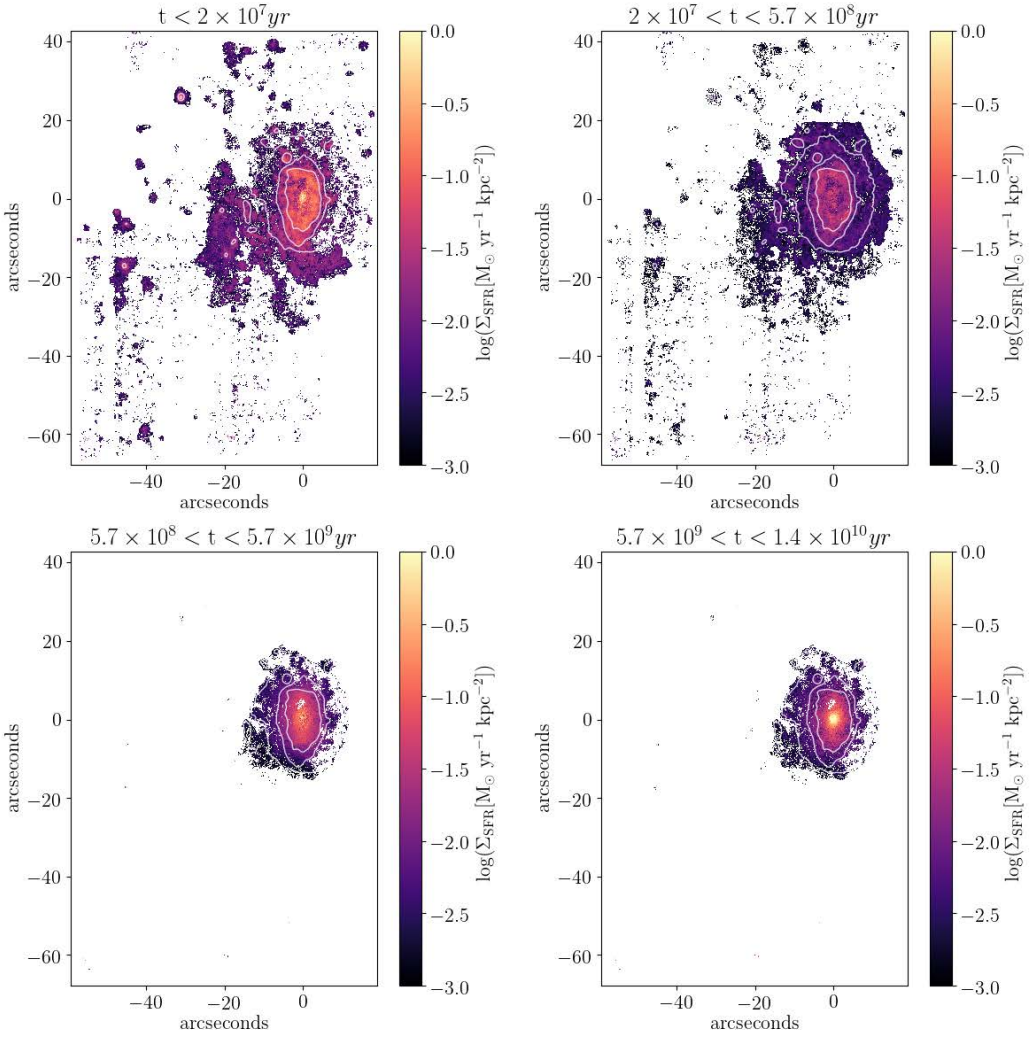

Figure 3.12: Star-formation rate surface density grouped into several stellar age ranges, indicating the average SFR per kpc^2 during the last $2 \times 10^7 yr$ (top left), between $2 \times 10^7 yr$ and $5.7 \times 10^8 yr$ (top right), $5.7 \times 10^8 yr$ and $5.7 \times 10^9 yr$ and $> 5.7 \times 10^9 yr$ ago. The top two plots have been masked to S/N$>$ 0.5, whilst the bottom plots have been masked to spaxels of S/N$>$ 3 and with a contribution to the stellar continuum above 5% The figure reveals recent star formation occurring in the tails and knots, as well as the leading edge of the disk, with the oldest stars residing in the bulge and disk of the galaxy. White contours indicate continuum isophotes.

$\Sigma_{\rm SFR}$, is calculated using the Hα luminosity, corrected for dust extinction and stellar absorption, in the (Kennicutt, 1998) method transformed to a Chabrier IMF, for each individual spaxel with an Hα S/N > 3.

The SFR surface density values across JO201 are typically around $0.001 M_{\odot} yr^{-1} kpc^{-2}$ for diffuse regions and $0.02 M_{\odot} yr^{-1} kpc^{-2}$ for denser blobs and regions within the galaxy disk. The bright trailing knots to the east of the galaxy are therefore strongly star forming, with a particularly active region around 5kpc in diameter to the north east of JO201. As well as within the trailing knots, a ring of strong star formation is apparent within the disk, where the gas is likely to have been compressed by interaction with the ICM. Within this ring a decrease in the star formation is coincident with the AGN emission, suggesting AGN feedback suppressing star formation in this region. This is also suggested by the deficit of Hα emission coincident with the [OIII] emission in Figure 3.1 and will be further investigated in George et al. (2019).

Overall, the range and spatial distribution of the star-formation rates obtained for JO201 are comparable with those observed in strongly stripped galaxies which are moving on the plane of the sky such as JO206 (Poggianti et al., 2017b) and JO204 (Gullieuszik et al., 2017) in the GASP sample. In particular, the dense regions of intense star formation are often observed in the tails of jellyfish galaxies. (Fumagalli et al., 2011; Kenney et al., 2014; Boselli et al., 2018a)

Vulcani et al. (2018) found that the total integrated SFR within the galaxy and trailing gas is $6 \pm 1 M_{\odot} yr^{-1}$, which is high for the stellar mass of the galaxy. In fact, the same authors find that the SFR in the disk of JO201 is around 0.4-0.5 dex above the main sequence of a control sample of non-stripped disk galaxies, which is among the highest offsets found in the sample.

Moreover, Moretti et al. (2018b) presented APEX observations of JO201, finding CO emission in the disk that partly traces the velocity of the stellar disk, and partly the velocity of the stripped Hα knots. Further from the disk the molecular gas does not follow the velocity of the Hα gas. The large depletion times measured for the molecular gas suggest that the majority will be dispersed into the ICM.

In comparison with the far ultraviolet observations presented in George et al. (2018), which have lower spatial resolution than the MUSE data presented in this study, we find that although the measured SFR values differ by a factor of up to 30%, between 0.1-0.5$M_{\odot} yr^{-1}$, the two methods reveal the same trends and the same pattern of star formation localised in collapsed knots. The extinction in UV and Halpha follows different laws. Since the UV extinction was derived using the balmer decrement, there may be uncertainty

in the correction, accounting for the deviation in the SFR values.

The bright knots in the tails of JO201, which have high velocities relative to the stellar disk, therefore appear to have originated from in-situ star formation happening in the stripped (trailing) gas.

3.7 Stellar Populations

We calculated the ages of the stellar populations across the galaxy using the SINOPSIS spectrophotometric fitting code (c.f. Section 3.2.4, and Paper III: Fritz et al., 2017). The SINOPSIS code works by calculating the average observed flux in a predefined set of spectral bands, selected to avoid prominent emission/absorption lines, as well as the equivalent widths of significant lines, outlined in Fritz et al. (2017). These are then compared to the features of model spectra, constructed from a subsample drawn from 200 mono-metallicity simple stellar population spectra with ages between 10^4 and 14×10^9. The spectra are multiplied by an appropriate estimate for the stellar mass, and dust attenuation is applied before summing to produce the final model spectrum. To minimise uncertainties in the stellar ages, which cannot accurately be derived, the properties calculated over the initial age range are combined into larger age bins. The number of bins and their ranges were selected based on simulations performed in Fritz et al. (2007).

A map of the luminosity weighted stellar age in JO201 is shown in Figure 3.11. The plot shows a ring of lower stellar age approximately 3-5kpc in radius around the centre of the disk and a decreasing stellar age into the tails compared with the outer edges of the disk. The decrease in stellar age along the leading edge and in a ring around the disk is consistent with a burst of recent star formation occurring due to compression of the gas as the galaxy collides with the ICM. This increases the fraction of young stars in that region and lowers the observed luminosity weighted age.

Beyond the outermost contours of the stellar continuum, the older stellar population rapidly diminishes and the tails contain only young stars. The stellar age further decreases in the collapsed knots within the stripped gas, as a result of the onset of star formation. This gradient in stellar age from the disk to the tails is similarly observed in JO206 (Poggianti et al., 2017b) and JO204 (Gullieuszik et al., 2017).

From the SINOPSIS fits, we further computed the star-formation rate surface density in different bins of stellar age with the intention of seeing the consequences of ram-pressure stripping on the star-formation

history of the galaxy. This is shown in Figure 3.12. The two oldest stellar component bins (between $5.7\times10^8 yr$ and $5.7 \times 10^9 yr$ ago, and $> 5.7 \times 10^9 yr$) are dominated by star formation in the central region of the galaxy and no stellar component of this age is detected outside the disk (i.e. the tails are not seen). More recent bursts of star formation (between $2 \times 10^7 yr$ and $5.7 \times 10^8 yr$ ago) can be seen along the leading edge of the disk and some of the stripped tails. Such activity is very likely triggered by ram-pressure as the galaxy first interacted with the dense ICM. Subsequently, in the last $2 \times 10^7 yr$, star-formation appeared in the knots within the long tails of stripped gas. Across the entire disk and tails of the galaxy, approximately 38% of the stellar mass is in the youngest stellar population, according to SINOPSIS.

Our findings are similar to the distribution of stellar populations seen in Poggianti et al. (2017b) within JO206, with older stellar populations dominating the disk and a younger stellar component reaching further into the tails. A lack of very young stars can be seen along the leading edge of the galaxy, followed by a region where the gas has been compressed or stripped by the ICM. This can also be seen in JO204 (Gullieuszik et al., 2017).

3.8 Stripping Timescale and Length of the Stripped Tails

It is possible to use different observable parameters of the galaxy and its host cluster, to estimate the time that the galaxy has been experiencing gas stripping. In this section we compare several independent calculations.

3.8.1 Stripping Timescale from an Orbital Analysis

In previous GASP studies (Bellhouse et al., 2017; Fritz et al., 2017; Gullieuszik et al., 2017; Poggianti et al., 2017a; Jaffé et al., 2018) we have used position-velocity phase-space diagrams of the cluster galaxies to infer the intensity of ram-pressure stripping, which, combined with the extent of the H_α emission in the disk, can be used to estimate the amount of gas removed (see Jaffé et al., 2015, 2018, for details on the method). One of the main caveats to this analysis is the uncertainty introduced by the projected distances and velocities that observations allow to measure. In this regard however, JO201 has a great advantage: given that it is being significantly stripped along the line of sight, we can assume that the measured projected velocity of the galaxy with respect to the cluster mean, is close to the true 3D velocity within the cluster. The observed

projected clustercentric distance however is more likely to be an underestimation of the real 3D distance from the cluster centre.

In GASP II we estimated the amount of stripping produced in JO201 based on its current location (projected distance 360 kpc from the cluster centre) and velocity (3363.7km s^{-1} or $3.4 \times \sigma_{\rm cl}$) in the cluster (close to pericentre), and compared it with the observed truncation radius (r_t) measured from the relative extent of the Hα emission relative to the stellar disk.

We have re-done the ram-pressure calculation (Jaffé et al., 2018) finding stronger ram-pressure stripping in JO201 than previously estimated. The corrected value of the ram-pressure at the position and velocity of JO201 is $P_{\rm ram} = 2.7 \times 10^{-11}$ N m^{-2}, and the anchoring pressure of the galaxy $\Pi_{\rm gal}$ is 5.2×10^{-11} N m^{-2} at the centre of the galaxy, using a revised disk scale-length of $r_{\rm d,stars} = 2.5$ kpc, which correspond to the mean $R_{\rm d,s}$ of disk galaxies with a mass similar to JO201 (see Fig. 1 in Jaffé et al., 2018). We chose to use this value rather than a fit to the light profile of JO201, because the latter could be affected by the jellyfish morphology. Our revised modelling suggests that the ram-pressure by the ICM should have almost completely removed gas from the galaxy at its current location in projected phase-space (see solid line in Figure 3.13). This is somewhat consistent with our observations, which suggest there is still some gas left in the inner $\sim$ 9kpc of the disk (although disturbed in velocity with respect to the smooth rotation of the stellar disk; GASP II). The radius at which the gas becomes unbound from the stellar disk, and thus the total amount of gas lost, is difficult to measure (Gullieuzik et al. in prep), but from Fig. 15 in GASP II we estimate that the $H\alpha$ truncation radius in JO201 is $r_t \lesssim 9$ kpc, which translates to a total gas mass loss $> 40\%$, assuming that $R_{\rm d,gas} = 1.7 \times R_{\rm d,stars}$ prior to stripping. The possible discrepancy between the observed r_t and the predicted amount of stripping (Figure 3.13) can be explained by the combination of an underestimated clustercentric distance (due to projection), and the fact that Gunn & Gott (1972)'s prescription of ram-pressure assumes an instantaneous stripping of gas in an infinitely thin disk, a simplification that will over-predict the amount of gas stripping (see Section 3.5 of Jaffé et al., 2018, for a summary of all the caveats).

What we can be certain of from our observations is that the the galaxy is close to pericentre (and thus peak-stripping) and that there has been a significant amount of gas stripping by ram-pressure which has affected even the inner-most parts of the disk.

In order to estimate the timescale of stripping, it is necessary to know at which point in phase-space the

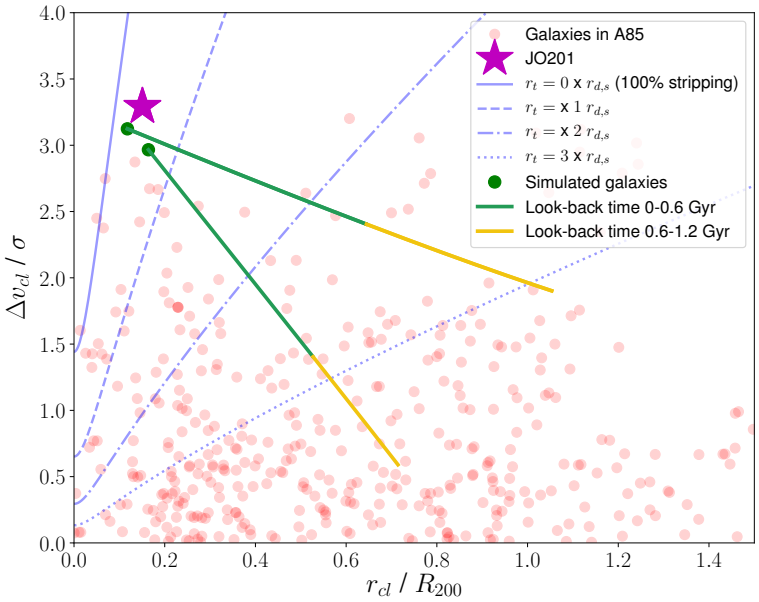

Figure 3.13: Projected position-velocity phase-space diagram of all the galaxies in A85 (pink circles), including JO201 (star). Blue curves correspond to the estimated position and velocity of a JO201-like disk galaxy undergoing ram-pressure stripping by A85's ICM. The solid blue line that passes near the location of JO201 corresponds to total gas stripping via ram-pressure, using our revised derivation of $P_{\rm ram}$ and $\Pi_{\rm gal}$. The dotted/dashed lines instead corresponds to an earlier stage of stripping, with a gas truncation radius $r_t = 1$, 2, and 3 $\times R_{\rm d,stars}$. Finally, the coloured tracks correspond to orbits of simulated haloes in a massive cluster whose position in phase-space at $z = 0$ (green circles) is close to the location of JO201. The colours of the tracks indicate look-back time.

galaxy started to lose gas. The answer is tightly linked to the orbital history of the galaxy, which we cannot measure directly but can infer from simulations.

We use N-body and hydrodynamical cosmological simulations from YZiCS (Choi & Yi, 2017; Rhee et al., 2017) to track the orbits of haloes passing near the core of a massive ($9.23 \times 10^{14} {\rm M}_{\odot}$) cluster at high speeds, like JO201 in A85. Using a random projection, we selected haloes whose end position in projected phase-space were the closest to the location of JO201, i.e. cluster-centric distances $r_{cl} < 0.5 \times R_{200}$, and high line-of-sight velocity with respect to the mean velocity of the cluster: $|\Delta v_{cl}| > 2.75\sigma$, where σ is the velocity dispersion of the cluster. This selection yielded 2 simulated galaxies (see the circles in Figure 3.13) which

we tracked in phase-space back in time until an epoch where the model galaxies had not yet experienced significant gas loss via stripping, i.e. to the right of the dotted blue line which corresponds to $\gtrsim 50\%$ of the total gas mass stripped. At this point the galaxy will have a gas deficiency of ~ 0.3, which is the threshold typically used to separate HI-rich galaxies from HI-deficient ones (Haynes & Giovanelli, 1984). Although there is some uncertainty in the orbit of JO201 and the moment when stripping began, the model orbits indicate a timescale of $t_{\rm str} \sim 0.6 - 1.2$ Gyr from the beginning of significant gas stripping until the present epoch of "peak" stripping near pericentre. This is shown by the yellow and green colours in the orbital tracks in Figure 3.13.

3.8.2 Timescale of Star-Formation in the Stripped Tails

An independent constraint of the timescale of stripping comes from the star-formation in the stripped tails, which presumably took place shortly after the stripping started (Tonnesen & Bryan, 2009, 2010, 2012).

An estimate of the average value of the stellar age was obtained by running SINOPSIS on the integrated spectra of each knot. Two possible values of the stellar age can be defined: luminosity-weighted, and mass-weighted (Cid Fernandes et al., 2005), with the first definition being more directly observable and the second, while more physical, being more difficult to derive due to the strongly changing M/L as a function of the stellar population age.

The fact that the M/L of simple stellar populations is an increasing function of age, might pose a well known problem when using stellar population synthesis models to recover the properties of galaxies, in particular their star formation histories. In fact, the appearance of features due to a given stellar population in an observed spectrum depends both on the amount of stars and on their M/L. Since the stellar blobs we are analysing are formed in situ and outside the galaxy, the age of their stars must be younger than the age at which ram pressure started affecting the gas of the galaxy (Poggianti et al. 2018 in press). This is why when analysing the spectra of the blobs, we have set an upper limit of 2×10^9 yr to the age of the stellar populations used for the spectral fitting. While being a rather conservative choice, this allows us to avoid spurious, artificial contributions in terms of stellar mass, and hence mass-weighted age, from older stars which, because of their very high M/L, would not provide a significant contribution to the observed spectrum.

Furthermore, once the star formation history was derived, we have calculated the contribution to the light of the observed spectra of each stellar population. If the contribution was less then 5%, that population was not taken into account for the calculation of the mass-weighted age. We chose a threshold of 5% because, for the typical S/N of the spectra we have analysed, this is the limit for which the fit is still acceptable.

The resulting age estimates are shown in Figure 3.14, where the time since earliest star formation is shown for each knot against the projected radius for knots located in the tails outside the stellar disk ($r_{\rm proj} > 20$kpc). Assuming a constant star formation history, the mass weighted stellar age will be the midpoint between the oldest and youngest stellar ages, therefore we approximate the time since earliest star formation as $2\times$ the mass weighted stellar age calculated using SINOPSIS. The time taken for the knots to collapse prior to star formation is hard to accurately predict as their initial densities and locations in the disk are not known. An estimate of the gravitational collapse time for a cloud of typical initial density was found to be more than an order of magnitude lower than the star formation timescales ($\sim$ 0.07Gyr), therefore the collapse times would not alter these predicted timescales significantly enough to necessitate their inclusion. Most of the star-forming knots in the tails have mass weighted stellar ages close to or less than 0.5 Gyr (between 10^7 and 7×10^8 yr), suggesting that initial star formation began approximately 1 Gyr ago.

Interestingly, the figure also suggests (with a large scatter) a possible age gradient with the more distant knots having slightly younger stellar populations.

This type of stellar age gradient along the tail has been observed in IC 3418 by Fumagalli et al. (2011); Kenney et al. (2014), and also in RB 199 by Yoshida et al. (2008), who attribute the age gradient to the movement of the stripped gas from which the knots form. The collapsed knots are left along the trajectory of the gas as it is stripped away from the galaxy. Once collapsed, the stars are no longer susceptible to ram-pressure, therefore knots that have collapsed earlier will both be preferentially situated closer to the galaxy and also contain older stars.

3.8.3 Physical Length of the Stripped Tails

Given the extreme ram-pressure conditions that JO201 has been experiencing for the past $\sim$ 1Gyr we expect the extent of the stripped tails to be large.

For many jellyfish galaxies the physical size of the tails is not far from the measured projected size because

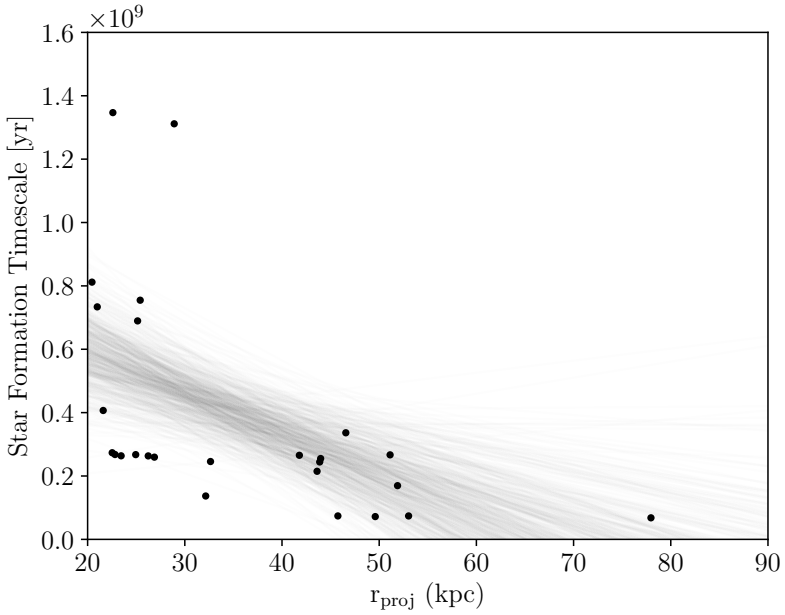

Figure 3.14: Star Formation Timescale for knots > 20kpc from JO201. Black points show the time since initial star formation began, approximated as 2× the mass weighted stellar age calculated using SINOPSIS. A linear fit was applied using the python package linmix and transparent lines show samples from the posterior, indicating the scatter in the fit.

the direction of motion is close to the plane of the sky. Because of the line-of-sight motion of JO201, the physical (unprojected) length of the stripped gas tails is not trivial to compute. However, we can obtain an estimate of the tail length by using a toy model to follow the motion and dynamics of a cloud of gas as it is accelerated away from the galaxy after being stripped by ram pressure. We model the infall of the galaxy into the potential well of a cluster with mass and density profiles derived from the X-Ray distribution of A85 (Chen et al., 2007). The galaxy begins at the virial radius of the cluster, 2.4Mpc, moving radially at 1500km s^{-1} (consistently with the orbits shown in figure 3.13). It then accelerates as it falls into the potential well of the cluster. The cloud also falls into the cluster potential well, but its motion is additionally affected by acceleration due to ram pressure and, counteracting the ram pressure, acceleration from the potential well of J0201. The latter is modelled as a spherical NFW halo ($M_{200} = 1.0 \times 10^{12}$ $M_{\odot}$, c=15; typical for a galaxy with this halo mass), and a 3D exponential disk (total mass= 4.0×10^{10} $M_{\odot}$, r_{exp}=3.62 kpc, h_z=0.25 kpc) using techniques described in Smith et al. (2015), where all parameters are chosen to match the JO201 observations. We ran the model for a gas cloud with mass 4×10^5 $M_{\odot}$ with a radius of 300 pc, which are typical values for HI clouds in the ISM (Vollmer 2001). The initial position of the cloud is in the outer disk of the galaxy at $4 \times R_{\rm d,stars}$, although our results are not strongly sensitive to this choice. By the time the model galaxy reaches the current velocity and projected radius of JO201 within the cluster, the gas cloud has been stripped to 94kpc from the galaxy and has been accelerated until it has a velocity of 1200km s^{-}1 relative to the galaxy, which is consistent with the largest velocity difference between the Hα gas tails and the stars in JO201 (GASP II). We note however that the estimated length of the tails along the line of sight (and the velocity reached by the gas cloud) is sensitive to the mass of the cloud: A cloud of higher mass (5.5×10^5 $M_{\odot}$) reaches a shorter distance (68kpc) and relative velocity (1000km s^{-1}). In our model, the time required for the galaxy to reach this point since crossing the virial radius of the cluster is between 0.9-1.0Gyr, which lies within the range of estimates for the time since JO201 began stripping (Sec. 3.8.1).

Our estimated upper limit to the line-of-sight length of the tails (94 kpc) is comparable to the longest tails observed in jellyfish moving on the plane of the sky such as JO206 (90kpc, Poggianti et al., 2017b) and ESO 137-001 (80kpc, Sun et al., 2010), which again suggests that the velocity vector of JO201 is dominated by the line of sight component.

Bringing together the results of the orbital analysis, star formation timescales and simulations, we find

that JO201 began undergoing stripping between 0.6 and 1.2 Gyr ago as it approached the core of the massive cluster A85 at high speed along the line of sight. This resulted in tails up to 94kpc in length trailing behind the galaxy, which partially collapsed into knots within 0.1 Gyr of initial stripping, forming stars within the past 0.1-0.7Gyr

3.9 Conclusions

This work is part of a series of papers from the GASP (GAs Stripping Phenomena in galaxies with MUSE) (Poggianti et al., 2017b) survey of "jellyfish" galaxies, observed with the MUSE instrument at the VLT. In particular, this study is a direct continuation of chapter 2 (GASP II Bellhouse et al., 2017) which focused on the environment and kinematic properties of JO201, a unique galaxy in the GASP sample subject to extreme ram-pressure conditions (i.e. very high speeds as it crosses the densest part of the ICM) in a trajectory close to the line of sight. In this chapter, we expanded upon the previous study of the ionised gas and stellar kinematics with an analysis of the properties of the stripped gas, including the gas metallicity, ionisation source and ionisation parameter. We also explored the stellar population ages, masses and star-formation across the galaxy, and build a toy model to estimate the timescale of the stripping event.

We summarise our findings in the following:

- We detect several emission lines across the galaxy, including $H\alpha, [NII], [OIII], H\beta$ and [SII]. The $H\alpha$ emission notably extends well beyond the disk of the galaxy, while the distribution of other emission lines such as [OIII] are much more concentrated. The emission lines were used to determine the source of ionisation (via the BPT diagram), gas-phase metallicities and ionisation parameter across the galaxy disk and tails.

- The central region of the galaxy is dominated by broad AGN emission, surrounded by a ring of composite emission. The outer disk and tails are purely ionised by star-formation, concentrated in knots of low velocity dispersion gas.

- The metallicity decreases in the stripped tails with distance from the galaxy disk. Such a metallicity gradient suggests that the outermost, lowest metallicity gas was stripped first, followed subsequently

by gas of increasing metallicity as the stripping continued. This interpretation is supported by the increasing velocity offset of the gas (relative to the stars) at larger distances from the galaxy disk, shown in GASP II.

- The star-forming knots in the leading edge of the galaxy exhibit some of the highest $\Sigma_{\rm SFR}$s in the galaxy, with values up to $6.0 \times 10^{-2} {\rm M}_{\odot} {\rm yr}^{-1} {\rm kpc}^{-2}$. These are likely to have formed as this part of the galaxy was compressed by the interaction with the ICM. In the tails the knots, which most likely formed in-situ from collapsed gas previously stripped from the disk, have lower $\Sigma_{\rm SFR}$ ($\sim 3.1 \times 10^{-3} {\rm M}_{\odot} {\rm yr}^{-1} {\rm kpc}^{-2}$).

- Using SINOPSIS to model the stellar population, we find that the oldest stars are only present in the disk, while the stellar component in the tails only began to form $\lesssim 0.7$Gyr ago. The most recent pockets of star-formation are located in the leading edge of the galaxy and in the knots within the tails.

- We observe a gradient in the stellar age of the star forming knots, with the oldest knots residing closest to the galaxy. A possible explanation is that the knots collapse out of the stripped gas as it moves away from the galaxy, hence older knots collapsed earlier when the stripped gas was closer to the disk.

- From orbital inference, we estimate that JO201 has been exposed to ram-pressure stripping for ~ 1 Gyr. This estimate is consistent with the time since initial star formation in the tails ($\lesssim 0.7$Gyr).

- We use a model to estimate the physical (deprojected) length of the tails of gas stripped from JO201 along the line of sight. During infall of the model galaxy, we find that the stripping causes the tails to extend up to 94 kpc, which is comparable to tails observed in galaxies which are stripped predominantly on the plane of the sky.

Overall, in previous GASP studies (including Bellhouse et al., 2017; Poggianti et al., 2017a; George et al., 2018; Moretti et al., 2018a) and the present study we have exploited the rich MUSE data and other multi-wavelength observations on JO201, undoubtedly one the most spectacular and unique jellyfish galaxies in the GASP survey, to extract the physical properties in and around the galaxy and built a comprehensive view of the physics involved in the interaction between the galaxy and the ICM. In summary, all the different analyses done to this galaxy (in particular, the stellar and gas kinematics, ionisation sources, gas metallicity, and stellar population ages) individually and consistently point toward a scenario of incremental outside-in

ram-pressure stripping of the gas during radial infall into the cluster, on a timescale $\sim$ 1 Gyr. The ram-pressure intensity is very high for this galaxy compared with other jellyfish galaxies because it is travelling close to face-on at supersonic speeds though the hot and dense medium of a massive cluster, and is in a moment in its (radial) orbit close to pericentric passage. The ram-pressure wind is not only able to remove a significant amount of gas from the disk but it is also likely to be pushing some of the gas towards the centre, fuelling the supermassive black hole. At the same time, the gas in the leading edge of the galaxy and in the stripped tails is compressed, giving rise to new episodes of star-formation, which is concentrated into knots.

Moreover, our estimated stripping timescale and ages of the stellar populations in the star-forming knots outside the galaxy confirm that some of the knots in the tails must have formed in-situ, consistent with hydrodynamical models of RPS and observations of this galaxy at other wavelengths (Tonnesen & Bryan, 2009, 2010, 2012; George et al., 2018; Moretti et al., 2018a)

Future studies will make use of the large sample of jellyfish galaxies observed by the GASP survey to quantify, in a statistical way, different aspects of the consequences of RPS, such as the contribution of stripped mass from galaxies into the ICM, and the impact of RPS on the internal properties of galaxies and their subsequent evolution.

Chapter 4

The Morphological effects of Ram-Pressure Stripping on the Arms of Spiral Galaxies

This Chapter consists of the GASP paper "Unwinding the arms of spiral galaxies via ram-pressure stripping", currently in preparation. The introduction has been abridged, since the background has already been given in Chapter 1, whilst some sections have been expanded within the paper. The majority of the paper is of the author's original writing, with due credits for contributions to the text to Rory Smith for the opening of section 4.5

4.1 Introduction

One of the most heavily studied jellyfish galaxies of the GASP survey to date has been JO201, analysed both individually in Bellhouse et al. (2017); George et al. (2018); Bellhouse et al. (2019) and as part of wider studies (Poggianti et al., 2017a and others...). JO201 is a massive galaxy falling into the massive cluster

Abell 85 at supersonic speeds (mach ~ 3.2) close to the line of sight, toward the observer and exhibiting signs of extreme near-face-on ram pressure stripping. The spatial distribution of the stripped knots hinted for the first time the possibility that the spiral arms could be "unwound" or broadened as an effect of the face-on gas stripping by the ICM. (See Bellhouse et al. (2017) and Figure 2 of George et al. (2018)). In this study, we further investigate this effect in JO201 and in the wider sample of GASP galaxies, in the quest for more evidence and a greater understanding of spiral arm unwinding during ram-pressure stripping events.

This chapter is structured as follows. Section 4.2 covers the selection process used to produce the sample in this study, and the resulting galaxies used. In section 4.3 we show the locations of the sample in position, velocity phase-space. Section 4.4 shows the analysis of the MUSE data to measure the spiral arm morphology and trace the distribution of different age stellar populations in the spiral arms. In section 4.5 we show the analysis of simulated galaxies undergoing ram-pressure stripping with different orientations with respect to the ICM wind, comparing with observed galaxies and analysing the effect of unwinding over time throughout infall. Finally in section 4.6 we summarise the results and draw conclusions.

Throughout this study, as with other GASP studies, we adopt a Chabrier initial mass function (IMF; Chabrier, 2003), and a concordance ΛCDM cosmology of $\Omega_{\rm M} = 0.3$, $\Omega_{\Lambda} = 0.7$, $\rm H_0 = 70 km\,s^{-1} Mpc^{-1}$.

4.2 The Sample

In order to investigate and understand the unwinding effect of ram-pressure stripping on the spiral arms of galaxies, we drew a sample of galaxies by visual inspection from the catalog of galaxies in the GASP survey (described in section 1.5). The GASP observations were reduced and processed as explained in GASP I. (Poggianti et al., 2017b), correcting for Milky Way dust reddening using dust values from NASA/IRSA and correcting internal dust extinction using the balmer decrement in the Cardelli et al. (1989) extinction law. Stellar absorption was taken into account using SINOPSIS to estimate the contribution from the stellar component, which was then subtracted from each spaxel. The sample of unwinding galaxies, i.e. galaxies which exhibit visual evidence of unwinding spiral arms, was selected from the full GASP catalog of 114 galaxies by visual inspection of the whitelight images along with the Hα maps created using KUBEVIZ as detailed in Bellhouse et al. (2017). The visual selection was carried out with the aim of singling out objects

Table 4.1: Properties of GASP jellyfish galaxies with unwinding spiral arms. Projected ICM orientation is estimated according to the location of the galaxy in position-phase space

Galaxy	Cluster	RA_{galaxy}	DEC_{galaxy}	$M_{*,disk}$ ($10^{10} M_{\odot}$)	Inclination	Projected ICM Orientation (from PPS)
JO201	A85	010.3762293	-09.2627726	6.2 ± 0.8	41.4°	Face-on
JO93	A2593	350.7988503	+14.9018617	3.5 ± 0.5	25.0°	Face-on
JO194	A4059	359.2530820	-34.6805380	15.0 ± 3	38.3°	Face-on
JO200	A85	010.5209131	-09.5344629	7 ± 1	45.3°	Edge-on
JO175	A3716	312.8233030	-52.8228720	3.2 ± 0.5	43.2°	Edge-on
JO47	A168	018.9906626	+00.6933548	0.40 ± 0.06	44.7°	Edge-on
JO49	A168	018.6830168	+00.2861296	4.8 ± 0.6	53.6°	Edge-on
JO70	A2399	329.0170813	-07.3272804	2.9 ± 0.6	39.3°	Edge-on
JO69	A2399	329.3303782	-07.7789347	0.8 ± 0.2	43.3°	Edge-on
JO73	A2415	331.1082488	-05.2463570	1.1 ± 0.3	33.1°	Edge-on
JO85	A2589	351.1308813	+16.8683152	4.6 ± 0.9	24.9°	Face-on
JW39	A1668	196.0321635	+19.2106686	17 ± 3	52.5°	Edge-on

with the following characteristics:

1. Disk morphology (excluding mergers, rings, irregular galaxies etc)

2. Orientation close to face-on, (axial ratio ≈ 1). This criteria ensures that the state of the spiral arms can be clearly inspected, which is not the case in edge on galaxies.

3. Clear signatures of broadened spiral arms, as judged from visual inspection of the Halpha maps and whitelight images

The resulting sample consists of 13 face-on galaxies with clear spiral arms, of which 12 had signs of unwinding spiral arms. The fact that 12 out of 13 face-on spiral galaxies in the GASP sample show signs of unwinding is indicative that the effect may be prevalent in stripped galaxies. The one galaxy inclined face-on to the observer not showing the unwinding effect is galaxy JO128 which is located towards its cluster outskirts and belongs to the control sample of non-stripped galaxies given in Vulcani et al. (2018) due to the low star formation measured in the galaxy's tails. The final sample is listed in Table 4.1 and shown in Figure 4.1.

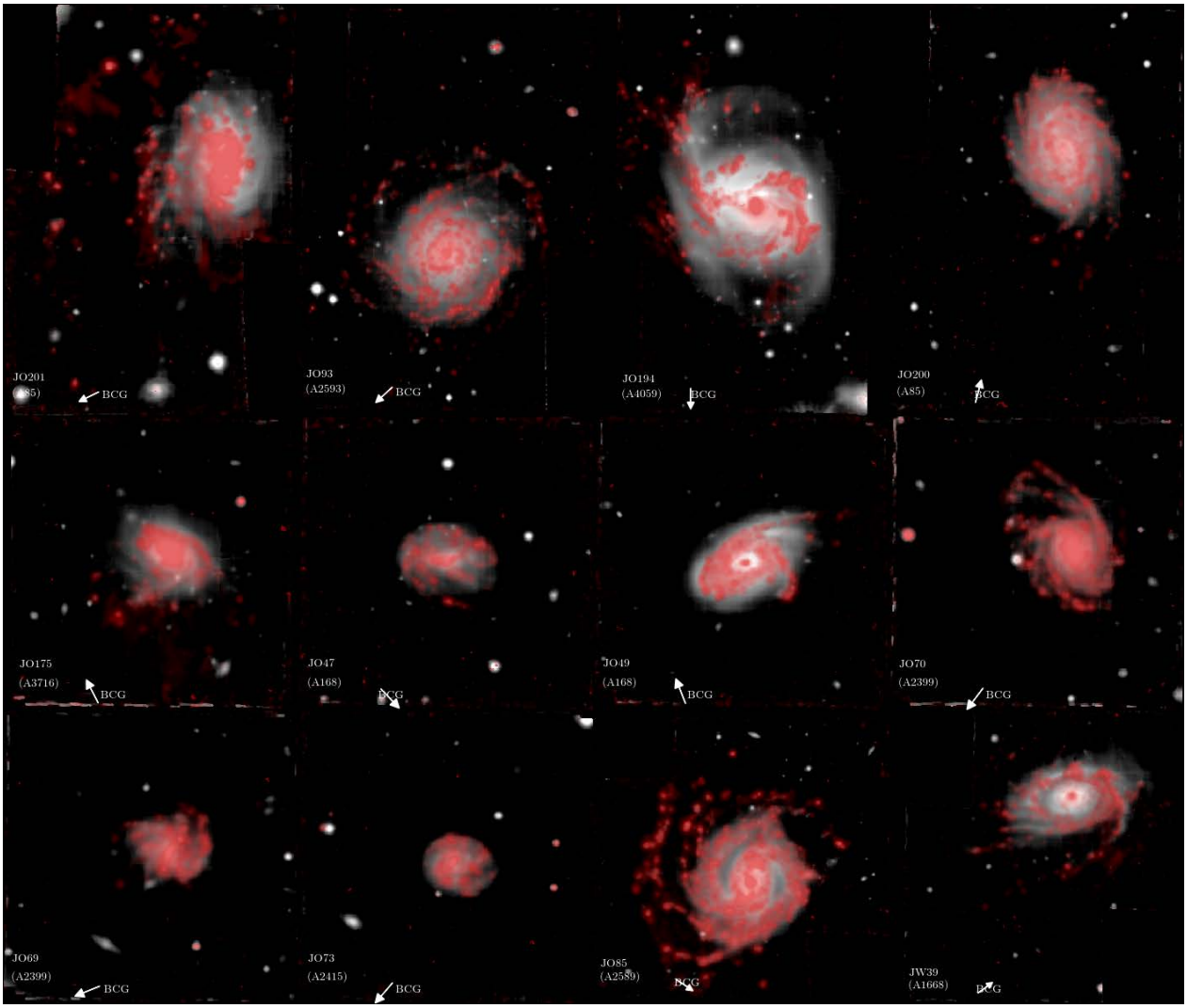

Figure 4.1: The unwinding galaxy sample, showing whitelight images of each galaxy with the Halpha emission line flux overlaid in red. The figure shows the red Halpha tails extending far beyond the disks in some cases, whilst maintaining a clear spiral arm pattern. The white light images generally show little to no unwinding pattern, which is expected to only manifest itself in the stripped gas and young stellar population.

4.2.1 Morphologies

As Figure 4.1 shows, the effect of unwinding spiral arms is most visible in Ha (not in the stellar light). Notable examples of unwinding spiral arms include JO201, which in the Hα map shows an extremely extended arc of stripped material to the left of the galaxy in Figure 4.1, far outside the galaxy disk. JO200 shows a generally uniform spiral morphology, with three spiral arms extending below the disk in the image. While some galaxies exhibit asymmetric unwinding patterns in a distinct tail, JO85 and JO93 show an unwinding pattern most of the way around the disk. It is possible that the azimuthal extent of the unwinding feature around the galaxy disk may be proportional to the inclination of the galaxy with respect to the ICM, i.e. tighter tails are observed in galaxies moving edge-on into the wind, which unwind only on their trailing edges, whereas broader unwinding tails may indicate face-on stripped galaxies, whose tails originate from further around the disk.

4.2.2 Kinematics

Figures 4.2 and 4.3 compare the ionised gas kinematics on the left panels with the stellar velocities on the right. The gas velocities were measured using the Hα emission line kinematics, which were measured using KUBEVIZ (Fumagalli et al., 2014) from the position of the Hα line in each spaxel.

The stellar velocities were calculated using the absorption line kinematics measured with the *ppxf* code (Cappellari & Emsellem, 2004) as described in Poggianti et al. (2017b). The stellar velocities in both figures are much smoother and show mostly undisturbed rotation curves. In the case of JO200, the gas velocities are similar to the stellar velocities, with some differences in the central gradient. In the ionised gas of JO201, the kinematics are very deviated from the stellar disk. Whilst the stellar disk velocity contours follow more of a "U" shape at the upper and lower edges of the disk, the gas kinematics follow concentric contours outward from the upper edge of the disk. This is likely to result from JO201's mostly face-on interaction with the ICM, pushing the gas around the edges of the disk to higher line-of-sight velocities.

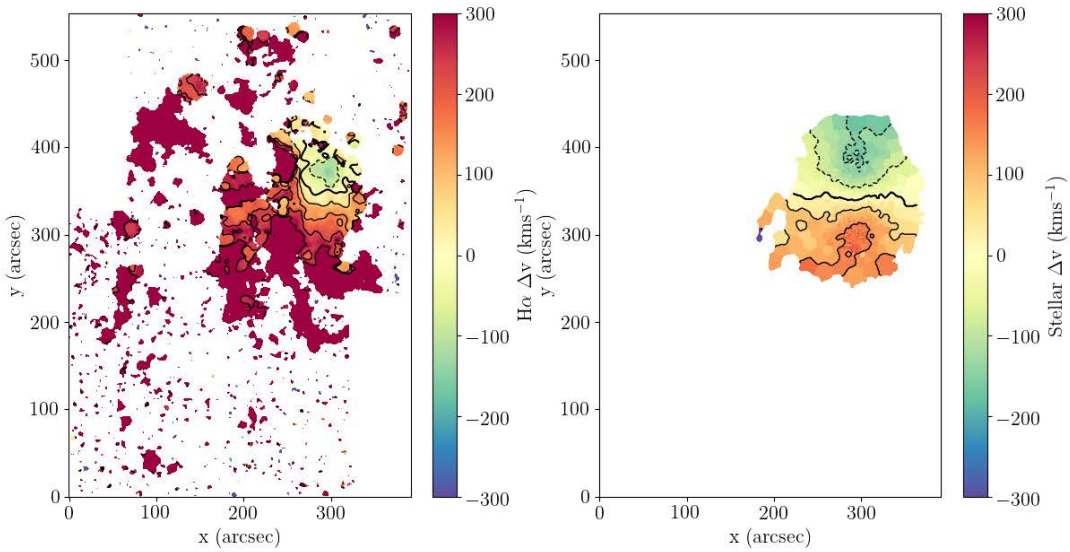

Figure 4.2: Comparison of kinematics maps in JO201. Black lines indicate velocity contours on the corresponding maps. *Left:* ionised gas velocity map measured from emission line kinematics. *Right:* stellar velocity map measured using ppxf. The stellar velocity contours exhibit a "U" shaped pattern at the upper and lower edges of the disk, in contrast, the gas kinematics follow concentric contours outward from the upper edge of the disk.

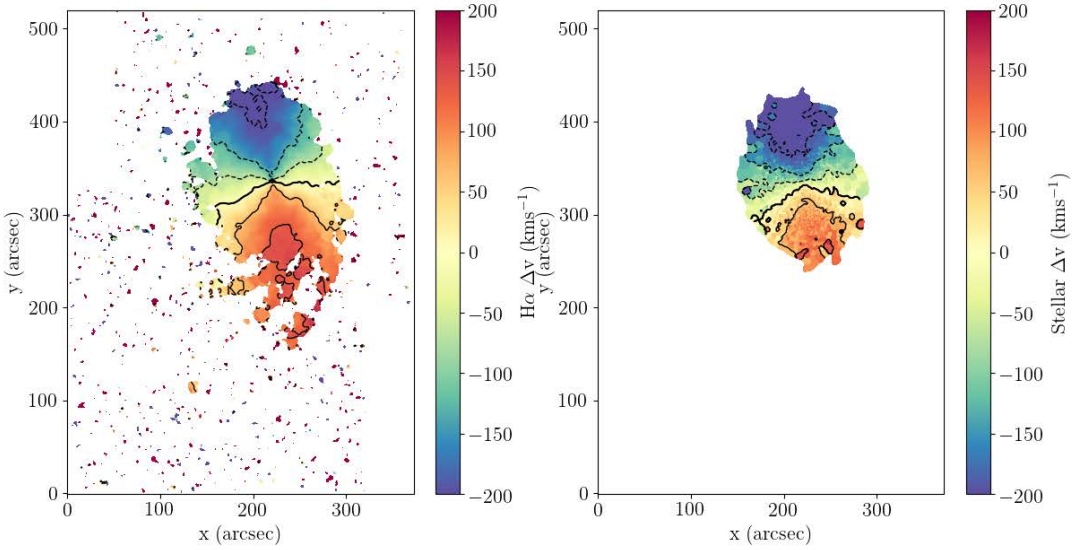

Figure 4.3: Comparison of kinematics maps in JO200. Black lines indicate velocity contours on the corresponding maps. *Left:* ionised gas velocity map measured from emission line kinematics. *Right:* stellar velocity map measured using ppxf. The stellar and gas velocities are similar in general, with some differences in the central gradient

4.3 Galaxy orbits

In order to explore the orbits and the inclination angles between the galaxies and the ICM, we looked at the morphologies of galaxies and their positions in phase space.

The location of the sample of unwinding galaxies in projected position vs. velocity phase-space is a useful parameter in this analysis, as this diagram can reveal the natures of the orbits that the galaxies are on (see Jaffé et al., 2018). Figure 4.4 shows the distribution of the unwinding-spiral jellyfish sample compared with the overall population of galaxies in clusters. The galaxies have been plotted as thumbnail images centred on their corresponding locations in phase space. For each galaxy, the Hα map is plotted in red over the whitelight image. The thumbnail images have been rotated such that the BCG direction is always to the left, parallel to the x-axis. The sample of all omegaWINGS galaxies is shown in the background as white points and the solid white lines indicate escape velocity curves in a NFW profile as in Jaffé et al. (2018).

Almost all the galaxies in our sample have negative peculiar velocities which indicate they are moving towards the observer. In particular, there are several galaxies (most notably JO201, JO194 and JO85) occupying the lower envelope of the trumpet-shape distribution of galaxies in phase-space close to the cluster centre, which is an indication that they could be crossing the dense core of the ICM at high speeds on radial orbits along our line of sight for the first time (see Bellhouse et al., 2017; Jaffé et al., 2018). Only one galaxy has a comparatively high positive velocity at a similar clustercentric distance (JW39), which indicates it is moving away from the observer.

According to the phase space diagram shown in Figure 4.4, the unwinding sample does not occupy a single, specific region of phase space. However, the more asymmetrically unwinding galaxies are generally found at low LOS velocities and higher projected radii, where it is likely that the majority of their motion is along the plane of the sky. Coupled with their orientation face-on to the observer, this would be consistent with these galaxies being stripped edge-on to the ICM.

Out of the sample of 12 unwinding galaxies, we find that 4 galaxies, JO201, JO93, JO194 and JO85 appear to be falling face-on with respect to the ICM, whilst the other 8 galaxies are likely to be traveling edge-on based on their phase-space positions (generally galaxies with $v/\sigma > 1.5$) and morphologies.

The thumbnail images in the diagram give an indication of the tail directions of each of the unwinding

galaxies with respect to the cluster centre. Galaxies to the middle right of the figure, which are at higher clustercentric radii and lower LOS velocities, tend to exhibit more extended, asymmetric tails. Based on their position in phase space, these galaxies are also the ones more likely to be undergoing edge-on stripping, as most of their motion is likely to be across the plane of the sky.

The more central, higher LOS velocity galaxies to the left of the figure tend to have shorter tails, which in some cases are more symmetrically unwinding. These galaxies are more likely to be experiencing face-on stripping, as most of their motion is likely to be along the line-of-sight.

4.4 Spiral Arms

4.4.1 Identifying spiral structure

In order to analyse the extent of the unwinding spiral arm patterns in the galaxy sample, we produced maps of the Hα and 12+Log(O/H) metallcities, reprojected onto polar space in terms of radial distance from the centre of the galaxy vs azimuthal angle around the disk.

The Hα and heavy element abundances trace the distribution of the spiral arms in the galaxy disk (Vogt et al., 2017). The Ha traces the distribution of the star formation activity which is increased in the denser regions of gas and dust of the spiral pattern. The metallicity has been found by Ho et al. (2017) to vary azimuthally with the spiral arm pattern due to local oxygen enrichment as a result of spiral-driven mixing.

The Hα maps were taken directly from the KUBEVIZ fits, while the 12+Log(O/H) metallicities were calculated using *pyqz* (Dopita et al., 2013).

In order to carry out the reprojection, each galaxy was corrected for inclination by scaling the distances along the dimension of the kinematic minor axis according to the axial ratio. The axial ratios were measured by taking the mean value from a series of elliptical isophotes fitted to the i-band image (see Franchetto et al. in prep. for details). Each spaxel was then reprojected onto polar coordinate space according to its radial distance and azimuthal position. The reprojection was carried out by calculating the position of each corner of each spaxel and transforming into the reprojected polar space, in order to preserve the extent of each spaxel in the new space, particularly in regions close to the galaxy centre where individual spaxels cover a large range of azimuthal angles. The resulting figures shown in Fig 4.5 and 4.6 show the disk of the galaxy

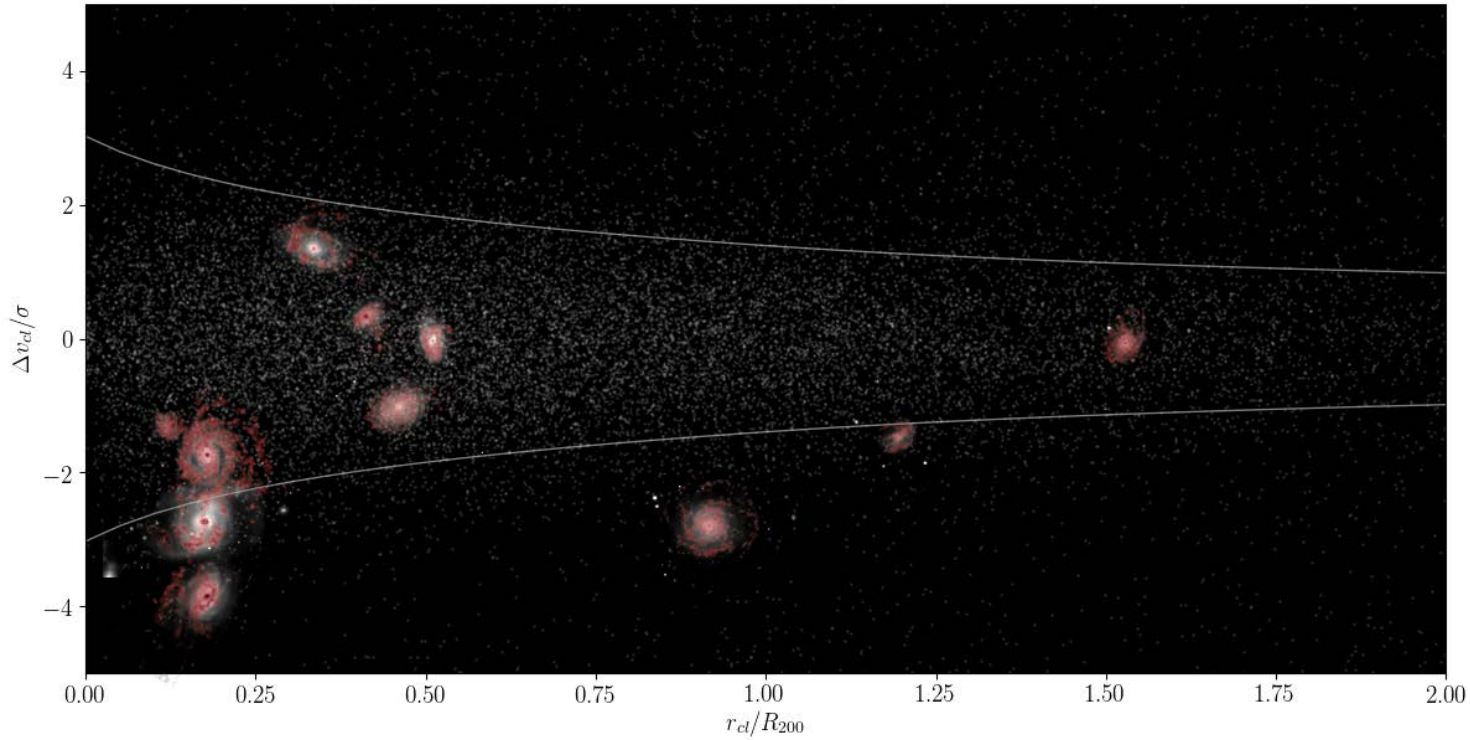

Figure 4.4: Projected position vs. velocity phase-space diagram of the unwinding sample, showing thumbnail images of each galaxy (Colours as in Figure 4.1). Each thumbnail is rotated so that the BCG direction is to the left. White points show as comparison, the sample of all omegaWINGS cluster galaxies and white solid lines indicate escape velocity curves in a NFW halo as in Jaffé et al. (2018).

Table 4.2: Comparison of pitch angles in the disks and tails of unwinding GASP jellyfish galaxies. Values marked as ? are given where no clear spiral arms are visible.

Galaxy	$\alpha_{\rm disk}(^\circ)$	$\alpha_{\rm tails}(^\circ)$
JO201	?	17.2
JO93	11	15
JO194	14.2	35.6
JO200	26.7	36.1
JO175	18.4	63.3
JO47	?	?
JO49	?	43
JO70	16.3	31.6
JO69	?	30.0
JO73	?	?
JO85	21.8	27.4
JW39	17.0	36.9

"unwrapped" in the left panel, alongside the original galaxy on the right. Spiral arms in the galaxy appear as lines and curves on the left hand side, with the gradient of the lines indicating the pitch angle. Straight lines were then drawn over the spiral arms on the azimuthal figure by hand, and the reverse projection method was used to show these on the original galaxy to highlight the arm locations and pitch angles.

Examples are shown for galaxies JO201 and JO200, which exhibit clear spiral arms in the azimuthal figure. In the tail of JO201, the inner spiral arm has a pitch angle around 7.7°, whilst in the outer spiral arm the pitch angle increases to 17.2°. In the case of JO200, the spiral arms have pitch angle values around 26.7° in the disk, which increase to around 36.1° in the unwound tails.

The azimuthal plots of other galaxies, not shown, have typical disk and tail spiral arm pitch angles shown in Table 4.2.

4.4.2 Gradients in stellar ages

In order to understand the process behind the apparent unwinding, we constrained the spatial distribution of the stellar component, divided into bins of stellar age calculated using the SINOPSIS spectrophotometric fitting code (c.f. Fritz et al., 2017). SINOPSIS finds the best fitting combination of single stellar population spectra to the spectrum of each spaxel, including the pertinent emission lines, in order to estimate the contributions of stellar populations in four age bins 1) 5.7×10^9-1.4×10^{10}yr, 2) 5.7×10^8-5.7×10^9yr, 3) 2×10^7-5.7×10^8yr

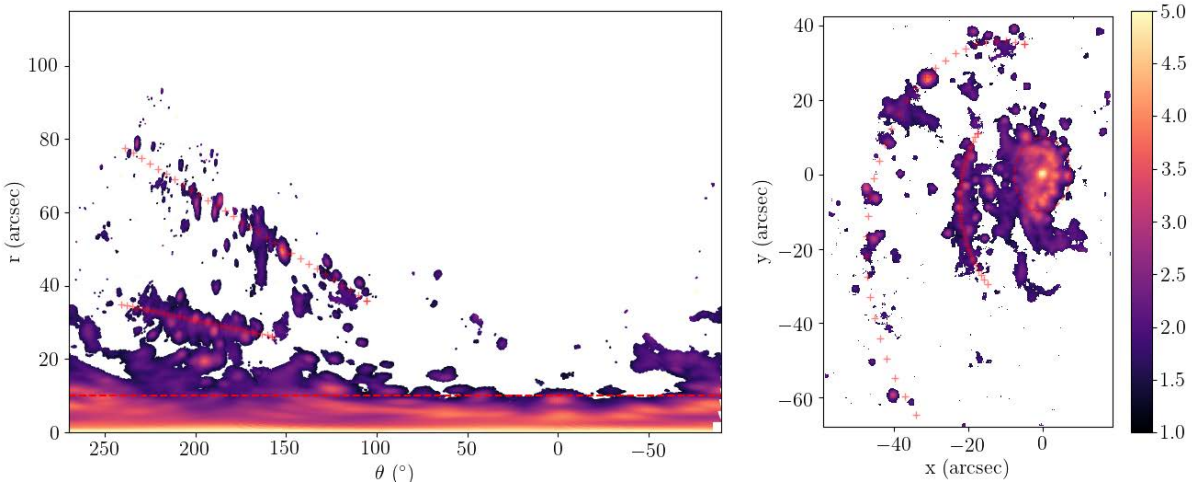

Figure 4.5: Plot of metallicity for the "unwrapped" disk of JO201, showing radial projected distance from the centre against azimuthal angle.

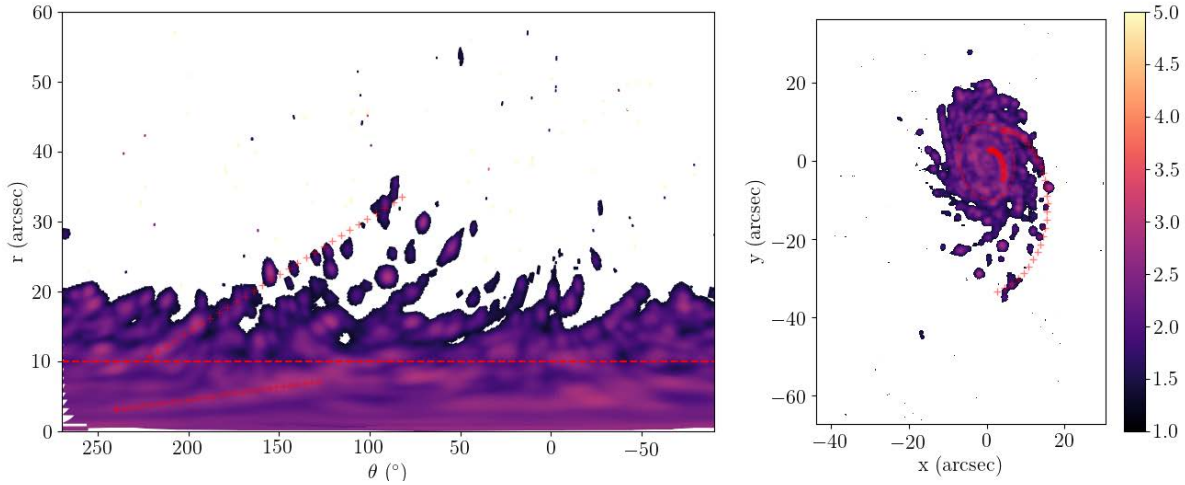

Figure 4.6: Plot of metallicity for the "unwrapped" disk of JO200, showing radial projected distance from the centre against azimuthal angle.

and 4) $< 2 \times 10^7$yr to the observed light. The number of bins and their range are defined in SINOPSIS to minimise uncertainty in the measured stellar ages, based on simulations performed in Fritz et al. (2007).

Figure 4.7 shows the whitelight images of each galaxy, overlaid with the oldest stellar component (5.7×10^9-1.4×10^{10}) in red and the youngest ($< 2 \times 10^7$yr) in blue. The image reveals that, as expected for the older stellar component, the red contour lies solely within each galaxy and appears undisturbed by the stripping. In contrast, the blue contours which trace the newly formed stars reflect the pattern of the unwinding spiral arms and extend much further outside the galaxy disk. This shows that the stars form out of the spiral arms after they have been stripped and unwound from the galaxy; the newly-formed stars will be unaffected by subsequent stripping.

Highlighting this latter point in greater detail, Figures 4.8 and 4.9 show the most drastic examples of spatial offsets between stellar age bins within the unwinding tails. In both figures, red shows the oldest stellar population (5.7×10^9-1.4×10^{10}yr), followed by orange (5.7×10^8-5.7×10^9yr), green (2×10^7-5.7×10^8yr) and blue showing the youngest ($< 2 \times 10^7$yr). In the upper left of JO194, the green and blue contours show a distinct spatial offset of around 4.6kpc, which traces the motion of the unwinding arm. The green contour of stars which formed around 285Myr earlier, is more tightly wound with the disk of the galaxy, whilst the blue contour lies further extended from the disk. A similar occurrence is visible in JO85 with the lower spiral arm of the image. This pattern captures the process of the spiral arm opening out and leaving a trail of newly-formed stars in its wake.

4.5 Simulations

We compare the observed morphology and velocity field of our sample to a set of high resolution wind-tunnel simulations of an intermediate mass spiral galaxy undergoing ram pressure stripping. The simulations consider three fixed inclination angles for the direction of the ram pressure wind with respect to the plane of the model's disk; face-on, 45°, and edge-on. In this way. we hope to better understand the role of inclination on the velocity field of the gas, and the effectiveness with which the spiral arms are unwound and the pattern of unwinding.

The model spiral galaxy we use has three main components of mass - an NFW dark matter halo, expo-

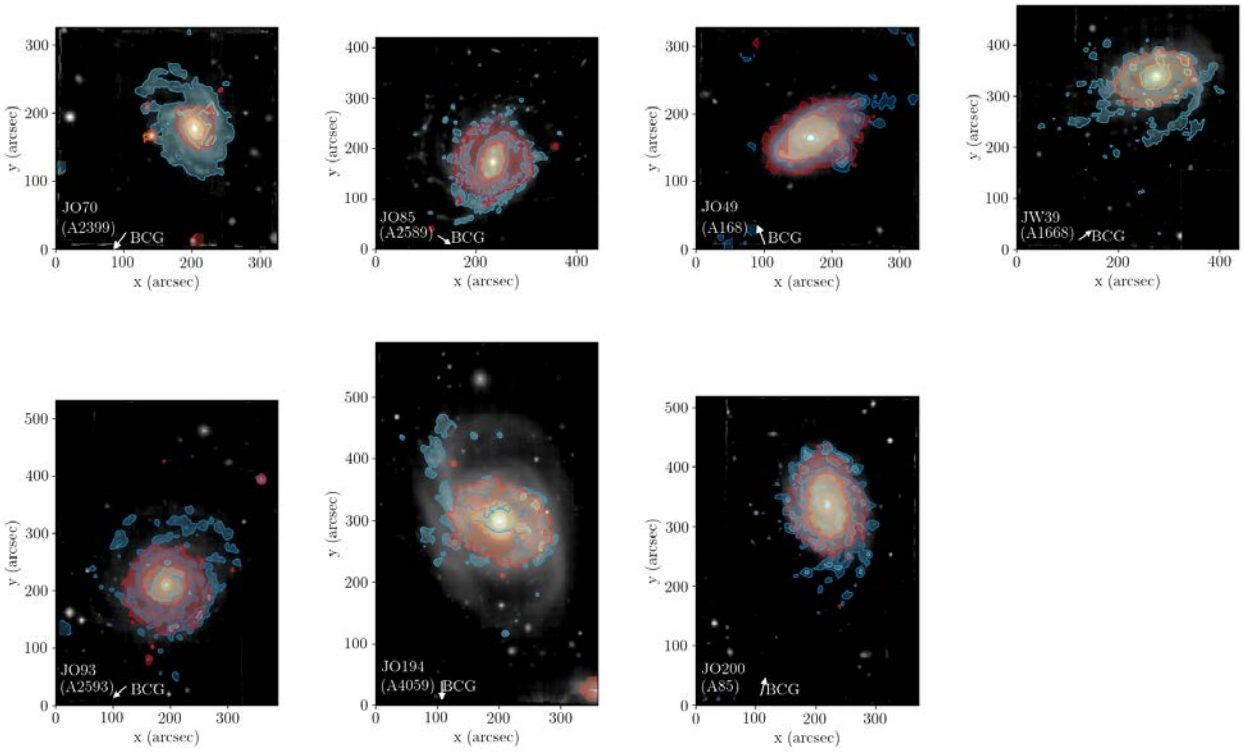

Figure 4.7: Unwinding galaxies shown in white light, overlaid with contours showing the oldest 5.7×10^9-1.4×10^{10}yr (red) and youngest $< 2 \times 10^7$ (blue) stellar populations calculated using SINOPSIS spectrophotometric code. The figures show that the older stellar population is generally constrained to the disk of the galaxy and is fairly undisturbed, whilst the younger population of stars extends much further into the tails and describes the extended spiral structure in the unwound arms.

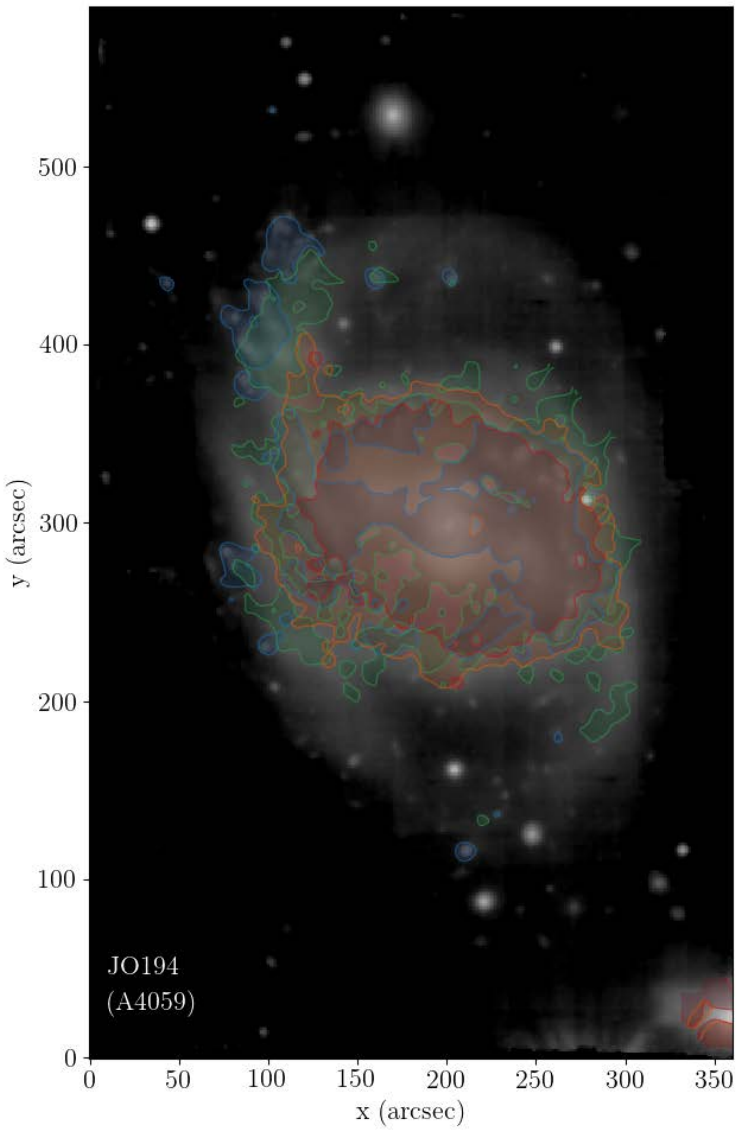

Figure 4.8: JO194 shown in white light, overlaid with four stellar age bins. Red: 5.7×10^9-1.4×10^{10}yr, orange: 5.7×10^8-5.7×10^9yr, green: 2×10^7-5.7×10^8yr and blue: $< 2 \times 10^7$yr. The upper left arm shows that the youngest (blue) stellar population is much further unwound from the galaxy than the green stellar age bin, indicating that the stars form out of the unwinding gas cloud and remain in the position in which they formed. As the arm unwinds, it has left behind a trail of newly formed stars in its wake.

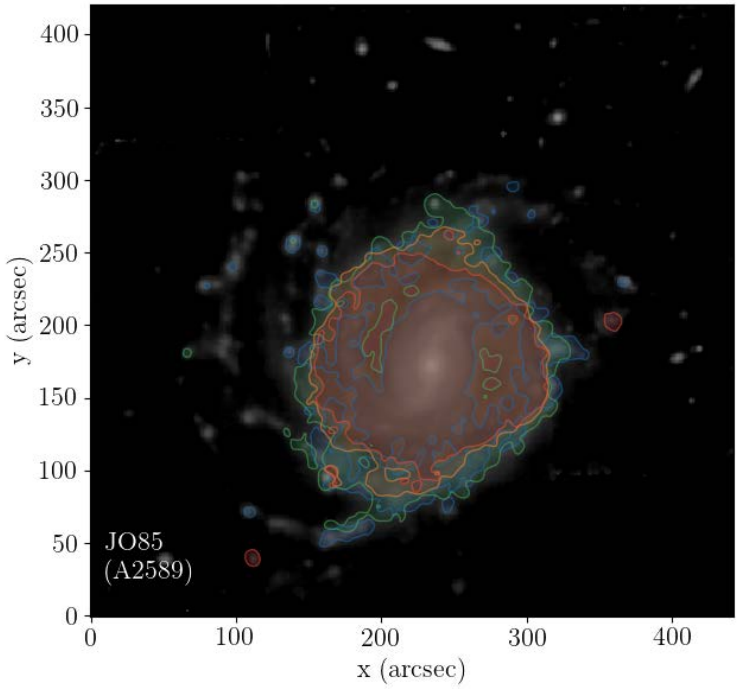

Figure 4.9: JO85 shown in white light, overlaid with four stellar population bins as described in Figure 4.8. The lower spiral arm shows a similar spatial offset to JO194 between the two youngest stellar populations revealing the unwinding motion of the spiral arm as it leaves a trail of newly formed stars.

nential disk of stars, and exponential disk of gas. Our model galaxy does not contain a bulge component. The dark matter halo mass of the galaxy is $M_{total} = 3.2 \times 10^{11} M_{\odot}$, with a virial radius of 140 kpc, and halo concentration=12, consisting of 5 million dark matter particles. The stellar disk has a total mass of $M_{*} = 1 \times 10^{10} M_{\odot}$, with an radial exponential scalelength of 2.2 kpc, truncated at 4 scalelengths, initially consisting of 250 thousand star particles. The gas disk initially has a total mass of $M_{gas} = 1.3 \times 10^{9} M_{\odot}$, and a radial scalelength of 3.7 kpc, truncated at 4 scalelengths, and is assumed solar metallicity. Initial conditions were built using the publically available initial-conditions set-up code DICE (Perret et al., 2014). Tests demonstrate that the initial conditions were very stable, and were evolved for 0.5 Gyr in isolation to ensure dynamical stability had been reached.

Simulations were carried out with the Adaptive Mesh Refinement (AMR) code RAMSES (Teyssier, 2002). The total volume was a box with side-length of 280 kpc, that fully encloses the virial radius of the dark matter halo. The adaptive mesh was allowed to refine according to the mass within a cell to a maximum refinement level=14, equivalent to a smallest cell-size of 17 pc. In addition, the refinement level ensures that at least four Jeans-lengths are resolved, down the to maximum level of refinement. The simulation considers a radiative-cooling treatment for solar metallicity gas. Star formation occurs following a standard prescription of a Schmidt-law with a 3% star-formation efficiency for all gas above a critical density threshold of $0.1 \mathrm{cm}^{-3}$. These are typical parameters for simulations conducted with RAMSES, which give a reasonable SFR for a galaxy of this mass as well as a reasonable match to the Kennicutt-Schmidt relation. Supernova feedback is treated thermally, with an efficiency of 20%, and a yield of 0.1. We confirm that, in isolation, our model disk lies on the star-forming main sequence.

Ram pressure was modelled using a wind-tunnel simulation set-up. A hot, fast flowing, low density, intracluster medium gas is fed into the simulation box from one wall of the simulation box. We initialise the disk with a low constant wind to roughly imitate the out skirts of the cluster. Then, after reaching 1 Mpc from the cluster centre, the density and inflow velocity of the intracluster medium begins to smoothly evolve with time, to mimic the changing ram pressure that a cluster spiral might experience when falling into a real cluster. To calculate the time evolving density, we assume a beta model for the intracluster medium that is a rough approximation for the Virgo cluster (central density=2.0×10^{-26} g cm^{-3}, $\beta = 0.5$, core radius=50 kpc). To calculate the time evolving wind speed, we calculate the orbital velocity of a galaxy

moving through the cluster potential well, and assume the inflow speed matches the orbital velocity. Under the assumption of hydro-static equilibrium with a gas temperature of 4.7×10^7 K, the potential well of the cluster is fully defined. Using a simple time-step integrator, we trace out the orbit of a galaxy falling in from 1 Mpc. We assume the particle has an initial radial velocity component of 565 km s^{-1}, and a tangential velocity component of 565 km s^{-1}. This results in a quite plunging orbit reaching a pericentre distance of 340 kpc from the cluster centre. During the infall, the orbital velocity increases from 800 km s^{-1} and reaches a maximum velocity of $\sim$1600 km s^{-1} at pericentre, and we set the inflow speed of the gas in our wind-tunnel test as equal to the orbital velocity.

We consider three inclination angles of the ram pressure wind to the disk plane; edge-on, 45° inclined, and face-on. For each inclination angle, we conduct the simulation for at least 2.3 Gyr in total. This is sufficient to pass the cluster pericentre, which occurs after approximately 1.7 Gyr. However, for this study, we find that the heavily truncated gas disks of those disks that have passed pericentre do not show features resembling the unwrapping we see in our observational sample. Therefore, we restrict our attention to the period between when the model disks enter the cluster and just before they reach pericentre.

Now we create "observed" velocity maps of the simulated disks at various instants in time, as they approach the cluster pericentre for the first time. We consider instants when the galaxy is at a clustocentric radius of $r_{\rm cl}$=0.92 Mpc (in the cluster outskirts), 0.66 Mpc (intermediate radius), and 0.35 Mpc (just before pericentre). Now at each of these instants we make a map, by binning the gas properties along a given line of sight, considering similar resolution as in the MUSE observations. We produce maps for all three disk inclinations. As we are comparing to H_α emission-line maps, we only consider gas above the star formation threshold in the simulation (i.e., with density $> 0.1{\rm cm}^{-3}$) in our maps. Velocity maps were then made by measuring the average velocity along each bin for comparison with observations.

JO200 was selected as a suitable galaxy for comparison with the simulation models, given the clarity of its disk and spiral arms and its strongly-asymmetric unwinding. As we will now demonstrate by comparison with the models, this strongly suggests edge-on infall with respect to the ICM wind.

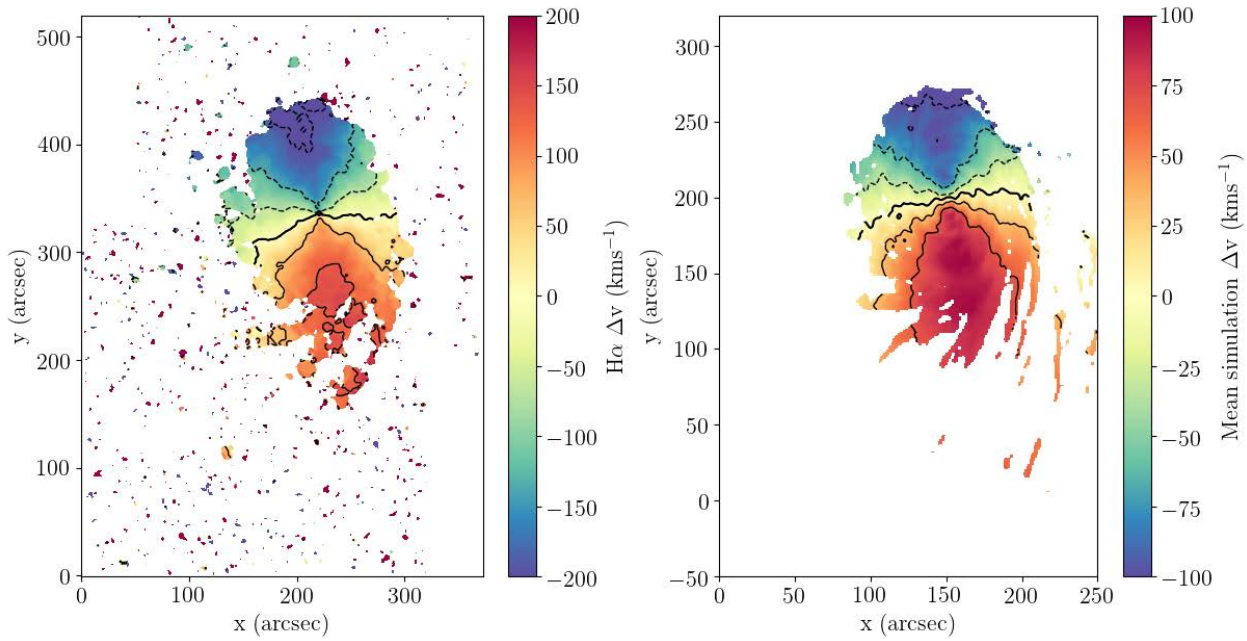

Figure 4.10: *Left:* Kinematics map of JO200 measured using Hα emission line velocities from KUBEVIZ. *Right:* Kinematics map of "observed" simulated galaxy undergoing edge-on stripping, produced as described in section 4.5.1. The simulated unwinding galaxy is rotated to match the inclination and position angle of JO200, and matches the unwinding pattern and kinematics fairly well, suggesting that JO200 is well-described by an edge-on stripping scenario.

4.5.1 Comparing Observations with Simulations

The compared velocity fields of JO200 and the edge-on simulated galaxy are shown in Figure 4.10. For ease of comparison between the two, the simulated galaxy was rotated to match the inclination and position angle of JO200 prior to measuring and averaging the particle velocities along the lines of sight of each pixel "bin".

Whilst the absolute values of the rotation curve differ as a result of the different total masses of the real and simulated galaxies, the gradient of the rotation is very similar in both cases. It is apparent from the figure that the velocity contours in the observed galaxy are more "U"-shaped at the most extreme ends of the rotation curve, while the simulated galaxy exhibits a more uniform rotation.

The spiral arms in both galaxies show a similar amount of unwinding with similar pitch angles in the unwound tails at the lower edge of the galaxies. The resemblance suggests that the unwinding pattern of JO200 may be well described by a nearly edge-on stripping scenario.

4.5.2 Tracing Unwinding Throughout Infall

We further studied the mechanisms behind the process of unwinding by analysing the kinematics and shape of the simulated galaxy over several timesteps throughout the infall process. A snapshot of the galaxy simulation falling edge-on with respect to the ICM wind was taken prior to infall and snapshots were taken of the edge-on and face-on galaxies during three stages throughout the infall process. These snapshots were binned to a grid of pixels at a similar resolution to the observations and analysed in two orientations: 1) The inclination angle is perpendicular to the wind direction, i.e., the galaxy is falling partially along the line of sight, and 2) The inclination angle is parallel to the wind direction, i.e., the galaxy is falling across the plane of the sky. The snapshots of the perpendicular and parallel cases are shown in figures 4.11 and 4.12 respectively.

In the perpendicular case, figure 4.11, it can be seen that the gas on the advancing edge of the galaxy, the right hand edge in the figure, is slowed by the ram-pressure as it rotates into the wind. The wind acts to slow the gas, causing it to build up as well as fall to higher orbits, producing a large asymmetry in the second timestep. As the simulation progresses, the stripped gas falls further behind the galaxy and the tail becomes more symmetric. In the final timestep, after the outer layers of gas have been removed, the remaining object is left with a very steep rotation curve gradient.

In the parallel case, figure 4.12, a similar asymmetry is observed in the shape of the disk in the second timestep, arising from the gas being slowed by the ICM wind, causing it to fall to higher orbits. This asymmetry shortly vanishes and the tail becomes more collimated by the final timestep. The rotation curves show the velocity curve being "dragged" along the wind direction to the left and the extreme values of the rotation curve decrease over time. As with the perpendicular case, the velocities in the central region are mostly unaffected and the remaining object retains a steep rotation curve.

Figure 4.13 shows the case of the face-on infalling simulated galaxy in 3 timesteps starting from initial infall. The ICM wind direction is downward and slightly inclined away from the observer. The velocity curve of the galaxy shows a disturbed but still fairly symmetric rotation in the initial timestep, with a slight deflection at the edges to higher velocities, similar to that observed in JO201 (c.f. Figure 15 within Bellhouse et al., 2017). In the second timestep, more of the gas has been pushed to higher velocities and the central

rotation curve is noticeably disturbed. By the third timestep, most of the gas has been stripped to higher velocities and the remaining object retains a steep rotation curve.

These simulations highlight three examples of the effects of orientation of an infalling galaxy with respect to both the ICM wind and the observer, revealing the differences in the effect of face-on and edge-on stripping on the velocity profile. In edge-on stripping scenarios, the differential velocities between the edge of the edges of the galaxy rotating into and out of the wind appears to result in a difference in the effectiveness of stripping, such that the gas rotating with the wind direction is more readily stripped, whilst the gas rotating against the wind is slowed initially, causing an asymmetric build-up of material on the corresponding trailing side.

In the face-on stripping scenario, the gas is stripped around the edges of the disk, causing the rotation curve across all areas of the disk to be much more disturbed, upward deflections on either side of the rotation curve indicate that the stripping occurs more evenly around the disk, in comparison to the edge-on scenario. The resulting galaxy after the face-on stripping has a shorter, steeper rotation curve, which is likely to be due to the increased effectiveness of face-on stripping (Abadi et al., 1999; Quilis et al., 2000; Vollmer et al., 2001) removing gas from the disk down to a smaller truncation radius. The differences between the velocity maps in these scenarios suggest that the kinematics can be a probe of the inclination of a galaxy's stripped gas with respect to the ICM.

4.6 Discussion

We find that a pattern of unwinding spiral arms is visible in 12 face-on galaxies in the GASP sample which are undergoing ram-pressure stripping interactions during cluster infall. These observations confirm that unwinding spiral arms can be the result of ram-pressure stripping; moreover, the pattern can differ depending on the inclination of the galaxy relative to the wind. The unwinding effect is visible in 12 out of the 13 face-on galaxies with visible spiral arms, making this effect much more common than previously expected. The unwinding pattern is visible in the stripped gas of a galaxy, the original smooth rotation curve of the stellar disk is unaffected. The two effects which can, individually and in combination, give rise to an unwinding pattern are as follows. 1) In edge-on wind interaction cases, the differential ram-pressure in the leading and trailing edges of the disk causes a build-up of material in the leading edge. The tail becomes asymmetric

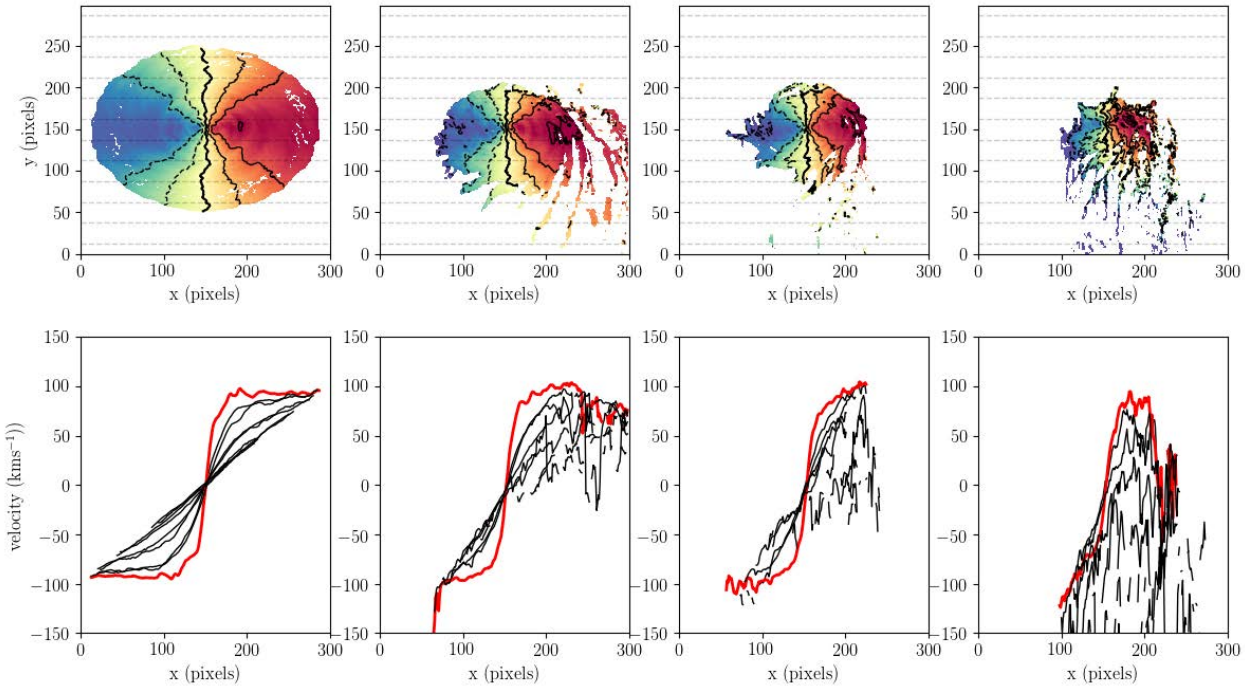

Figure 4.11: Timestep snapshots of a simulated galaxy undergoing edge-on stripping, inclined such that the velocity map can be extracted to emulate a physical observation. In this example, the inclination axis is perpendicular to the wind direction, such that the motion of the galaxy is partially along the line-of-sight. The red line shows the central rotation curve, whilst the black lines show the rotation curves across the disk of the galaxy, corresponding to the dashed lines on the upper panels.

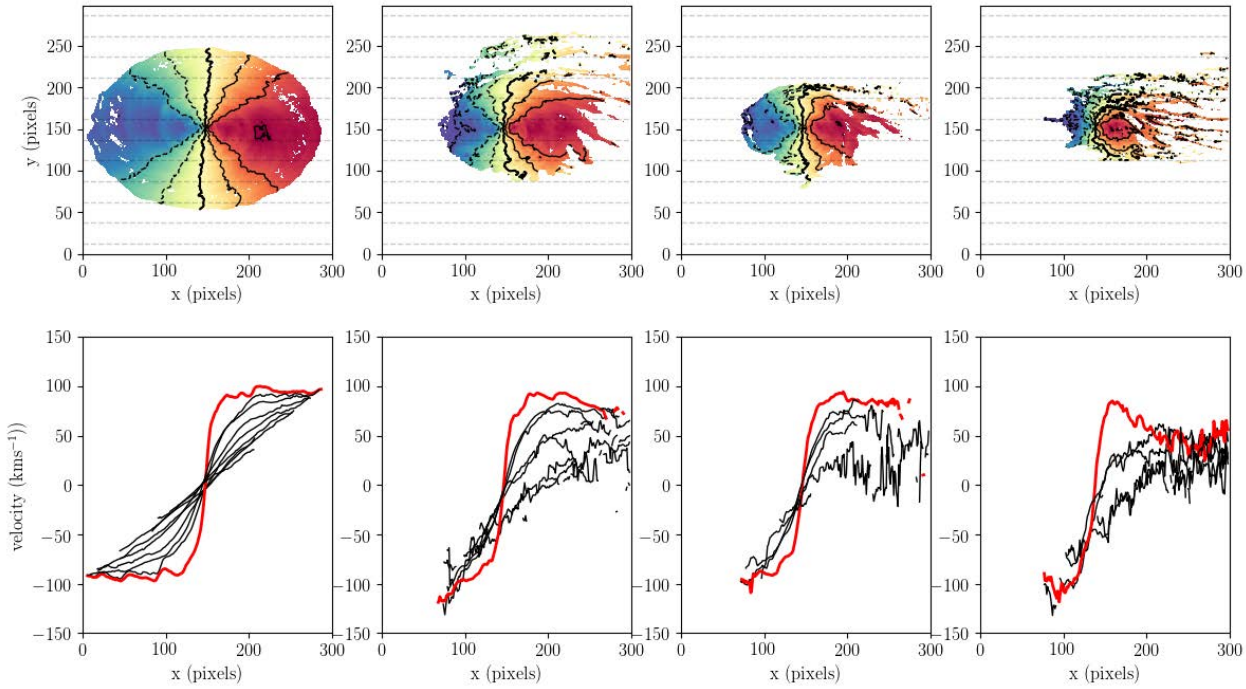

Figure 4.12: Timestep snapshots of a simulated galaxy undergoing edge-on stripping, inclined such that the velocity map can be extracted to emulate a physical observation as for Figure 4.11. In this case, the wind direction is parallel to the inclination axis, i.e., the motion of the galaxy is entirely across the plane of the sky. The red line shows the central rotation curve, whilst the black lines show the rotation curves across the disk of the galaxy, corresponding to the dashed lines on the upper panels.

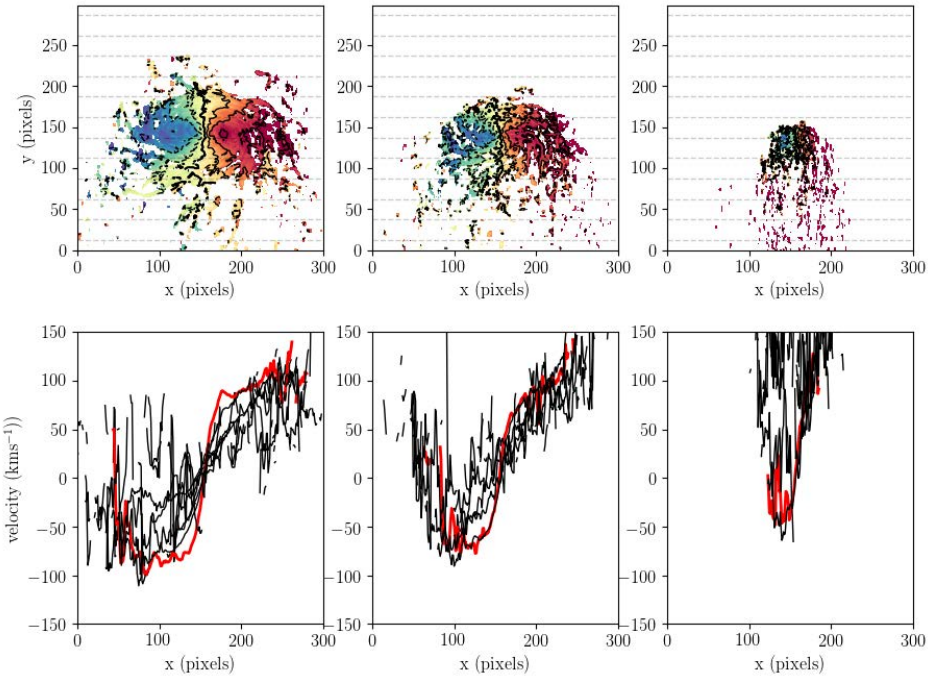

Figure 4.13: Face-on stripped galaxy. The red line shows the central rotation curve, whilst the black lines show the rotation curves across the disk of the galaxy, corresponding to the dashed lines on the upper panels.

and the slowed rotation of the gas causes the pitch angle to increase. 2) In face-on wind interactions, the gas from the outer spiral arms is stripped and withdrawn from the potential well of the galaxy disk, causing it to move more tangentially and increase the pitch angle in all directions from the disk. In most cases, a combination of these two effects will occur as a galaxy is stripped at angles between face-on and edge-on with respect to the ICM wind. Cases in which the galaxy is moving mostly edge-on to the wind appear to be more asymmetric and have tails that are further collimated to one side of the disk, whilst cases closer to face-on such as JO201 and JO85 show gas extending in a much wider range of directions from the disk. The unwinding tails were found to contain only stars younger than 20 Myr when analysed with SINOPSIS spectrophotometric fitting code which have likely formed in-situ, confirming that the unwinding effect only occurs in the gas component of the galaxy.

The results of the simulations and the observed differences between patterns in the tails in different regions of phase space suggest that a relation may exist between the stripped morphology and the inclination of the galaxy with respect to the ICM wind, such that broader tails may be indicative of stripping at angles close to face-on to the wind. With a sufficiently large sample, it may be useful to further explore the possibility of such a relation.

An important result of this study is that we confirm that hydrodynamical interactions alone can produce curved tails due to the residual rotation of the stripped material. Since curved tails and stripped arcs can be signs of tidal interactions, care should be taken to confirm the origin of stripping when classifying samples of interacting galaxies based only on their morphology.

Chapter 5

Conclusions

5.1 Summary

The contents of this thesis have presented a series of studies into the process known as ram-pressure stripping as a mechanism of galaxy transformation in group and cluster environments, in the context of the current understanding of galaxy evolution in The Universe.

In Chapter 2, a case-study of a particular Jellyfish Galaxy JO201 from the GASP survey was presented. The galaxy is moving face-on at extreme speeds mostly along the line of sight through the Galaxy cluster Abell 85.

The MUSE observations revealed Hα emission associated with ionised gas in a dense arc along the leading edge of the galaxy and also extending out of the galaxy disk in the trailing direction. The presence of extraplanar ionised gas coupled with the lack of disturbance in the stellar disk confirmed this galaxy to be encountering ram-pressure stripping in its interaction with the cluster and rule out any gravitational effects which would disturb the stellar component.

The line-of-sight nature of the stripping was found to complicate the line profiles of the emission from the stripped material in the form of asymmetries in the velocity distribution. Clumps of gas located just outside the galaxy were found to have tails along the line of sight where gas has been pushed to higher redshifts relative to the galaxy, indicating that the gas around the trailing edge of the galaxy is in the process of being

removed by the ram-pressure interaction.

The kinematic analysis revealed that the gaseous component is progressively offset to higher redshifts with respect to the undisturbed, smoothly rotating stellar component. This is suggestive of ram-pressure stripping being most effective on the outermost regions of the galaxy, further from the influence of the galaxy potential well.

The large velocity dispersions measured in the diffuse stripped material coupled with the low velocity dispersions in the compact knots, suggesting that the gas is shock-heated as it is stripped from the galaxy, before cool clumps condense to form stars in the tails.

The results of the work described in the first chapter give an insight into the action of ram-pressure on a large galaxy in a massive cluster. The process of RPS appears to be most effectively removing gas from the outermost regions of the galaxy and is able to compress the gas along the leading edge of the galaxy disk, provoking star formation, whilst removing gas from the disk to form a diffuse tail with a high velocity dispersion behind the galaxy. Once removed, this gas can then cool and condense to form collapsed knots trailing behind the galaxy which are hot-spots for star formation.

In Chapter 3, the further physical properties of the galaxy JO201, the subject of Chapter 2, are investigated and presented. Classification of the ionisation sources across the disk and tails was carried out using the emission line ratios of the ionised gas. The material in the disk and the collapsed knots in the tail was found to dominated by photoionisation-driven emission, indicating high star formation. The central region of the galaxy disk was found to be dominated by AGN-driven ionisation. The metallicity of the gas was also studied, revealing a decreasing gradient with radial distance from the galaxy. This reinforces the result of the first chapter that that RPS acts in an outside-inward direction. In the stellar component, a similar radial gradient was observed, with the oldest knots residing closest to the disk and the age progressively decreasing with distance from the galaxy.

Simulations and modelling found that the galaxy is likely to have been experiencing some degree of RPS for ~ 1 Gyr, and that the tails are likely to extend ~ 94 kpc in the line of sight.

The results of Chapter 3 build a picture of the history of the RPS process transforming JO201. The ICM colliding with the galaxy acts to shock and compress the gas in the disk, invoking star formation. On the trailing side of the galaxy, the ICM wind strips the material from the disk, starting with the outermost, least

bound gas and progressively removing gas from deeper in the galaxy's potential as the process continues. The stripped gas then moves away from the galaxy, leaving a trail of collapsed knots behind it as it progresses, which become centres of intense star formation activity. The stars are no longer affected by subsequent pressure from the ICM wind, and remain in situ where they form. Eventually, these may be accreted back onto the galaxy, or if they are sufficiently removed, may disperse and contribute to the intracluster light. The AGN in the central region of JO201 is likely to have been triggered by the RPS compressing gas and provoking infall onto the central supermassive black hole (Poggianti et al., 2017a). The triggered AGN appears to be suppressing star formation in the central region corresponding to the fall-off in Hα emission, which was confirmed by a similar cavity in the UV emission by George et al. (2019). This acts to further supplement the quenching process of ram-pressure stripping by boosting the quantity of gas removed.

Chapter 4, presents an analysis of the morphological effects of ram-pressure stripping on galaxies, focusing on a particular subset of jellyfish galaxies from the GASP survey whose stripped material appears to trace the pattern of the spiral arms.

Out of the 13 galaxies which were inclined face-on to the observer with visible spiral arms, 12 exhibit the unwinding spiral arm phenomenon and are distributed across many regions of phase-space, suggesting that the effect may be common in stripped galaxies.

In the observed galaxies, stellar population analysis found that the unwinding component contained no discernible stellar component older than 20Myr, confirming that the extraplanar spiral arms were produced only by hydrodynamical effects and any stars were formed in-situ.

Simulated observations of galaxies undergoing ram-pressure stripping orientated face-on, edge-on and at 45° to the direction of the ICM wind were compared to investigate the different resulting patterns in the stripped material. It was found that galaxies moving edge-on to the wind experience a "pile-up" of material due to the ram-pressure differential between the edges rotating with and against the wind direction. The slowing of the gas as it rotates causes the pitch angle of the spiral arm pattern to increase. For galaxies traveling face-on to the wind the stripped gas, removed from the potential of the galaxy disk, can fall to higher orbits, slowing and increasing the pitch angle. The simulated galaxy experiencing RPS at 45° to the disk orientation was found to exhibit a combination of these two effects. The simulated RPS interactions result in unwound spiral arms in their stripped material which closely resemble many galaxies in the observed sample.

The resulting objects in the simulations appear to be compact, fast rotating objects, with steep rotation curves, once the lower-velocity material has been fully removed from the outer edges.

The results of Chapter 4 indicate an interesting effect of RPS. The large proportion of galaxies exhibiting the effect and their wide distribution across phase space suggest that it is fairly common, and the lack of previous observation may be due to unfavourable orientation or less discernible spiral patterns in observed galaxies. An interesting result of this study is that such "unwound" tails, which would previously have been a flag for tidal effects only, can also be a result of hydrodynamical effects, and morphological selection of samples should be carried out with care to account for this.

5.2 Discussion

Together the studies outlined and presented in these chapters build up a timeline of the process of ram-pressure stripping by the intracluster medium. This includes building an understanding of the overall effect of RPS on a galaxy undergoing infall, in addition to the small-scale effects which occur as part of the stripping process, within the galaxy and its tails. The results outlined in this thesis, combined with the studies conducted to date, show that ram-pressure can be an extremely effective mechanism by which galaxies, particularly those on first infall on radial orbits, can evolve in cluster environments. The interaction between the ICM and the galaxy can compress gas along the leading edge, increasing the star formation rate and in extreme cases funnel gas into the central supermassive black hole. In the case where infalling gas triggers AGN activity, the resulting energy release can cause outflows, removing material from the galaxy, and suppressing star formation in the central region, quenching the galaxy from the inside out. In the outer regions of the galaxy, where the gas stripping is most effective, ram-pressure proceeds to strip the gas from the outside inward. In some cases, denser structures in the gas component such as the outer regions of the spiral arms may retain their structure during stripping and manifest as denser "tentacles" in the tail, which may seed the in-situ formation of clumps. The stripped material, characterised by high velocity dispersion and composite emission, leaves a diffuse tail behind the galaxy, from which clumps of gas may cool and collapse to undergo star formation. Once formed, the stars are not susceptible to further stripping, and these knots will remain where they form. Eventually, the stars formed in the tail may fall back onto the galaxy or escape to contribute

to the intracluster light.

With the studies on galaxies undergoing ram-pressure to date, we have built a much better understanding of the specifics of ram-pressure stripping and its effect on individual galaxies, and we have begun to gain an insight into the wider role of ram-pressure stripping in galaxy evolution. In the future, it would be extremely useful to explore the role of the AGN in stripping processes with higher resolution imaging of the central regions of these objects, in order to better understand the conditions required for the AGN to "boost" stripping in the ways we have seen. Furthermore, it would be of great benefit to build larger catalogs of such interacting galaxies and develop alternative methods of selection which avoid the selection biases which come from visual inspection. This is important not only in order to build the known sample of jellyfish galaxies at low redshift, but also to expand the selection to include those at higher redshifts and begin to derive the cosmological impact of ram-pressure on the evolution of galaxies in the universe. As we approach the era of large surveys and big data astrophysics, developing automated techniques to select and explore samples from the immense quantities of data that will soon become available will be of paramount importance. Moreover, the vast samples of galaxies that could be obtained in this way will allow us to understand to a much greater degree the relations, trends and associations between different parameters. Ultimately, we should be able to shed light on a much wider swathe of the parameter space of interacting galaxies and the processes which shape them through cosmic time.

Bibliography

Abadi M. G., Moore B., Bower R. G., 1999, MNRAS, 308, 947

Anderson M. E., Bregman J. N., 2011, ApJ, 737, 22

Asplund M., Grevesse N., Sauval A. J., Scott P., 2009, ARA&A, 47, 481

Bacon R., et al., 2010, in Ground-based and Airborne Instrumentation for Astronomy III. p. 773508, doi:10.1117/12.856027

Bahcall J. N., Spitzer Lyman J., 1969, ApJ, 156, L63

Baldry I. K., Balogh M. L., Bower R. G., Glazebrook K., Nichol R. C., Bamford S. P., Budavari T., 2006, MNRAS, 373, 469

Baldwin J. A., Phillips M. M., Terlevich R., 1981, PASP, 93, 5

Balogh M. L., Navarro J. F., Morris S. L., 2000, ApJ, 540, 113

Barton E. J., Geller M. J., Kenyon S. J., 2000, ApJ, 530, 660

Bekki K., Couch W. J., 2003, ApJ, 596, L13

Bellhouse C., et al., 2017, ApJ, 844, 49

Bellhouse C., et al., 2019, MNRAS, 485, 1157

Benson A. J., Bower R. G., Frenk C. S., White S. D. M., 2000, MNRAS, 314, 557

Bertelli G., Bressan A., Chiosi C., Fagotto F., Nasi E., 1994, A&AS, 106, 275

Binney J., Tremaine S., 2008, Galactic Dynamics: Second Edition. Princeton University Press

Binney J., Nipoti C., Fraternali F., 2009, MNRAS, 397, 1804

Boselli A., Gavazzi G., 2006, PASP, 118, 517

Boselli A., Gavazzi G., Lequeux J., Buat V., Casoli F., Dickey J., Donas J., 1997, A&A, 327, 522

Boselli A., Cortese L., Boquien M., Boissier S., Catinella B., Lagos C., Saintonge A., 2014, A&A, 564, A66

Boselli A., et al., 2016, A&A, 587, A68

Boselli A., et al., 2018a, preprint, (arXiv:1802.02829)

Boselli A., et al., 2018b, preprint, (arXiv:1803.04177)

Boselli A., et al., 2019, A&A, 623, A52

Bower R. G., McCarthy I. G., Benson A. J., 2008, MNRAS, 390, 1399

Bravo-Alfaro H., van Gorkom J. H., Caretta C., 2008, in Baryshev Y. V., Taganov I. N., Teerikorpi P., eds, Vol. 1, too. pp 102–105

Bravo-Alfaro H., Caretta C. A., Lobo C., Durret F., Scott T., 2009, A&A, 495, 379

Byrd G., Valtonen M., 1990, ApJ, 350, 89

Calzetti D., 2013, Star Formation Rate Indicators. p. 419

Cappellari M., Copin Y., 2003, MNRAS, 342, 345

Cappellari M., Emsellem E., 2004, PASP, 116, 138

Cardelli J. A., Clayton G. C., Mathis J. S., 1989, ApJ, 345, 245

Cava A., et al., 2009, A&A, 495, 707

Cavaliere A., Fusco-Femiano R., 1976, A&A, 49, 137

Cayatte V., van Gorkom J. H., Balkowski C., Kotanyi C., 1990, AJ, 100, 604

Chabrier G., 2003, PASP, 115, 763

Chen Y., Reiprich T. H., Böhringer H., Ikebe Y., Zhang Y.-Y., 2007, A&A, 466, 805

Choi H., Yi S. K., 2017, ApJ, 837, 68

Chung A., van Gorkom J. H., Kenney J. D. P., Vollmer B., 2007, ApJ, 659, L115

Chung A., van Gorkom J. H., Kenney J. D. P., Crowl H., Vollmer B., 2009, AJ, 138, 1741

Cid Fernandes R., Mateus A., Sodré L., Stasińska G., Gomes J. M., 2005, MNRAS, 358, 363

Consolandi G., Gavazzi G., Fossati M., Fumagalli M., Boselli A., Yagi M., Yoshida M., 2017, A&A, 606, A83

Cortese L., et al., 2007, MNRAS, 376, 157

Cortese L., et al., 2010, A&A, 518, L49

Cortese L., Catinella B., Boissier S., Boselli A., Heinis S., 2011, MNRAS, 415, 1797

Cowie L. L., McKee C. F., 1977, ApJ, 211, 135

Cowie L. L., Songaila A., 1977, Nature, 266, 501

Crain R. A., McCarthy I. G., Frenk C. S., Theuns T., Schaye J., 2010, MNRAS, 407, 1403

Croton D. J., et al., 2006, MNRAS, 365, 11

Dai X., Anderson M. E., Bregman J. N., Miller J. M., 2012, ApJ, 755, 107

Dekel A., et al., 2009, Nature, 457, 451

Diehl S., Statler T. S., 2006, MNRAS, 368, 497

Dopita M. A., Sutherland R. S., Nicholls D. C., Kewley L. J., Vogt F. P. A., 2013, ApJS, 208, 10

Dressler A., 1980, ApJ, 236, 351

Dressler A., Shectman S. A., 1988, AJ, 95, 985

Durret F., Lima Neto G. B., Forman W., 2005, A&A, 432, 809

Ebeling H., Stephenson L. N., Edge A. C., 2014, ApJ, 781, L40

Ellison S. L., Simard L., Cowan N. B., Baldry I. K., Patton D. R., McConnachie A. W., 2009, MNRAS, 396, 1257

Evrard A. E., 1991, MNRAS, 248, 8P

Faltenbacher A., Diemand J., 2006, MNRAS, 369, 1698

Fasano G., et al., 2015, Monthly Notices of the Royal Astronomical Society, 449, 3927

Fossati M., Gavazzi G., Boselli A., Fumagalli M., 2012, A&A, 544, A128

Fossati M., Fumagalli M., Boselli A., Gavazzi G., Sun M., Wilman D. J., 2016, MNRAS, 455, 2028

Fossati M., et al., 2018, preprint, (arXiv:1801.09685)

Fritz J., et al., 2007, A&A, 470, 137

Fritz J., et al., 2017, ApJ, 848, 132

Fujita Y., 1998, ApJ, 509, 587

Fujita Y., Nagashima M., 1999, ApJ, 516, 619

Fukugita M., Peebles P. J. E., 2004, ApJ, 616, 643

Fukugita M., Peebles P. J. E., 2006, ApJ, 639, 590

Fumagalli M., Gavazzi G., Scaramella R., Franzetti P., 2011, A&A, 528, A46

Fumagalli M., Fossati M., Hau G. K. T., Gavazzi G., Bower R., Sun M., Boselli A., 2014, MNRAS, 445, 4335

Gavazzi G., Boselli A., Pedotti P., Gallazzi A., Carrasco L., 2002a, A&A, 396, 449

Gavazzi G., Bonfanti C., Sanvito G., Boselli A., Scodeggio M., 2002b, ApJ, 576, 135

George K., et al., 2018, MNRAS, 479, 4126

George K., et al., 2019, MNRAS, 487, 3102

Girardi L., Bressan A., Chiosi C., Bertelli G., Nasi E., 1996, A&AS, 117, 113

Gullieuszik M., et al., 2017, ApJ, 846, 27

Gunn J. E., Gott III J. R., 1972, ApJ, 176, 1

Gupta A., Yuan T., Martizzi D., Tran K.-V. H., Kewley L. J., 2017, ApJ, 842, 75

Haines C. P., et al., 2015, ApJ, 806, 101

Haynes M. P., Giovanelli R., 1984, AJ, 89, 758

Hernquist L., Barnes J. E., 1991, Nature, 354, 210

Hess K. M., Wilcots E. M., 2013, AJ, 146, 124

Hester J. A., et al., 2010, ApJ, 716, L14

Ho I.-T., et al., 2014, MNRAS, 444, 3894

Ho I. T., et al., 2017, ApJ, 846, 39

Hoag A. A., 1950, AJ, 55, 170

Ichinohe Y., Werner N., Simionescu A., Allen S. W., Canning R. E. A., Ehlert S., Mernier F., Takahashi T., 2015, MNRAS, 448, 2971

Jaffé Y. L., Poggianti B. M., Verheijen M. A. W., Deshev B. Z., van Gorkom J. H., 2012, ApJ, 756, L28

Jaffé Y. L., Smith R., Candlish G. N., Poggianti B. M., Sheen Y.-K., Verheijen M. A. W., 2015, MNRAS, 448, 1715

Jaffé Y. L., et al., 2016, MNRAS, 461, 1202

Jaffé Y. L., et al., 2018, MNRAS, 476, 4753

Jones C., Forman W., 1999, ApJ, 511, 65

Kapferer W., Sluka C., Schindler S., Ferrari C., Ziegler B., 2009, A&A, 499, 87

Katz N., Keres D., Dave R., Weinberg D. H., 2003, in Rosenberg J. L., Putman M. E., eds, Astrophysics and Space Science Library Vol. 281, The IGM/Galaxy Connection. The Distribution of Baryons at z=0. p. 185 (arXiv:astro-ph/0209279), doi:10.1007/978-94-010-0115-1˙34

Kauffmann G., et al., 2003, MNRAS, 346, 1055

Kenney J. D. P., Koopmann R. A., 1999, AJ, 117, 181

Kenney J. D. P., Young J. S., 1989, ApJ, 344, 171

Kenney J. D. P., van Gorkom J. H., Vollmer B., 2004, AJ, 127, 3361

Kenney J. D. P., Geha M., Jáchym P., Crowl H. H., Dague W., Chung A., van Gorkom J., Vollmer B., 2014, ApJ, 780, 119

Kennicutt Robert C. J., 1998, ARA&A, 36, 189

Kennicutt Jr. R. C., Roettiger K. A., Keel W. C., van der Hulst J. M., Hummel E., 1987, AJ, 93, 1011

Kereš D., Katz N., Weinberg D. H., Davé R., 2005, MNRAS, 363, 2

Kewley L. J., Dopita M. A., Sutherland R. S., Heisler C. A., Trevena J., 2001a, ApJ, 556, 121

Kewley L. J., Dopita M. A., Sutherland R. S., Heisler C. A., Trevena J., 2001b, ApJ, 556, 121

Kronberger T., Kapferer W., Unterguggenberger S., Schindler S., Ziegler B. L., 2008, A&A, 483, 783

Lacey C., Cole S., 1993, MNRAS, 262, 627

Larson R. B., Tinsley B. M., Caldwell C. N., 1980, ApJ, 237, 692

Lavery R. J., Henry J. P., 1988, ApJ, 330, 596

Lin L., et al., 2008, ApJ, 681, 232

Maloney P., Black J. H., 1988, ApJ, 325, 389

McPartland C., Ebeling H., Roediger E., Blumenthal K., 2016, MNRAS, 455, 2994

Merluzzi P., et al., 2013, MNRAS, 429, 1747

Merritt D., 1983, ApJ, 264, 24

Mihos J. C., Hernquist L., 1994, ApJ, 425, L13

Mihos J. C., Richstone D. O., Bothun G. D., 1992, ApJ, 400, 153

Mihos J. C., Bothun G. D., Richstone D. O., 1993, ApJ, 418, 82

Mo H., van den Bosch F. C., White S., 2010, Galaxy Formation and Evolution

Moore B., Katz N., Lake G., Dressler A., Oemler A., 1996, Nature, 379, 613

Moore B., Lake G., Katz N., 1998, ApJ, 495, 139

Moretti A., et al., 2017, A&A, 599, A81

Moretti A., et al., 2018a, MNRAS, 475, 4055

Moretti A., et al., 2018b, MNRAS, 480, 2508

Navarro J. F., Frenk C. S., White S. D. M., 1996, ApJ, 462, 563

Nipoti C., 2010, MNRAS, 406, 247

Nulsen P. E. J., 1982, MNRAS, 198, 1007

Osterbrock D. E., Ferland G. J., 2006, Astrophysics of gaseous nebulae and active galactic nuclei

Owers M. S., Couch W. J., Nulsen P. E. J., Randall S. W., 2012, ApJ, 750, L23

Peng Y.-j., et al., 2010, ApJ, 721, 193

Peng Y., Maiolino R., Cochrane R., 2015, Nature, 521, 192

Perret V., Renaud F., Epinat B., Amram P., Bournaud F., Contini T., Teyssier R., Lambert J. C., 2014, A&A, 562, A1

Poggianti B. M., et al., 2016, AJ, 151, 78

Poggianti B. M., et al., 2017a, Nature, 548, 304

Poggianti B. M., et al., 2017b, ApJ, 844, 48

Press W. H., Schechter P., 1974, ApJ, 187, 425

Proxauf B., Öttl S., Kimeswenger S., 2014, A&A, 561, A10

Quilis V., Moore B., Bower R., 2000, Science, 288, 1617

Quinn P. J., Goodman J., 1986, ApJ, 309, 472

Quinn P. J., Hernquist L., Fullagar D. P., 1993, ApJ, 403, 74

Ramatsoku M., et al., 2019, MNRAS, 487, 4580

Rasmussen J., Ponman T. J., Mulchaey J. S., 2006, MNRAS, 370, 453

Rasmussen J., Ponman T. J., Verdes-Montenegro L., Yun M. S., Borthakur S., 2008, MNRAS, 388, 1245

Rasmussen J., Sommer-Larsen J., Pedersen K., Toft S., Benson A., Bower R. G., Grove L. F., 2009, ApJ, 697, 79

Rawle T. D., et al., 2014, MNRAS, 442, 196

Rhee J., Smith R., Choi H., Yi S. K., Jaffé Y., Candlish G., Sánchez-Jánssen R., 2017, ApJ, 843, 128

Roediger E., Brüggen M., Owers M. S., Ebeling H., Sun M., 2014, MNRAS, 443, L114

Salpeter E. E., 1955, ApJ, 121, 161

Sánchez-Menguiano L., et al., 2017, A&A, 603, A113

Schlafly E. F., Finkbeiner D. P., 2011, ApJ, 737, 103

Schweizer F., 1996, AJ, 111, 109

Schweizer F., Ford W. Kent J., Jedrzejewski R., Giovanelli R., 1987, ApJ, 320, 454

Sharp R. G., Bland-Hawthorn J., 2010, ApJ, 711, 818

Smith R. J., et al., 2010, MNRAS, 408, 1417

Smith R., Flynn C., Candlish G. N., Fellhauer M., Gibson B. K., 2015, MNRAS, 448, 2934

Spitzer Jr. L., Baade W., 1951, ApJ, 113, 413

Springel V., 2000, MNRAS, 312, 859

Springel V., et al., 2005, Nature, 435, 629

Sun M., Donahue M., Roediger E., Nulsen P. E. J., Voit G. M., Sarazin C., Forman W., Jones C., 2010, ApJ, 708, 946

Takeda H., Nulsen P. E. J., Fabian A. C., 1984, MNRAS, 208, 261

Teyssier R., 2002, A&A, 385, 337

Tinsley B. M., Larson R. B., 1979, MNRAS, 186, 503

Toft S., Rasmussen J., Sommer-Larsen J., Pedersen K., 2002, MNRAS, 335, 799

Tonnesen S., Bryan G. L., 2009, ApJ, 694, 789

Tonnesen S., Bryan G. L., 2010, ApJ, 709, 1203

Tonnesen S., Bryan G. L., 2012, MNRAS, 422, 1609

Toomre A., 1977, in Tinsley B. M., Larson D. Campbell R. B. G., eds, Evolution of Galaxies and Stellar Populations. Yale University Observatory, p. 401

Toomre A., Toomre J., 1972, ApJ, 178, 623

Tran K.-V. H., van Dokkum P., Franx M., Illingworth G. D., Kelson D. D., Schreiber N. M. F., 2005, ApJ, 627, L25

Tremonti C. A., et al., 2004, ApJ, 613, 898

Valluri M., 1993a, ApJ, 408, 57

Valluri M., 1993b, ApJ, 408, 57

Valluri M., Jog C. J., 1990, ApJ, 357, 367

Vazdekis A., Sánchez-Blázquez P., Falcón-Barroso J., Cenarro A. J., Beasley M. A., Cardiel N., Gorgas J., Peletier R. F., 2010, MNRAS, 404, 1639

Veilleux S., Cecil G., Bland-Hawthorn J., 2005, ARA&A, 43, 769

Venkatapathy Y., et al., 2017, AJ, 154, 227

Vikhlinin A., Forman W., Jones C., 1997, ApJ, 474, L7

Vogt F. P. A., Seitenzahl I. R., Dopita M. A., Ruiter A. J., 2016a, preprint, (arXiv:1611.03862)

Vogt F. P. A., Owen C. I., Verdes-Montenegro L., Borthakur S., 2016b, ApJ, 818, 115

Vogt F. P. A., Pérez E., Dopita M. A., Verdes-Montenegro L., Borthakur S., 2017, Astronomy and Astrophysics, 601, A61

Vollmer B., Cayatte V., Balkowski C., Duschl W. J., 2001, ApJ, 561, 708

Vollmer B., Wong O. I., Braine J., Chung A., Kenney J. D. P., 2012, A&A, 543, A33

Vulcani B., Poggianti B. M., Fritz J., Fasano G., Moretti A., Calvi R., Paccagnella A., 2015, ApJ, 798, 52

Vulcani B., et al., 2018, ApJ, 866, L25

White S. D. M., Frenk C. S., 1991, ApJ, 379, 52

White S. D. M., Rees M. J., 1978, MNRAS, 183, 341

Woods D. F., Geller M. J., Barton E. J., 2006, AJ, 132, 197

Yagi M., et al., 2010, AJ, 140, 1814

Yoon Y., Im M., Kim J.-W., 2017, ApJ, 834, 73

Yoshida M., et al., 2008, ApJ, 688, 918

Zavala J., Balogh M. L., Afshordi N., Ro S., 2012, MNRAS, 426, 3464

van Dokkum P. G., 2005, AJ, 130, 2647

van de Voort F., Schaye J., 2012, MNRAS, 423, 2991

van den Bosch F. C., 2002, MNRAS, 332, 456